Multiphase Flow & Mixing in Microreactors

Submitted in partial fulfillment of the requirements for the degree of

Doctor of Philosophy

by

Ajay K. Gorasia

Roll No. 05402701

Supervisor: Prof. Sanjay Mahajani

Department of Chemical Engineering
Indian Institute of Technology, Bombay

2009

Thesis entitled: MULTIPHASE FLOW & MIXING IN MICROREACTORS

by   AJAY K. GORASIA

is approved for the degree of DOCTOR OF PHILOSOPHY

Examiners

_____

_____

_____

_____

Supervisors

_____

_____

Chairman

_____

Date: _____

Place: _____

INDIAN INSTITUTE OF TECHNOLOGY, BOMBAY, INDIA

CERTIFICATE OF COURSE WORK

This is to certify that Mr. Ajay K. Gorasia was admitted to the candidacy of the Ph.D. Degree on 22nd day of July 2005 after successfully completing the entire courses requirement for the Ph.D. Degree program. The details of the course work done are given below

Sr. No.	Course No.	Course Name	Credits
1	CL 601	Advanced transport phenomena	6.0
2	CL 701	Computational methods in chemical engineering	8.0
3	CL 702	Lecture series	2.0
4	CLS 801	Seminar	4.0
5	HS 699	Communication and presentation skills	4.0

I.I.T. Bombay   Dy. Registrar(Academic)

Dated:

To,
My Parents,
Teachers

Table of Contents

Abstract

Efficient and effective design of process equipment requires delivery of right amount of materials and energy at the right places and at the right times. The challenge is to ensure that the reactor hardware and operating protocol satisfy various process demands without compromising safety, the environment and economics. Microreactors because of their miniaturized and compact structure have better control on delivery of material and energy at right location and at right time. Shorter path lengths for thermal and molecular diffusion enable them to offer significantly higher transport rates, thereby enabling them to provide an ideal environment for rapid exothermic/endothermic reactions. The aim of the present work is to develop experimental and computational modeling tools, which will help in determining key hydrodynamic parameters necessary to quantify flow and mixing in microreactors.

Hydrodynamic parameters were measured using experimental measurement techniques like digital imaging and conductivity probes. Multi level CFD models are developed to simulate slug flows in capillaries. Different hydrodynamic parameters measured experimentally or determined using CFD simulations were incorporated in chemical reaction engineering model to predict performance of microreactors. Besides investigating flow mixing and reactions in a single unit of microreactor, attempts have also been made to extrapolate flow and mixing studies to newer designs such as 'mesh-microreactor' and contact angle mediated compact microreactor cum separator.

Keywords: Microreactors, hydrodynamics, CFD, 'mesh-microreactor', 'Y' separator

List of Tables

List of Figures

Nomenclature

a	interfacial area per unit volume (m^2/m^3)
A	cross sectional area of the channel (m^2)
C_0	distribution parameter (dimensionless)
C	concentration ($kmol/m^3$)
D	dispersion coefficient (m^2/s)
d_B	Bubble Diameter (m)
d_c	diameter of the channel (m)
D_{ax}	axial dispersion coefficient (m^2/s)
D_{eff}	diffusion coefficient (m^2/s)
F	Frequency (s^{-1})
g	Acceleration due to gravity (m/s^2)
H	height of mesh microreactor (mm)
k_L	exchange coefficient ($N \cdot v_L / H$), 1/s
k	mass transfer coefficient (m/s)
k_0	frequency factor (m3/mols)
K	absorption constant, (m^3/mol)
L	Time averaged length (m)
L_{int}	interfacial length (m)
L_{Bubble}	length of the bubble (m)
L_{slug}	length of the slug (m)
L_{UC}	length of unit cell (m)
M	molecular weight
N	number of transfer units (-)
P	pressure (N/m^2)
Q	flow rate (m3/ s)
R	Radius of the microchannel (m)
RTD	residence time distribution
r	radial position (m)
r_{Curv}	radius of curvature (m)
r	reaction rate (kmol/(m3 of liq vol) s)
r_V	reaction rate per unit washcoat volume, (kmol/(m^3 of catalyst volume) s)
t	time (s)
U	superficial velocity (m/s)

U_B bubble velocity (m/s)

U_{GS} superficial gas velocity (m/s)

U_{LS} superficial liquid velocity (m/s)

U_{TP} Two phase velocity = $U_{LS} + U_{GS}$ (m/s)

U_{wall} wall velocity (m/s)

V_{Bubble} volume of bubble (m^3)

V_{UC} volume of unit cell (m^3)

V_D Relative drift velocity (m/s)

t time (s)

T   temperature (°K)

W Dimensionless relative bubble velocity

x normalized distance from the location of entrance of the tracer pulse (-)

x mass fraction (dimensionless)

z axial position (m)

Greek symbols

ε Void fraction of the phase (dimensionless)

δ Film thickness (m)

β Ratio of bubble length to length of unit cell (dimensionless)

μ Viscosity of the respective phase (Pa-s)

ρ Density of the respective phase (kg/m^3)

σ Surface tension (N/m)

τ Time (s)

λ Laplace constant

α volumetric gas quality

ϕ mass transfer enhancement factor

ψ Bubble shape factor

ν Stochiometric coefficient

ε_G gas holdup (dimensionless)

$\delta(t)$ Dirac's δ function (-)

$\bar{t}$ Characteristic time (s)

ρ_{mix} mixture density (kg/m^3)

Subscripts

L & G	liquid and gas phases
l & g	liquid and gas phase
GS	superficial gas velocity
LS	superficial liquid velocity
TP	Overall superficial velocity (Gas superficial velocity + Liquid superficial velocity)
B	Bubble
lf	Liquid film
S	Liquid slug
i	Bubble index
G	gas phase
L	liquid phase
S	solid phase
d	dynamic zone in the individual mesh elements
St	static zone in the individual mesh elements
f	fluid region
i	component index
G-f	gas phase in the fluid region
L-f	liquid phase in the fluid region
L-wc	liquid phase in the wash-coat region
s	surface of the solid catalyst
wc	wash-coat region
GL	gas to liquid
LS	liquid to solid

Dimensionless Numbers and Parameters

Bo	Bond Number	$Bo = \dfrac{\rho_L g D^2}{\sigma}$
Ca	Capillary Number	$Ca = \dfrac{\mu U_B}{\sigma}$
Fr	Froude Number	$Fr = \dfrac{U_B^{\,2}}{gD}$
Re	Reynolds Number	$Re = \dfrac{D U_B \rho_L}{\mu_L}$
Su	Suratman Number	$Su = \dfrac{\sigma D \rho_L}{\mu_L^{\,2}}$

Eo	Eotvos number	$Eo = \dfrac{(\rho_L - \rho_G)gD^2}{\sigma}$
We	Weber number	$We = \dfrac{\rho_L U_B{}^2 D}{\sigma}$
Nf	Fluid property number	$Nf = \dfrac{g\mu_L{}^4}{\sigma^3 \rho_L}$

Chapter 1

Introduction

1.1 Background and motivation

Major advances for chemical industries will, no doubt, continue to emerge from catalysis, chemistry, and biological sciences. However, maximizing the industrial benefit from these advances requires comparable advances in design of required process equipment, reactors and products. Efficient and effective design of process equipment requires delivery of right amount of materials and energy at the right places and at the right times. The challenge is to ensure that the reactor hardware and operating protocol satisfy various process demands without compromising safety, the environment and economics.

Microreactors because of their miniaturized and compact structure have better control on delivery of material and energy at right location and at right time. Shorter path lengths for thermal and molecular diffusion enable them to offer significantly higher transport rates, thereby enabling them to provide an ideal environment for rapid exothermic/endothermic reactions. Additionally, these reactors can simply be bundled together for large scale production. This reduces the problem of scale-up arising in conventional reactors. Hence these reactors are seen as the future of chemical process engineering for specialty and fine chemicals. They are also looked upon as one of the potential candidates for process intensification for several industrially important processes.

Though microreactor technology is relatively new area for engineers, several experimental and modeling studies have been carried out to identify the hydrodynamic flow regimes and their transitions for gas-liquid flows through various small-scale geometries (e.g. Paglianti et al., 1996; Mishima and Hibiki, 1996; Triplett et al., 1999; Kreutzer, 2003, Simmons et al., 2003). Dispersion and mass transfer studies for gas-liquid flows have also been published (e.g. Thulasidas et al., 1995; Bercic and Pintar, 2003; Elperin and Fominykh, 1998). Experimental techniques like particle image velocimetry (PIV) (e.g. Thulasidas et al., 1997), µPIV (e.g. Devasenathipathy et al., 2003) and optical sensors (e.g. Kraus et al., 2004) have shown strong potential in characterization of flow field in the microchannels. A few studies on characterization of multiphase microreactors using CFD modeling for hydrodynamics and mass transfer have also published (e.g. Taha and Cui, 2004, 2006; van Baten and Krishna 2004). As can be seen these studies are still preliminary and discrete. Further investigation is required to understand and thereby improve the performance of these reactors.

Chemical reactions carried out using microreactors are mainly exploratory. Most researchers tried different chemistries using microreactors and reported increased performance in terms of conversion and selectivity as compared with conventional reactors. Couple of comprehensive reviews on reactions carried using these reactors is reported by Pennmann et al., (2004), Ehrfeld et al., (2000) and Hessel et al., (2003). However, most of these studies don't give any explanation for the observed performance enhancement. Hence a proper reaction engineering analysis to explain this loop hole is a must.

Advent of micromachining technology has enabled fabrication of very complex contacting patterns. However, the cost of such fabrications is huge. Since with microreactors, scale-up is achieved by numbering up and not by increasing the physical dimensions of the reactors, the issue of distributing materials to large number of micro-reactors also becomes crucial. Hence one has to have a clear understanding on how small is adequate, and how can one achieve the desired performance at minimal cost. Efforts are also being made to integrate different process operations such as mixing, heating, reaction and separations into a compact micro-reactor configuration which can be optimized as per the requirements of the reactions under consideration (Kralj et al., 2007 and Kashid et al., 2007). Such systems also need to be explored in depth.

Considering these points, the present work was taken up to develop experimental and computational modeling tools, which will help in determining key hydrodynamic parameters necessary to quantify flow and mixing in microreactors. The study is supplemented with reaction engineering models to evaluate performance of microreactors. Besides investigating flow mixing and reactions in a single unit of microreactor, attempts have also been made to extrapolate flow and mixing studies to newer designs such as 'mesh-microreactor' and contact angle mediated compact microreactor cum separator.

1.2 Objectives

Based on issues discussed in previous section and critical review of published information, the research for this thesis was planned with following objectives:

- Develop measurement techniques to characterize key hydrodynamic parameters of gas-liquid flow through capillaries
- Develop computational fluid dynamics (CFD) based models capable of simulating flow and mass transfer of slug flows in capillaries
- Develop a generalized reaction engineering model to simulate performance of microreactors
- Explore and evaluate flow and mixing in newer designs of microreactors such as mesh reactor and liquid-liquid slug flow reactor cum separator

1.3 Methodology

The methodology used in this work is summarized in Figure 1.1. The proposed work is organized into experimental measurements, computational modeling and simulations. Various hydrodynamic parameters were measured using experimental measurement techniques like digital imaging and conductivity probes. Multi level CFD models are developed to simulate slug flows in capillaries. Different hydrodynamic parameters measured experimentally or determined using CFD simulations were incorporated in chemical reaction engineering model to predict performance of microreactors.
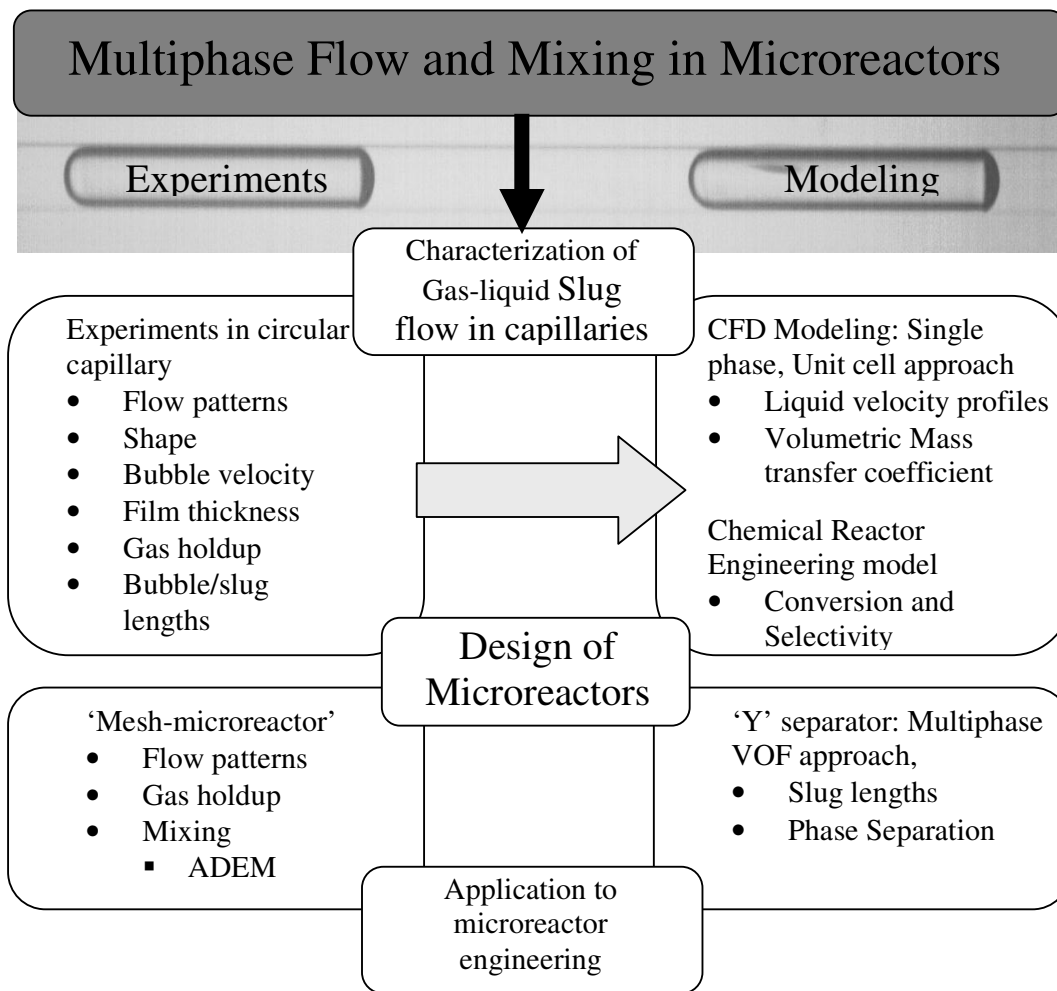
Figure 1.1: Overall methodology

1.4 Organization of thesis

The overall thesis is organized as follows. In PART ONE, the characterization of gas-liquid flows in a single unit of microreactor i.e. capillaries using experimental and modeling tools is presented (Chapters 2, 3 & 4). In PART TWO, applications to microreactor engineering are discussed (Chapters 5 & 6). Chapter wise discussion of this work is as given below.

Chapter 1 gives the brief introduction to the thesis, the motivation to undertake the present research, the specific objectives of the research work carried, methodology adopted to achieve the mentioned objectives and finally the organization of the thesis is discussed.

PART I: Gas-liquid slug flow in capillaries

Chapter 2 describes the experimental characterization of gas-liquid slug flow in capillaries using flow visualization studies. Experiments are carried out to study influence of gas and liquid flow rates on various hydrodynamic properties such as flow patterns, bubble shape, bubble/slug velocity, film thickness, gas holdup and bubble and liquid slug lengths. The measured experimental data are compared with different correlations and experimental data available in the literature and commented on their effective utilization.

In chapter 3, a computational fluid dynamics (CFD) model was developed to simulate slug flow in capillaries. The model is based on a unit cell approach. Bubble is considered as void and steady state single phase simulations are performed to predict liquid velocity profiles and mass transfer in slug flow. Simulated velocity profiles were compared with the experimental PIV data from Birmingham University.

Chapter 4 discusses development of chemical reactor engineering model based on mass and energy balances. The model is quite general and can account for any gas-liquid, liquid-liquid and gas-liquid-solid reactions in microchannels. Case-study of hydrogenation of 2,4,DNT was undertaken to demonstrate application of the developed model.

PART II: Applications to microreactor engineering

In Chapter 5 'mesh-microereactor' concept as multiphase microreactor is explored. The concept is based on creating micro-channel like structures by simply sandwiching a mesh within two flat plates. Flow and mixing studies were undertaken to quantify characteristics of mesh microreactor. A basic methodology to characterize these types of reactors was established which will form a basis for further studies.

Lastly Chapter 6 discusses development of multiphase CFD model based on VOF approach to study the contact angle based coupled reactor-separator type microreactor proposed by Agar and co-workers (Kashid, 2007). Variations of slug lengths with flow rates were determined and compared with the experimental data. The model will form a useful basis for further efforts to quantify separation efficiency.

Chapter 2

Experimental Characterization

2.1. Introduction

Gas-liquid flows through capillaries/small sized channels are widely used in variety of application ranging from micro-electro-mechanical systems, electronic cooling, nuclear power plant cooling, chemical process engineering, micro-reactor engineering, bio-engineering, aerospace engineering etc., Several studies are being conducted to experimentally characterize gas-liquid flows in capillaries. Previous experimental studies in micro channel are summarized in Table 2.1. Depending upon operating flow rates and channel dimensions different flow patterns such as bubble, slug, churn, annular and their transitions may occur. Among these, slug flow pattern (also called Taylor flow, bubble-train flow) spans over a wide range of liquid and gas velocities. It is characterized by the pseudo-periodic occurrence of long capsular gas bubbles followed by liquid slugs. The gas bubbles and the liquid slugs are separated from the wall by a thin liquid film. The most interesting feature of slug flow is its segmented nature. The separation of the liquid slugs by the gas bubbles reduces the axial dispersion. The recirculations from liquid slugs improves the heat and mass transfer from liquid to wall and interfacial mass transfer from gas to liquid (Bercic and Pintar 2003). Because of the combined advantage of reduced axial dispersion and enhanced radial mixing, slug flow regime attracts a variety of industrial applications.

Despite being one of the most studied flow regime in micro-channels, there is still no adequate description of the flow pattern and its characteristics (slug/bubble length/velocities, frequency hold-up etc.). This is mainly because the characteristics of slug flow are strong function of large number of system (capillary dimension, mixing unit, capillary MoC etc.) and operating parameters (flow rates, density viscosity, surface/interfacial tension etc). Secondly most of the research in this field was discrete. Some investigators only studied flow regimes and didn't look for shape lengths velocities etc., while others who accounted for those parameters didn't cover the whole range. Hence there is a need to unify all the studies in the past and correlate all the parameters to develop better understanding of slug flow in narrow channels.

Table 2.1: Recent studies on gas-liquid flows in microchannel

Reference	Gas-Liquid system used	Channel Geometry and orientation	Range of superficial velocities (m/s)	Studied parameters
Irandoust and Andersson (1989)	Air/water, Air/ethanol Air/glycerol	Circular(V) 1.0 , 2.0 mm	U_{GS} = 0.04- 0.66 U_{LS} = 0.04- 0.66	Film thickness
Kariyasaki et al. (1991)		Circular (VU, VD) 1, 2.4, 4.9 dia RectangularAspect ratio- 1 to 9	U_{GS}: 0.1-30 U_{LS}: 0.03 – 2.3	Flow pattern, void fraction, frictional pressure drop
Thulasidas et al. (1995)	Air/ silicone oil	Rectangular (H, VU, VD) 2mm DH		Relative bubble velocity, bubble diameter, dimensionless bubble velocity
Mishima and Hibiki (1996)	Air/water	Circular (VU) 1- 4 mm dia	U_{GS}=0.0896-33.5 U_{LS}=0.0116-1.67	Bubble velocity; Distribution parameter
Laborie et al (1999)	Air/water Air/water-Glycerol Air/water-Ethyl Alcohol	Circular (V) 1,2,3,4mm	U_{LS} = 0.08 - 0.9 U_{GS} = 0.1 – 1	Bubble velocity, length of bubble and slug, frequency
Kawahara et al. (2002)	Nitrogen / water	Circular 0.1mm	U_{GS} = 0:1–60 U_{LS} = 0.02–4	Flow pattern, void fraction, pressure drop
Chen et al (2002)	Nitrogen/ water	Circular (H) 1,1.5 mm	U_{GS}= 0.29 -10.29 U_{LS}= 0.399 -1.11	Flow regimes; Bubble velocity
Chung et al. (2004)	Nitrogen / water	Circular 0.53,0.25,0.1,0.05 mm	U_{LS}= 0.01-5.77 U_{GS} = 0.02 -73	Two phase flow characteristics, void fraction
Wren et al. (2005)	Air/water	Circular (H) 5mm dia	U_{LS}= 0.093 - 0.313 m/s U_{GS}= 1.14 - 4.56 m/s	Frequency
Liu et al (2005)	Air/water Air/oil	Square (V) hydraulic diameters from 0.9 mm to 3 mm	U_{LS}, U_{GS} : 0.008-1m/s	Flow patterns, Bubble velocity, Bubble and slug lengths
Qian and Lawal (2006)	Air/water	Circular (H) 0.25, 0.5. 0.75, 1, 2, 3mm	U_{GS}: 0.05-0.1 m/s U_{LS}: 0.02-0.2 m/s	Effect of inlet configuration, viscosity, surface tension, channel diameter and various dimensionless parameters on bubble and slug lengths
Ide et al. (2007)	Air/water	Circular, (H, VU, VD) 1,2.4,4.9 mm dia Rectangular Aspect ratio 1 to 9	U_{GS} = 0.5-8 m/s U_{LS} = 0.2-1 m/s	Influence of direction of flow
Warnier et al. (2008)	Nitrogen/ water	Rectangular(H) 0.1*0.05mm.	--	Gas holdup and liquid film thickness

H: Horizontal, V: Vertical, VD: Vertical Downward, VU: Vertical Upward

Most of the earlier work on gas-liquid flows in capillaries was focused on identifying flow regime maps and their transitions (see foe example Triplett et al., 1999, Chen et al, 2002, Kawahara et al., 2002, Serizawa and Kawara, 2002, and Akbar et al., 2003, Simmons et al. 2003). Since the key objective of the present work was to study slug flow and its characteristics only work which is relevant to the present study was reviewed and is summarized in Table 2.2

Table 2.2: Review of previous work on hydrodynamic characteristics of gas-liquid slug flow in capillaries

Reference	System & operating parameters	Correlation
Bubble Velocity		
Mishima and Hibiki (1996)	Air/water Circular, (VU), 1- 4 mm U_{GS}=0.0896-33.5m/s U_{LS}=0.0116-1.67 m/s	$U_B = C_0 U_{TP}$ $C_0 = 1.2 + 5.1 e^{-0.691 d}$ C_0 =1.45,1.31,1.33,1.21 for d =1.09, 2.10, 3.08, 3.90
Laborie et al (1999)	Air/water, Air/water-Glycerol, Air/water-Ethyl Alcohol Circular, (V), 1,2,3,4mm diameter ULS = 0.08 - 0.9 m/s UGS = 0.1 – 1 m/s	$U_B = C_0 U_{TP}$ $U_B = a (Eo)^b$ where a and b are dependent on the fluid property number Nf defined by wallis et al. (1969)
Liu et al (2005)	Air/water, Air/oil Circular, Square (V)d_H = 0.9-3mm U_{LS}, U_{GS} : 0.008-1m/s	$\dfrac{U_B}{U_{TP}} = \dfrac{1}{1 - 0.61 Ca_{UTP}^{0.33}}$
Ide et al. (2007))	Air/water, Circular, (H, VU,VD) 1,2.4,4.9mm Rectangular: Aspect ratio 1 to 9 U_{GS} = 0.5-8 m/s U_{LS} = 0.2-1 m/s	$U_B = C_k (U_{TP})^{1.05}$ C_k = 1.09 for D = 4.9 mm, C_k = 1.17 for D = 2.4mm and C_k = 1.21 for D = 1 mm.
Film thickness		
Fairbrother and stubbs (1935)	Air/water Circular (H) 5mm	$\delta = \dfrac{r}{2}\left(\dfrac{U_B \mu_L}{\sigma_L}\right)^{0.5} = \dfrac{r}{2} Ca^{0.5}$ $W = \dfrac{U_B - U_{TP}}{U_B} = 1.0 Ca^{0.5}$ $0.001 < Ca < 0.1$
Bretherton (1961)	Air/aniline, Air/benzene Circular (H, V) 1mm	$\dfrac{2\delta}{D} = 1.34 Ca^{\frac{2}{3}}$ $Ca \to 0$
Irandoust and Andersson (1989)	Air/water, Air/ethanol, Air/glycerol Circular (V) 1.0 & 2.0 mm U_{GS} = 0.04- 0.66m/s U_{LS} = 0.04- 0.66m/s	$\dfrac{\delta}{D} = 0.18\left\{1 - \exp\left[-3.08\left(\dfrac{\mu U_G}{\sigma}\right)^{0.54}\right]\right\}$
Aussillous and Quere (2000)	Air/Water Circular (V)	$\dfrac{\delta}{D} = \dfrac{0.66 Ca^{2/3}}{(1 + 3.33 Ca^{2/3})}$

Gas holdup		
Kariyasaki et al. (1991)	Circular (VU,VD) 1, 2.4 & 4.9 mm Rectangular Aspect ratio- 1 to 9 U_{GS}: 0.1-30 m/s U_{LS}: 0.03 – 2.3 m/s	$\varepsilon_G = 1 - \left[1 + 1860\, Eo^{0.75} Fr^{0.95}\, \text{Re}^{-1.03}\, Ca^{0.17}\left(\dfrac{U_{Ls}}{U_{Gs}}\right)\right]^{-1}$
Chung et al. (2004)	Nitrogen / water Circular 0.53,0.25,0.1,0.05 mm U_{LS}= 0.01-5.77 m/s U_{GS}= 0.02 -73 m/s	$\varepsilon_G = \alpha$ for d =0.53mm $\varepsilon_G = 0.833\,\alpha$ for d =0.25mm $\varepsilon_G = \dfrac{0.03\alpha^{0.5}}{1 - 0.97\alpha^{0.5}}$ for d < 0.1 mm
Warnier et al. (2008)	Nitrogen/ water Rectangular(H) 0.1*0.05mm.	$\varepsilon_G = \dfrac{A_B}{A}\alpha$ $\dfrac{A_B}{A}$ is a constant independent of the channel diameter, Operating parameters and fluid properties
Bubble and slug length		
Laborie et al (1999)	Air/water, Air/water-Glycerol, Air/water-Ethyl Alcohol Circular, (V), 1,2,3,4mm diameter ULS = 0.08 - 0.9 m/s UGS = 0.1 – 1 m/s	$\dfrac{L_B}{D} = 0.0878(\dfrac{\text{Re}_{(U_B)}}{Eo^2})^{0.63}$ $\dfrac{L_S}{D} = 3451(\dfrac{1}{\text{Re}_{(U_{GS})}\, Eo})^{1.2688}$ Where $\text{Re}_{(U_B)}$ is based on bubble velocity, $\text{Re}_{(U_{GS})}$ is based on superficial gas velocity.
Liu et al (2005)	Air/water, Air/oil Circular, Square (V)d_H = 0.9-3mm U_{LS}, U_{GS} : 0.008-1m/s	$U_{TP}^{-0.33} L_S^{0.5} = 0.088\, \text{Re}_G^{0.72}\, \text{Re}_L^{0.19}$
Qian and Lawal (2006)	Air/water Circular (H) 0.25, 0.5. 0.75, 1, 2, 3 U_{GS}: 0.05-0.1 m/s U_{LS}: 0.02-0.2 m/s	Slug lengths are dependent on the inlet geometry. $L^* = L^*(\text{Re},Ca,\varepsilon_G)$. $\dfrac{L_G}{D} = 1.637\alpha^{0.107}(1-\alpha)^{-1.05}\, \text{Re}^{-0.075}\, Ca^{-0.0687}$ $\dfrac{L_S}{D} = 1.637\alpha^{-0.893}(1-\alpha)^{-0.05}\, \text{Re}^{-0.075}\, Ca^{-0.0687}$ $\dfrac{L_S + L_B}{D} = 1.637\alpha^{-0.893}(1-\alpha)^{-1.05}\, \text{Re}^{-0.075}\, Ca^{-0.0687}$
Akbar and Ghiassian (2006)	(simulation)	$\dfrac{U_{TP}^{-0.33}}{L_S^{0.5}} = 142.6\alpha^{0.56}(\dfrac{D}{(L_S + L_B)})^{0.42}\, \text{Re}_G^{-0.252}$

2.2. Experimental investigation

2.2.1. Experimental setup

Experiments were conducted using a state of the art 'microreactor rig' designed to carry out reactions using microreactors. The rig consisted of high precision HPLC pumps (LAB Alliance, SSI make range 1-40 ml/min with an accuracy of 0.1 ml/min) for accurate control of liquid flow rate and mass flow controllers (WEST make range 1-40 nml/min with an accuracy of 0.1 ml/min) for controlling gas flow rate. A photograph of the microreactor rig is shown in Figure 2.1. A typical test-section for conducting G-L flow studies in capillaries consists of a 'T' type mixer and test capillary. A schematic of the test-section is shown in Figure 2.2. Since HPLC pumps had lots of inherent fluctuations, the flow becomes discontinuous and periodic. Hence in order to avoid the discontinuity a dampener was introduced just before the liquid enters the 'T' mixer. Another important issue, which needs to be taken care of while conducting the experiments is that of backflow of liquid into the gas pipeline. This was minimized by introducing the needle in the gas flow line.

Figure 2.1: Microreactor rig
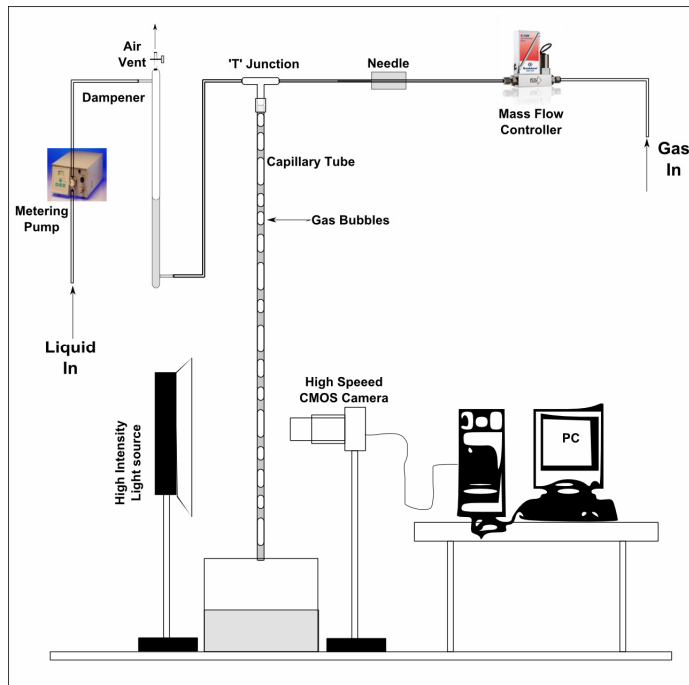
Figure 2.2: Schematic of the Experimental Setup

The 'T' type mixer used for the experiments was a standard stainless steel 1/16" 'T' joint with nut and ferrule arrangements, generally used for connecting gas pipelines used for GC/HPLC purposes. Both gas and liquid inlets are connected with 1/16" (i.d = 1.3mm) steel tubing. The outlet is a 1/16" (i.d = 0.5mm) Teflon tubing, which in turn is connected to the 0.8mm capillary using flexible tube. The details of the above mentioned arrangement is shown in Figure 2.3. Compressed nitrogen cylinder and liquid feed reservoir were used as a source for the gas and liquid respectively. The flow visualization was done using high speed CMOS camera (*Motion Pro Redlake* make) with a suitable lens (*Nikon AF Micro Nikkor* 105 mm 1:2.8 D) capable of capturing images at 2000 *f.p.s*. The camera was positioned at a distance far away from the 'T' mixer (L/D ≥ 100, from the top of the tube). Two liquids namely water and water-glycerol (50%v/v) was used as test fluids. The specification of the liquids is given in Table 2.3.

The inner diameter of the microchannel is measured by filling it with ink and capturing the image. The superficial velocities are varied between 0.04 and 0.8m/s for gas-phase and 0.09 and 1.5m/s for the liquid phase. The flow was recorded for 36 pairs of (gas and liquid)

superficial velocity for the water/Nitrogen system and 30 pairs of superficial velocities for the water-glycerol/nitrogen system. To obtain concordant values, three videos were recorded for each pair of superficial velocity.
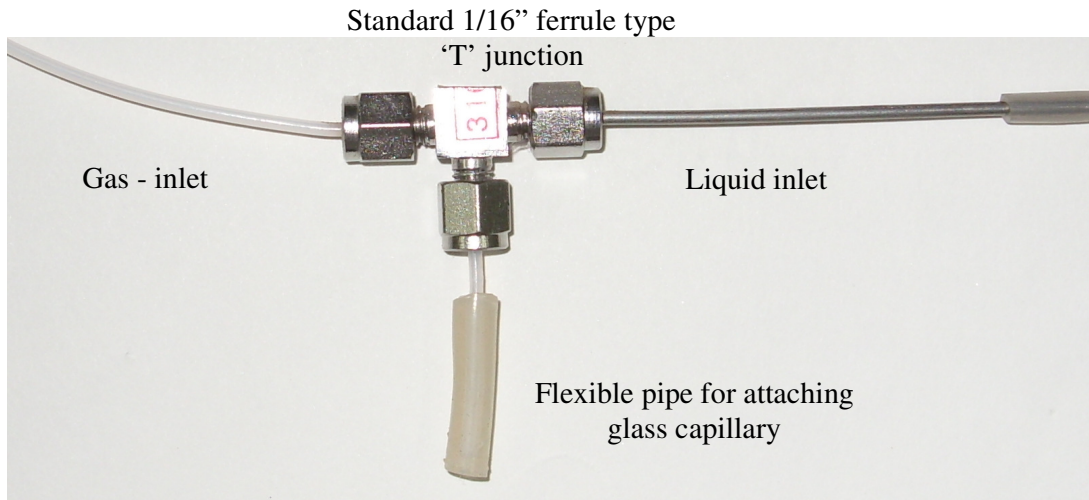
Figure 2.3: 'T' type mixer used for the experiments

Table 2.3: Characteristics of liquids used in experiments

Liquid	Density (Kg/m^3)	Viscosity (10^{-3} Pas)	Surface Tension (10^{-3} Nm^{-1})
Water	1000	1	72
Water-glycerol (50% v/v)	1152.74	6.9	68

2.2.2. Image analysis

Flow regimes were identified using visual observations of the captured movies. However, other hydrodynamic parameters such as bubble/slug lengths/velocities and hold-up were extracted from the movie using a systematic procedure. The incident light deflects at the gas–liquid interface and hence appears to be dark. This is the main principle behind the image analysis procedure discussed.

- The intensity values are measured (for each frame) along vertical line profiles across two cross-sections (called 'top' and 'bottom') separated by a known distance 'L_f', using macro written in a commercial image analysis software IMAGEPRO plus 5.1. The intensity values drops sharply along the gas liquid interface. This principle is used to detect the presence or absence of the bubble at each frame. A typical image and graph of the intensity profile across the capillary in the presence and absence of bubble is shown in Figure 2.4 (a)

- Based on the intensity profile graphs of various frames, a threshold value is set, such that the intensity lower than the threshold indicates the presence of the bubble for a given frame. A code written in MATLAB indexes '0' or '1' value against each frame ('0' denotes absence of bubble and '1' denotes presence of bubble).

- The occurrence of 1 after a 0 indicates the start or rise of the bubble and the occurrence of 0 after a 1 indicate the end or fall of the bubble. A sample graph for the presence of bubble/liquid slug along a top and bottom cross-sectional planes for few frames of a recorded movie are shown in Figure 2.4 (b).
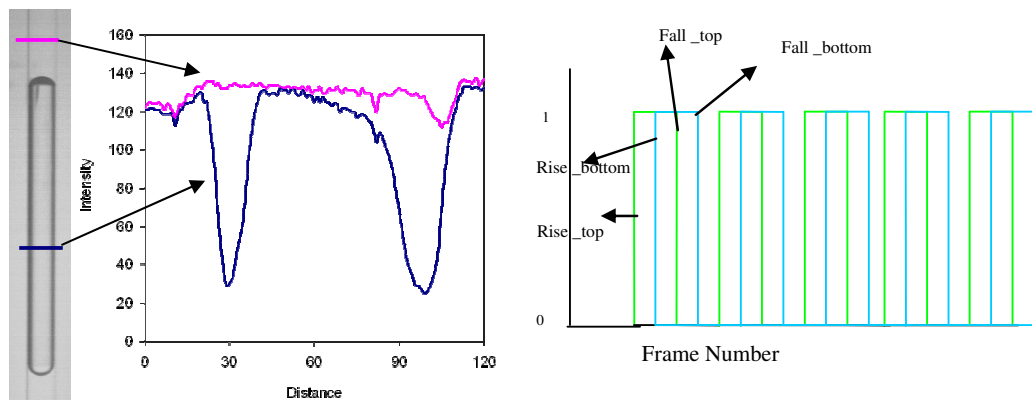
Figure 2.4 (a) Intensity based analysis for the detection of presence/absence of bubble
(b) Rise and Fall series measured at two different locations

15

- The rise and fall of the bubble across the 'top' and 'bottom' cross sections are stored in arrays R_{top}, R_{bottom}, F_{top} and F_{bottom} respectively. Minor adjustments are made such that $R_{top,i}$ and $R_{bottom,i}$ corresponds to the same bubble (by discarding the initial bubbles that have already passed 'top' before frame 1).In case of Taylor bubble train flow where the bubbles move very close to each other, there are chances that intensity analysis misses the fall of the bubbles at one or both cross-sections, (and hence overestimating the length). In such cases, manual adjustments are made by referring the corresponding frames.

- The lag which is measured as the difference between the indexed rise and fall series at the top and bottom, and stored in arrays λ_1 and λ_2 respectively and their arithmetic average is stored in the array λ. The lag when divided by the frame speed (2000 frames per second) gives the time taken by the bubble (τ) taken by the bubble to travel the distance L_f. Hence speed is obtained as L_f/τ.

- "Number of pixels per mm" is obtained by calibration of the image with the help of the channel internal diameter. In water-nitrogen system the internal diameter is clearly seen. But the refractive index of water-glycerol solution and glass are nearly the same(η_{glass} =1.47, $\eta_{glycerol}$ =1.4729) , so the internal diameter is not seen in the images. So, the contrast enhancement is done to locate the inner diameter and find out the value of pixels/mm (Figure 2.5)

- Bubble/slug length is then calculated by multiplying the bubble velocity with the respective difference of rise and fall for any of the top or bottom series divided by pixels/mm. The number of elements of the arrays indicates the number of bubbles.

- Once the velocities of the bubbles are obtained, an average of all the bubble velocity is used to calculate the film thickness using various correlations available for film thickness as discussed in Table 2.2

Figure 2.5 (a) Channel (inner) diameter not visible in water-glycerol/nitrogen system (b) channel (inner) diameter made visible on contrast adjustment

- Further assuming the shape of the bubble to be cylindrical, volume of each bubble is calculated. Necessary correction factors are multiplied to the volume of bubble for bubbles with hemispherical and elliptic ends. For necked tail (observed in water-glycerol/Nitrogen system), the correction factors are calculated by measuring the length and diameter of the necked portion. Similarly volume of the each slug is also calculated. Volume of liquid in the film is accounted by considering the volume of the annular region around the bubble and slug. Ratio of sum of all volumes of gas bubble to that the sum of volumes of gas and liquid gives the time averaged gas hold-up of the system.

- The holdup is also calculated as the ratio of gas superficial velocity to bubble velocity ($U_{GS}/\overline{U_B}$) as proposed by Wallis (1969), and the accuracy of the correlations of liquid film thickness are tested.

- The averages (bubble velocity, bubble/slug lengths) are calculated by taking the number average of respective parameter for all the measured bubbles/slugs.

The equations mentioned in Table 2.4 sums up the above-mentioned procedure.

Table 2.4: Equations used in image analysis for the determination of hydrodynamic parameters in slug flow

$$\lambda_{1,i} = R_{bottom,i} - R_{top,i} \qquad \lambda_{2,i} = F_{bottom,i} - F_{top,i} \qquad \lambda_i = \frac{\lambda_{1,i} + \lambda_{2,i}}{2}$$

$$\tau_i = \frac{\lambda_i}{f.p.s}$$

$$L_f = \frac{Total\ no\ of\ pixels\ between\ two\ cross-sectional\ planes}{Pixels/mm}$$

$$U_{B,i} = \frac{L_F}{\tau_i}$$

$$L_{B,i} = \frac{U_{B,i} * (R_{bottom,i} - F_{bottom,i})}{Pixels/mm} \qquad L_{Slug,i} = \frac{U_{B,i} * (F_{bottom,i} - R_{bottom,i+1})}{Pixels/mm}$$

$$\overline{U_B} = \frac{\sum_i U_{B,i}}{\sum i} \qquad \overline{L_B} = \frac{\sum_i L_{B,i}}{\sum i} \qquad \overline{L_{Slug}} = \frac{\sum_i L_{Slug,i}}{\sum i}$$

$$U_{B,max} = \underset{i}{Max}(U_{B,i}) \qquad L_{B,max} = \underset{i}{Max}(L_{B,i}) \qquad L_{Slug,max} = \underset{i}{Max}(L_{Slug,i})$$

$$U_{B,min} = \underset{i}{Min}(U_{B,i}) \qquad L_{B,min} = \underset{i}{Min}(L_{B,i}) \qquad L_{Slug,min} = \underset{i}{Min}(L_{Slug,i})$$

$$Ca = \frac{\mu \overline{U_B}}{\sigma} \qquad d_B = D - 2\delta$$

$$V_{B,i} = \frac{\pi}{4}(d_B)^2 L_{B,i} * C.F \qquad \text{where } C.F \text{ is the shape correction factor}$$

$$V_{Slug,i} = \frac{\pi}{4}(d_B)^2 L_{Slug,i} + V_{B,i} * (1 - C.F)$$

$$V_{film,i} = \frac{\pi}{4}[D^2 - (d_B)^2](L_{B,i} + L_{S,i})$$

$$\varepsilon_G = \frac{\sum_i V_{B,i}}{\sum_i (V_{B,i} + V_{film,i}) + \sum_{i-1}(V_{Slug,i})}$$

$$\varepsilon_G = \frac{U_{GS}}{U_B}$$

2.3. Results and discussion

2.3.1. Flow patterns

Actual snapshots of the gas-liquid flows observed in the present circular micro-channel (0.84mm) at different gas and liquid flow rates are shown in Figure 2.6 (nitrogen-water) and Figure 2.7 (nitrogen-glycerol-water (50% v/v)). For the range of operating conditions studied, slug flow pattern was expected to prevail, however different sub-flow patterns of slug flow were observed. Depending on their interfacial configuration these flow patterns were classified as Periodic single Taylor bubble pattern (P1), Periodic two/three Taylor bubble pattern (P2) , Pseudo-periodic random Taylor bubble pattern (P3), Taylor bubble train flow (P4), Annular flow (P5)

- **Periodic single Taylor bubble pattern (P1):** This pattern consists of periodic occurrence of Taylor bubbles that are longer than the tube diameter followed by liquid slugs. The length of the gas bubbles and liquid slugs remained constant throughout the experimental run. Such a flow pattern occurs at approximately equal and (Figure 2.8) relatively low superficial gas and liquid velocities ($We_{UTP} < 0.003$, Figure 2.9). These flows are completely dominated by surface tension forces. A unit cell representative of the flow consists of a Taylor bubble of length L_B followed by liquid slug of length L_S

- **Periodic two/three Taylor bubble pattern (P2):** This pattern consists of periodic occurrence of Taylor bubbles of either two or three different lengths followed by liquid slugs. The lengths of the succeeding bubble are always smaller then the preceding bubble. However, no such pattern is observed for liquid slugs. This flow pattern is also surface tension dominated ($We_{UTP} < 0.01$, Figure 2.9), however, inertial forces tend to break the bigger size bubble into smaller two/three size bubbles. A unit cell representative for the flow of two bubble pattern consists of bubble of length (L_{B1}) followed by average slug length between the two/three bubbles (L_S) followed by second bubble of length (L_{B2}) followed by second liquid slug of length (L_S).

- **Pseudo-periodic random Taylor bubble pattern (P3)**: As the superficial velocities increases, the randomness in the system increases. A single large Taylor-bubble is

19

followed by large number of irregular size bubbles separated by liquid slugs. However, such an occurrence is also periodic, hence the flow pattern is named pseudo-periodic random Taylor bubble pattern. Here the inertial forces are comparable to surface tension forces ($We_{UTP} \approx 0.01$, Figure 2.9).

- **Taylor bubble train flow (P4)**: This flow pattern is characterized by occurrence of a "train of bubbles", formed by 2-6 Taylor bubbles with a clear interface between any two consecutive bubbles. Number of bubbles forming the train is not fixed and flow pattern is pseudo-periodic. Such a flow pattern was also observed by Fukano and Kariyasaki (1993) and Mishima and Hibiki (1996) but didn't classify them as a separate flow pattern. Chen et al (2002) was the first to classify it as a separate flow pattern. Zhao and Reskallah (1993) also reported similar flow patterns for large pipes in microgravity. They called it froth flow, which occurred in the transition region between slug flow and annular flow. The transition to Taylor bubble train flow occurs when the inertial forces overcomes the surface tension forces ($We_{UTP} > 0.01$, Figure 2.9). Interestingly, the inertial forces are sufficient enough to bring the bubbles near to each other, but are insufficient to rupture the interface and form a single unit. This flow pattern along with P3 can also be considered as a transition regime from Slug/Taylor to annular flow

- **Annular flow (P5)**: When the inertial forces of the gas phase become high enough to rupture the interface between the bubbles, the flow becomes annular (P5) and is characterized by a thin wavy liquid film flowing along the wall with a mist of gas and entrained liquid in the core. This occurs when U_{GS}/U_{LS} exceeds a threshold value. Jayawardene et al. (1997) during his studies on flow patterns in microgravity and reported that this threshold value of U_{GS}/U_{LS} increases with increase in the Suratman number ($\frac{\sigma D \rho_L}{\mu_L{}^2}$) of the system. Our experiments are in agreement with this observation. For water-glycerol/Nitrogen system with a lower Suratman number (1.38×10^3) the transition to annular takes place at U_{GS}/U_{LS} = **6** (as shown in Figure 2.9(b)), while for water/Nitrogen system with a higher Suratman number (6.05×10^4) the threshold value of U_{GS}/U_{LS} is higher and not within the range covered here.

(a)	(b)	(c)	(d)	(e)	(f)
P1	P1	P1	P2	P2	P5

U_{LS} = 0.036 m/s

(a)	(b)	(c)	(d)	(e)	(f)
P1	P1	P1	P2	P2	P5

U_{LS} =0.090 m/s

(a)	(b)	(c)	(d)	(e)	(f)
P1	P1	P2	P2	P2	P5

U_{LS} =0.177 m/s

(a)	(b)	(c)	(d)	(e)	(f)
P1	P2	P2	P3	P3	P4

U_{LS} = 0.270 m/s

(a)	(b)	(c)	(d)	(e)	(f)
P2	P3	P3	P3	P3	P3

U_{LS} = 0.354 m/s

(a)	(b)	(c)	(d)	(e)	(f)
P3	P3	P3	P4	P4	P5

U_{LS} = 0.706 m/s
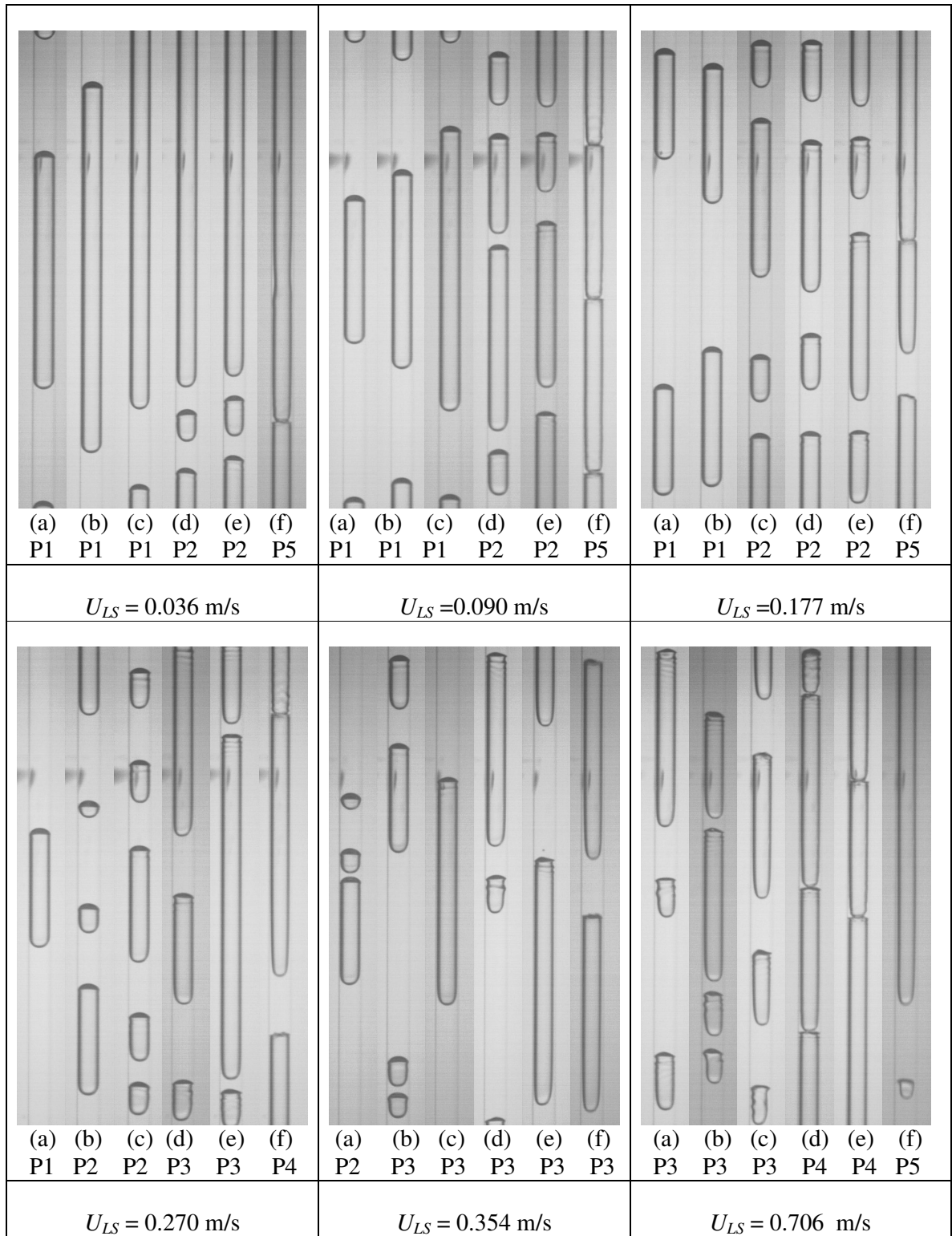
Figure 2.6 Actual snapshots of water-nitrogen flows in 0.84mm capillary (a) U_{GS}= 0.088m/s, (b) U_{GS} = 0.155 m/s, (c) U_{GS} = 0.283 m/s, (d) U_{GS} = 0.408 m/s, (e) U_{GS} = 0.542 m/s and (f) U_{GS} = 1.286 m/s

21

(a)	(b)	(c)	(d)	(e)	(f)	
P1	P1	P5	P5	P5	P5	

$U_{LS} = 0.036$ m/s

(a)	(b)	(c)	(d)	(e)	(f)
P1	P1	P1	P2	P5	P5

$U_{LS} = 0.090$ m/s

(a)	(b)	(c)	(d)	(e)	(f)
P1	P1	P1	P2	P2	P5

$U_{LS} = 0.177$ m/s

(a)	(b)	(c)	(d)	(e)	(f)
P1	P1	P2	P4	P4	P1

$U_{LS} = 0.270$ m/s

(a)	(b)	(c)	(d)	(e)	(f)
P1	P2	P2	P4	P4	P1

$U_{LS} = 0.354$ m/s
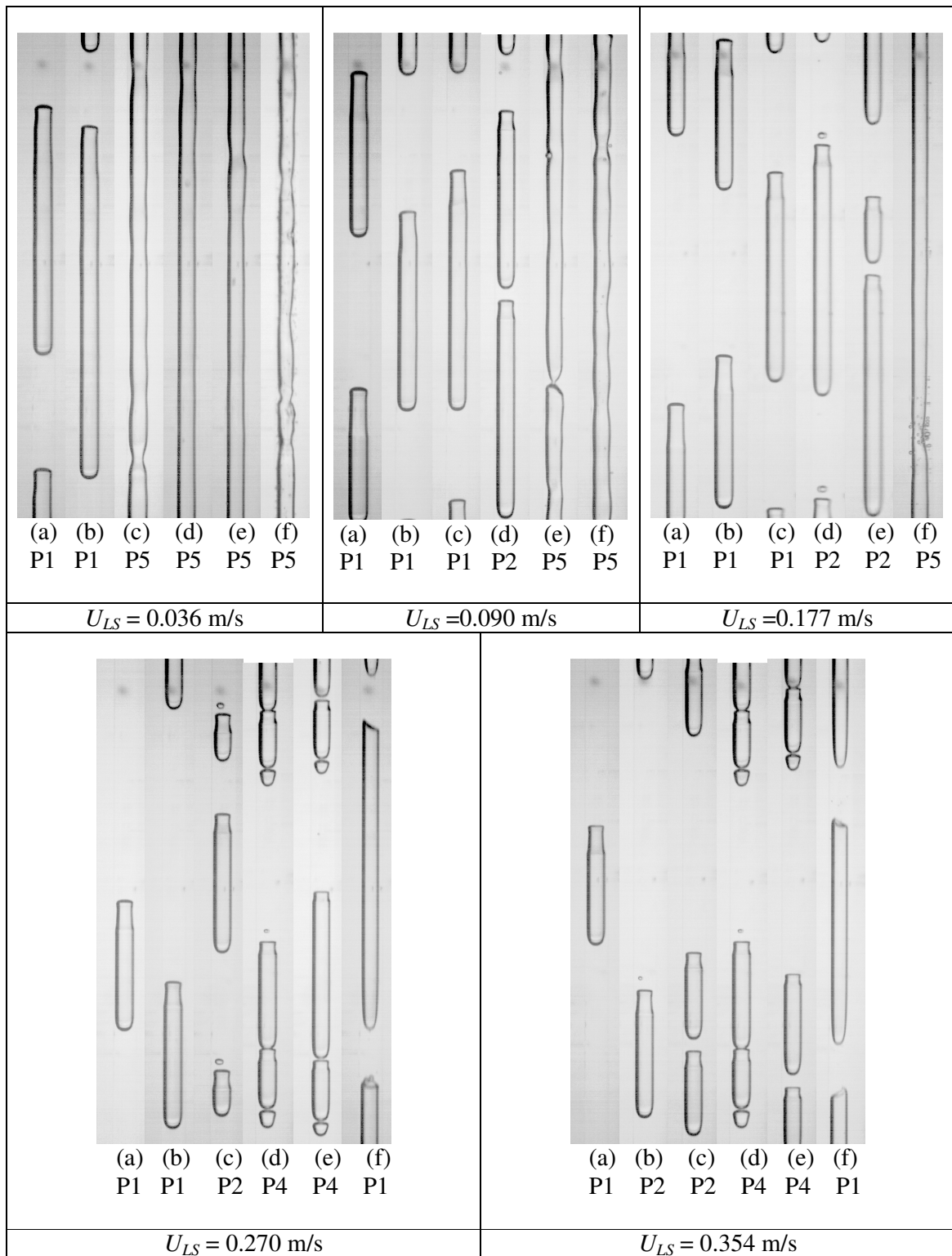
Figure 2.7: Actual snapshots of water-glycerol/nitrogen flows in 0.84mm capillary (a) $U_{GS} = 0.088$ m/s, (b) $U_{GS} = 0.155$ m/s, (c) $U_{GS} = 0.283$ m/s, (d) $U_{GS} = 0.408$ m/s, (e) $U_{GS} = 0.542$ m/s and (f) $U_{GS} = 1.286$ m/s
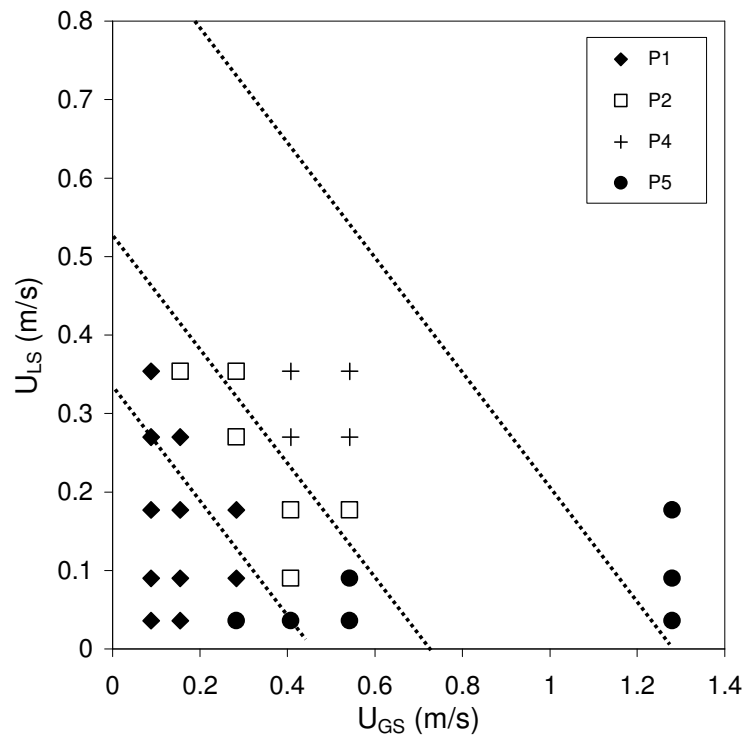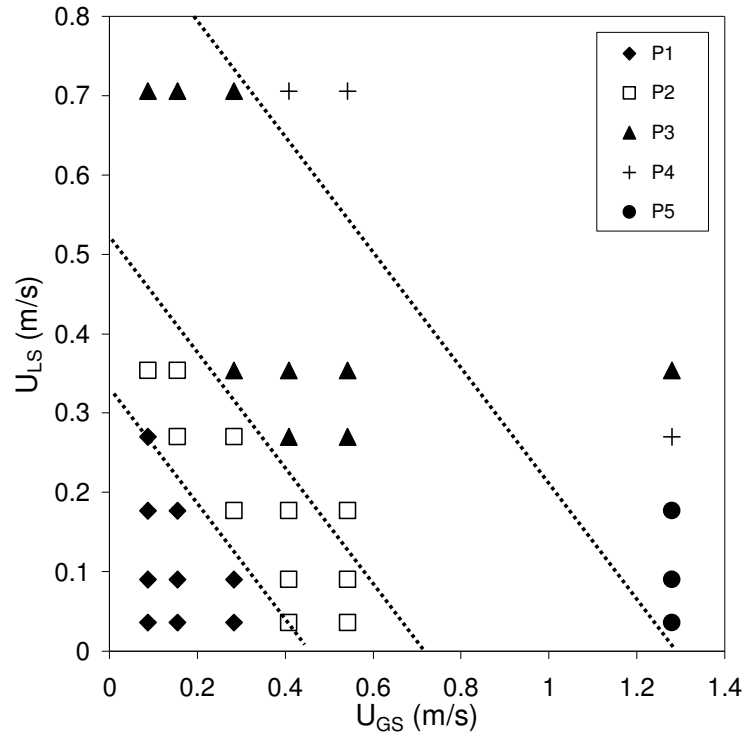
Figure 2.8: U_{LS} vs. U_{GS} flow pattern map (a)Water/Nitrogen system (b)Water-glycerol/Nitrogen system
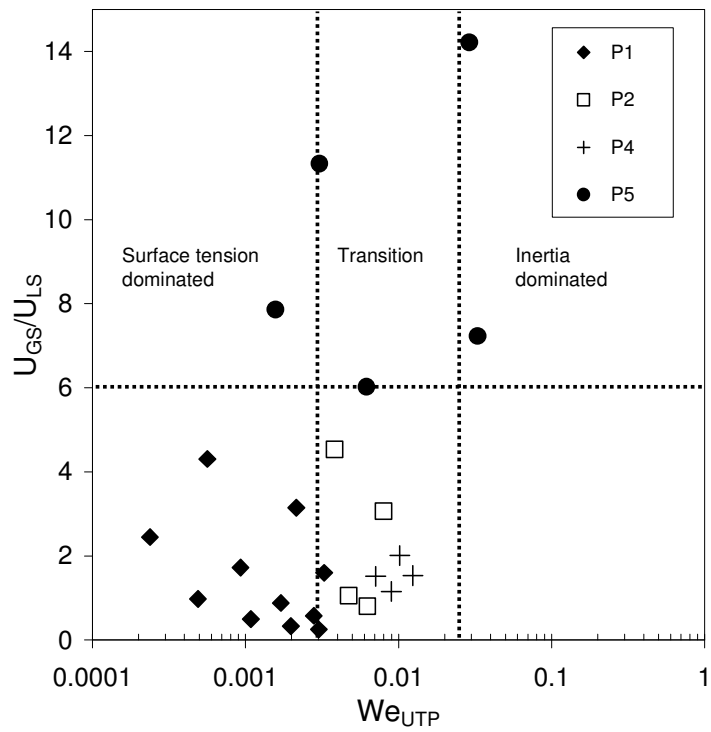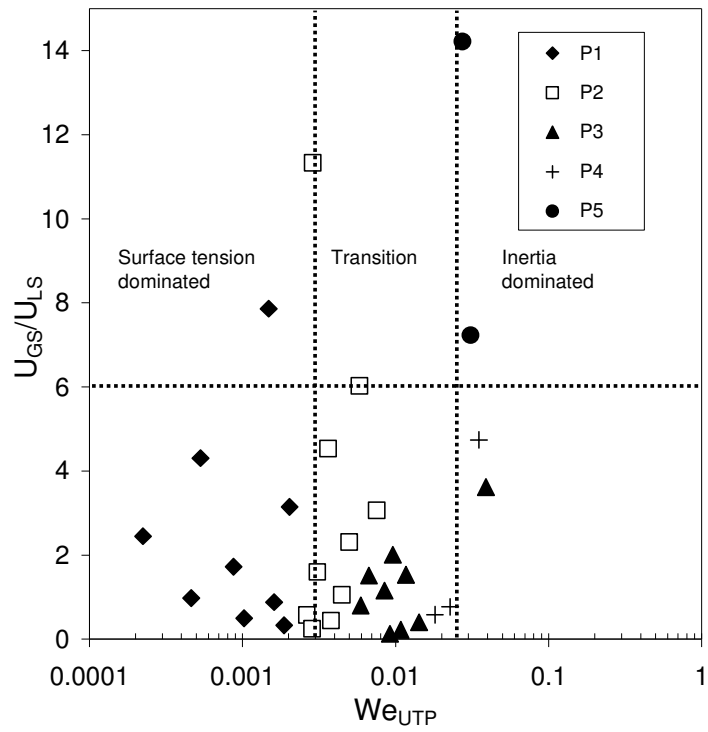
Figure 2.9: U_{GS}/U_{LS} vs. We_{UTP} flow pattern map (a)Water/Nitrogen system (Suratman number = 6.05×10^4) (b) Water-glycerol/Nitrogen system (Suratman number = 1.38×10^3)

The ranges of dimensionless parameters relevant to the present two-phase microchannel flow experiment are shown in Table 2.5. These values indicate the relative significance of the forces in the flow field (inertial force $\approx$ surface tension force > viscous force >> gravity $\approx$ buoyancy).

Table 2.5: Dimensionless parameters

Dimensionless Parameter	Definition	Water /Nitrogen	Water-Glycerol /Nitrogen
Eotvos number (Eo)	$\dfrac{Buoyancy\ force}{Surface\ tension\ force} = \dfrac{(\rho_L - \rho_G)gD^2}{\sigma}$	0.096	0.117
Bond number (Bo)	$\dfrac{Gravitational\ force}{Surface\ tension\ force} = \dfrac{\rho_L gD^2}{\sigma}$	0.096	0.117
Reynolds number (Re)	$\dfrac{Inertial\ force}{Viscous\ force} = \dfrac{\rho_L UD}{\mu}$	108-867	18-168
Capillary number (Ca)	$\dfrac{Viscous\ force}{Surface\ tension\ force} = \dfrac{\mu U_B}{\sigma}$	0.001-0.02	0.01-0.2
Weber Number (We)	$\dfrac{Inertial\ force}{Surface\ tension\ force} = \dfrac{\rho_L U_{TP}^2 D}{\sigma}$	0.09-15	0.1-17
Suratman number (Su)	$\dfrac{\sigma D \rho_L}{\mu_L^2}$	6.05×10^4	1.38×10^3

2.3.2. Bubble shape

Bubble shape is one of the important parameters influencing the streamline patterns in the liquid slug. For circular capillaries the body of bubble is always cylindrical, however, what changes is the head and tail of the bubble. The shape of the head/nose varies from perfectly hemispherical shape to prolate/elliptical shape at higher superficial velocities. The shape of the tail varies from perfectly hemispherical to oblate/flat necked and was found to be a strong function of Capillary number (Figure 2.10). At Capillary number ≤ 0.001 the bubble shows perfectly hemispherical cap at both top and bottom. With increasing Capillary number ($Ca \approx 0.01$) the tail becomes flat and wavy with noticeable undulations. Further increase shows a neck like formation at the tail of bubble. When the degree of necking increases, the Taylor

bubble tail becomes distorted and the necked portion is shed in the form of a small spherical bubble.
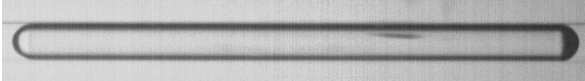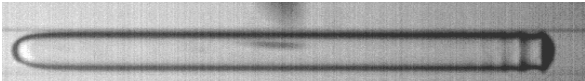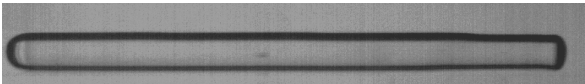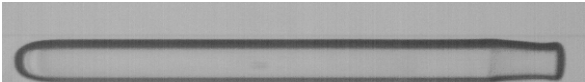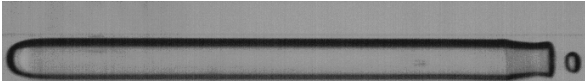
Spherical tail	$Ca = 0.0018$	
Flat tail	$Ca = 0.0067$	Increasing Capillary number
Wavy tail	$Ca = 0.0134$	
Necked tail	$Ca = 0.0307$	
Bubble shed when necking increases	$Ca = 0.0796$	

Figure 2.10: Bubble tail shapes

2.3.3. Bubble velocity

Figures 2.11 (a) and (b) represent the variation of time averaged bubble velocity (U_B) with superficial gas velocity (U_{GS}) for varying superficial liquid velocities (U_{LS}) for water-nitrogen and water-glycerol nitrogen systems respectively. An increase in U_B with increase in either U_{GS} or U_{LS} is observed, with relationship being linear. The effect of the variation in the physical properties such as surface tension and viscosity (water-glycerol nitrogen system) is found to increase the bubble velocity by an order of 10-20%. The results are consistent with the observations of Liu et al. (2005) and Kreutzer (2003) who reported increase in bubble velocity for high viscosity and lower surface tension fluids.

Correlating the Taylor bubble velocity in a capillary tube with system and operating parameters has been an objective of study for many researchers (Fukano and Kariyasaki, 1993; Mishima and Hibiki, 1996; Laborie et al. 1999, Chen et al. 2002, Liu et al. 2005 and Warnier et al. 2008). Most of them found the drift flux model provided by Zuber and Findlay (1969) (for larger size channels) and its variant modified drift flux useful with predictions for estimating bubble velocity within an error range of 5-10%. However the constants C_0 and C_1 involved in these correlations were found to be dependent on parameters such as tube diameter and liquid physical properties serving as a drawback to this method.

Figure 2.12 shows variation of average bubble velocity versus the overall superficial velocity U_{TP}. A correlation of the form of the drift flux model $U_B = C_o U_{TP} + C_1$ gives

$$U_B = 1.2161 U_{TP} - 0.0502 \quad \text{(water / nitrogen system) and} \qquad \textbf{2.1}$$
$$U_B = 1.541 U_{TP} - 0.1073 \quad \text{(water-glycerol / nitrogen system)} \quad \textbf{2.2}$$

The above correlation predicts the velocities within an error of 3.75 % and 6.15% for the respective systems. The results are in agreement with Laborie et al. (1999) who reported values of $C_0 = 1.24$ for water/air system and 1.56 for water-nitrogen (46% w/w)/ air system in a 1mm capillary.
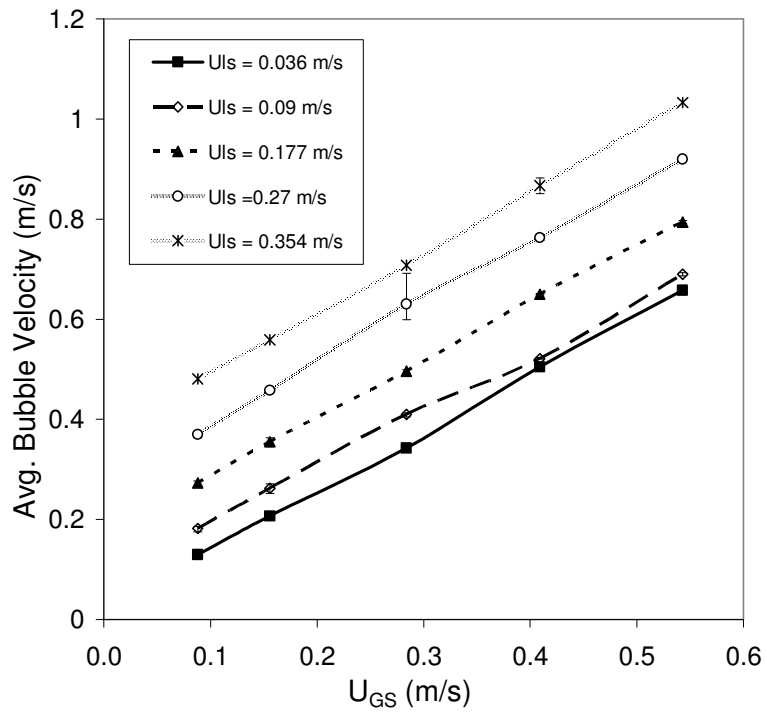
(a) Water/nitrogen system
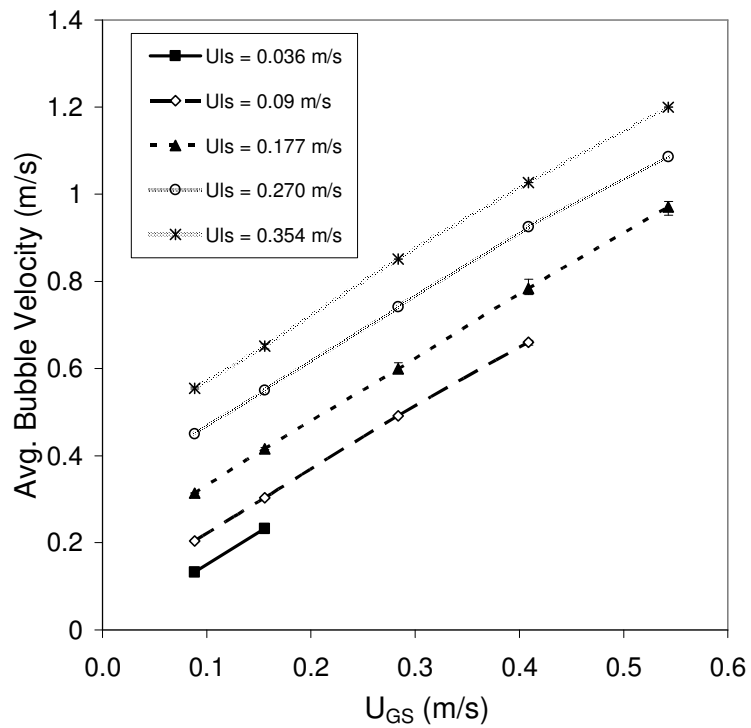
(b) Water-glycerol / nitrogen system

Figure 2.11: Variation of time averaged bubble velocity (U_B) with superficial gas velocity(U_{GS})
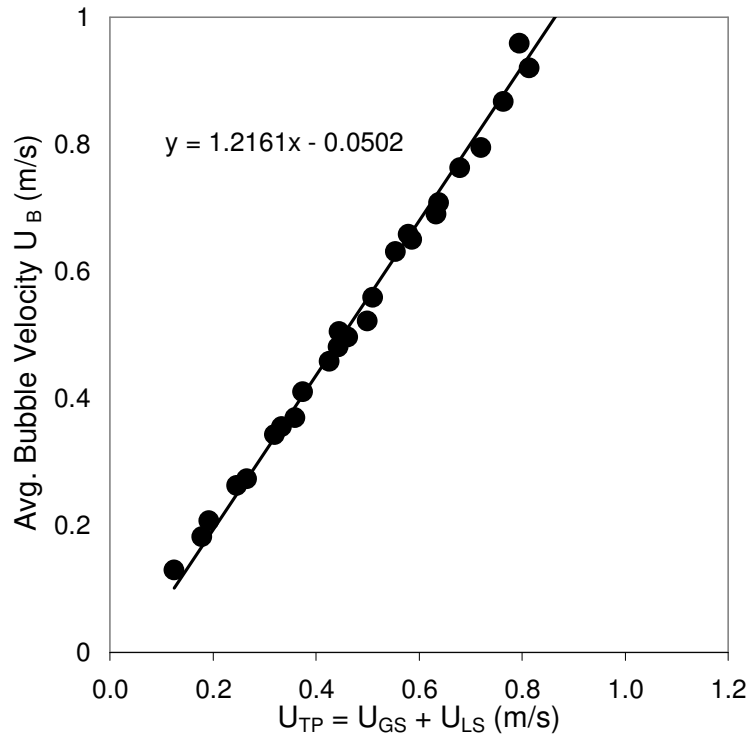
(a) Water/nitrogen system
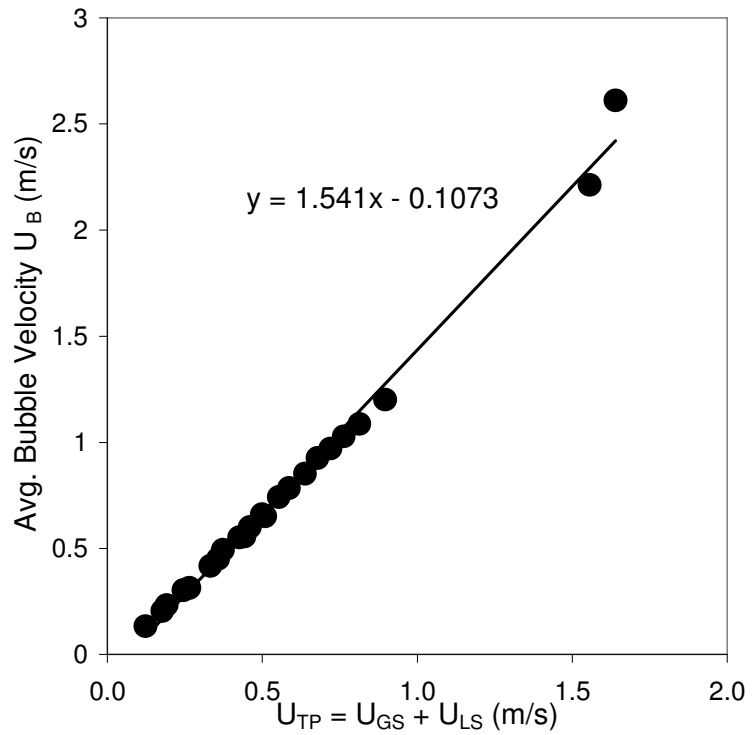
(b) Water-glycerol / nitrogen system

Figure 2.12: Average bubble velocity (U_B) vs U_{TP} plots for 0.84mm capillary

The drift flux distribution parameter $\left(U_B \middle/ U_{TP} \right)$ as discussed by Liu et al. 2005 was found to be an increasing function of the Capillary number. The dimensionless relative bubble velocity, $W = \dfrac{U_B - U_{TP}}{U_B}$ (which is also the ratio of area occupied by the film to the total cross-sectional area of the channel $\dfrac{A - A_B}{A}$) was plotted against Capillary number (Figure 2.13(a)). It was observed that W increases sharply with Ca, and then asymptotes to a value of ~0.35. Similar observations were also found for the experimental data of Liu et al. (2005) (Figure 2.13 (b)). This indicates that the increase in film thickness becomes constant beyond $Ca > 0.35$.

2.3.4. Film thickness

No experimental measurements were made for the determining the film thickness. Different theoretical and empirical correlations available in the literature for predicting film thickness were used to estimate the gas holdup for all sets of experimental data. The estimated holdup values were compared with the holdup calculated using $\varepsilon_G = \dfrac{U_{GS}}{U_B}$. Figures 2.14 & 2.15 show the parity plot between the two holdups calculated for water/nitrogen and water-glycerol/nitrogen respectively. For water/nitrogen system (Ca varies from 10^{-3} to 10^{-2}) all the correlations used gave accurate prediction. For water-glycerol/nitrogen system (Ca varies from 0.01-0.2), Bretherton's correlation showed the minimum prediction showing that lubrication analysis is not valid for higher Capillary numbers. The Fairbrother and Stubbs correlation and Aussilous and Quere correlation were found to show reasonably good prediction. However, Aussilous and Quere correlation is recommended because of the sound theoretical reasoning and ability to account for higher Capillary numbers ($Ca>1$) too, as reported in literature.
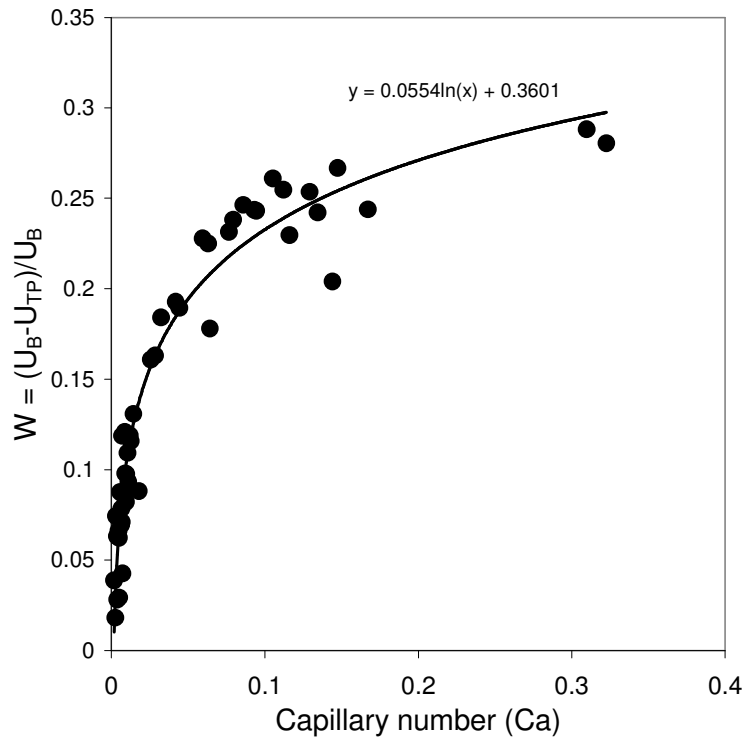
(a)
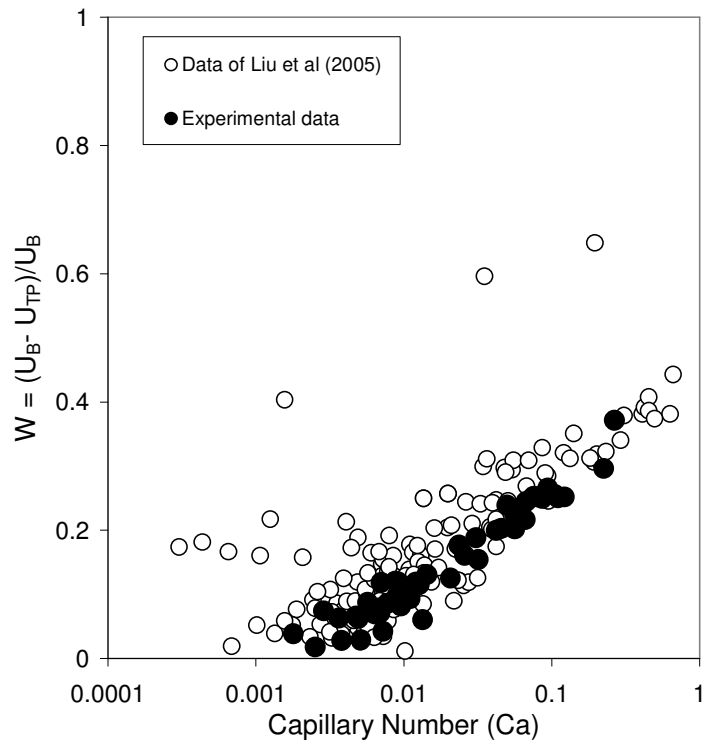
(b)

Figure 2.13: *W* vs *Ca* plot (a) Our experimental data (b) Experimental data of Liu et al.(2005)
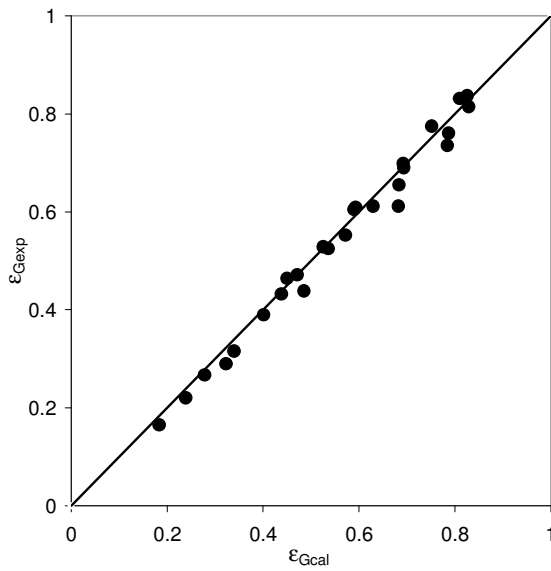
(a) Aussilous and Quere correlation
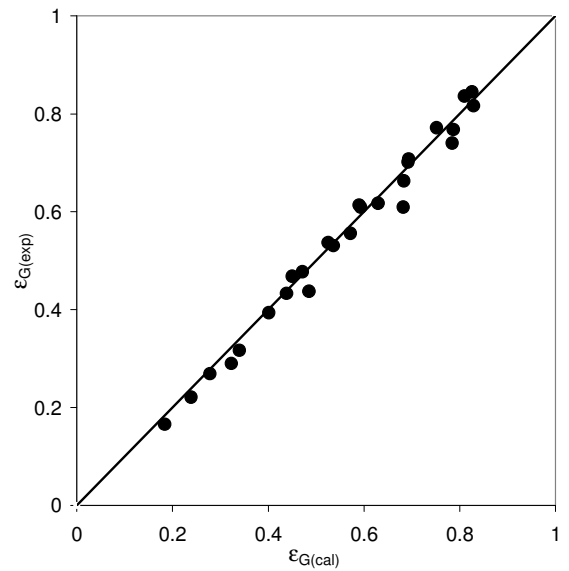
(b) Fairbrother and Stubbs correlation
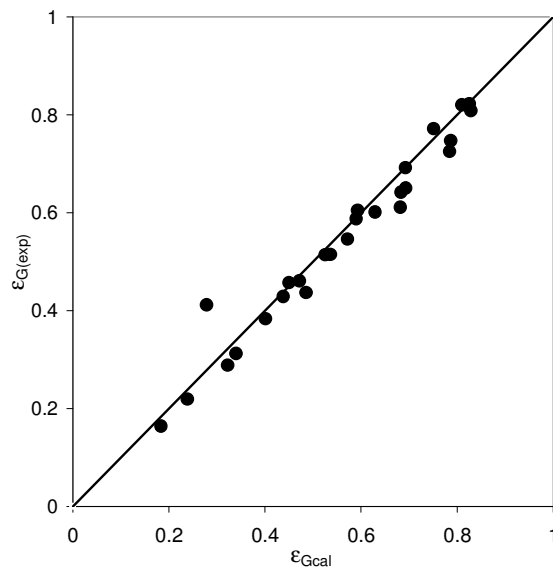
(c) Bretherton correlation

Figure 2.14: Parity plot of the calculated holdup vs those observed experimentally using different correlations for water/nitrogen system
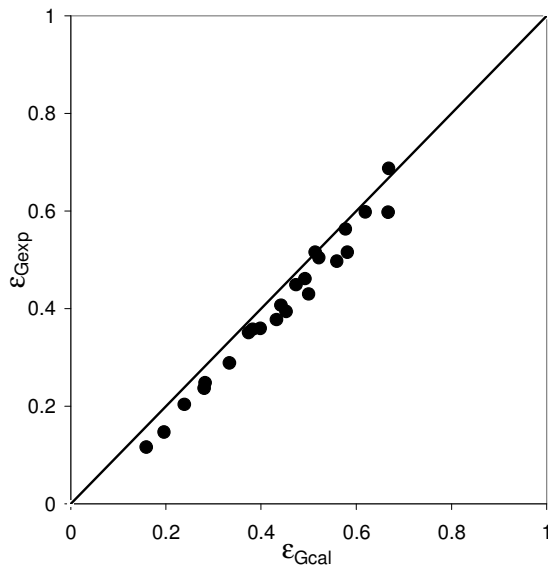
(a) Aussilous and Quere correlation
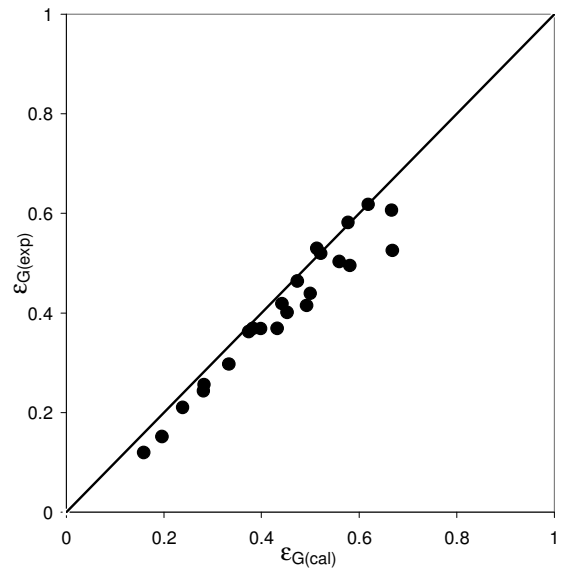
(b) Fairbrother and Stubbs correlation
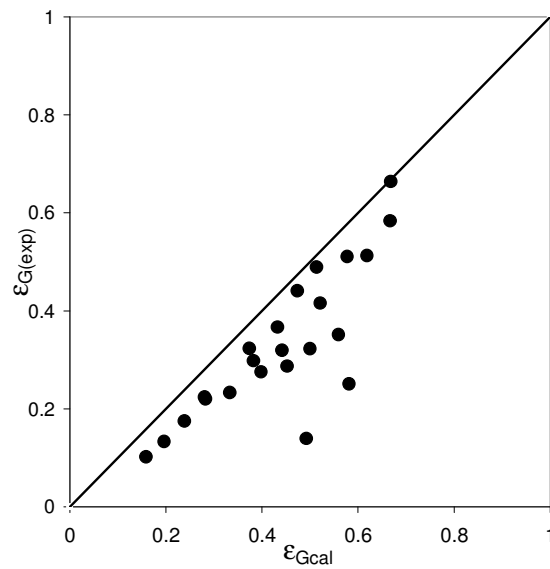
(c) Bretherton correlation

Figure 2.15: Parity plot of the calculated holdup vs those observed experimentally using different correlations for water-glycerol/nitrogen system

2.3.5.   Gas holdup

The variations of gas holdup (ε_G) with U_{GS} for varying U_{LS} for water-nitrogen and water-glycerol-nitrogen system are shown in Figure 2.16 (a) and (b) respectively. The figure shows that the gas holdup increases with increase in superficial gas velocities and decrease in superficial liquid velocities and vice-versa.

We know that for homogeneous flow, gas holdup (ε_G) is given as $\left(\varepsilon_G = \alpha = \dfrac{U_{GS}}{U_{GS} + U_{LS}} \right)$

hence the ratio $\dfrac{\varepsilon_G}{\alpha}$ can be used as a parameter for measuring the deviation from homogeneity. For homogeneous flow $\dfrac{\varepsilon_G}{\alpha} = 1$. Also we know that in slug flow the Taylor bubble velocity and the liquid slug velocity are same thus we get

$$\frac{U_{GS}}{\varepsilon_G} = \frac{U_{LS}}{\varepsilon_S} \tag{2.3}$$

Where
$$\varepsilon_S = 1 - \varepsilon_G - \varepsilon_{Lf} \tag{2.4}$$

$$\varepsilon_G = (1 - \varepsilon_{Lf}) \frac{U_{GS}}{U_{GS} + U_{LS}} \tag{2.5}$$

Since the liquid film forms a uniform continuous phase, ε_{Lf} is given by the ratio of the area occupied by the liquid film to the area of the bubble

$$\varepsilon_{Lf} = \frac{A - A_b}{A} \tag{2.6}$$

$$\varepsilon_G = \frac{A_b}{A} \frac{U_{GS}}{U_{GS} + U_{LS}} \quad \therefore \quad \frac{\varepsilon_G}{\alpha} = \frac{A_b}{A} \tag{2.7}$$

$\dfrac{A_B}{A}$ decreases with increase in Capillary number. Hence, the deviation from homogenous flow increases with increase in Capillary number. Figure 2.17 shows variation of gas holdup (ε_G) with volumetric quality $\left(\alpha = \dfrac{U_{GS}}{U_{GS} + U_{LS}} \right)$ similar to one given by Armand (1946). As expected the degree of non homogeneity was lesser for water/nitrogen system (0.9) as compared to water-glycerol/nitrogen system (0.765).
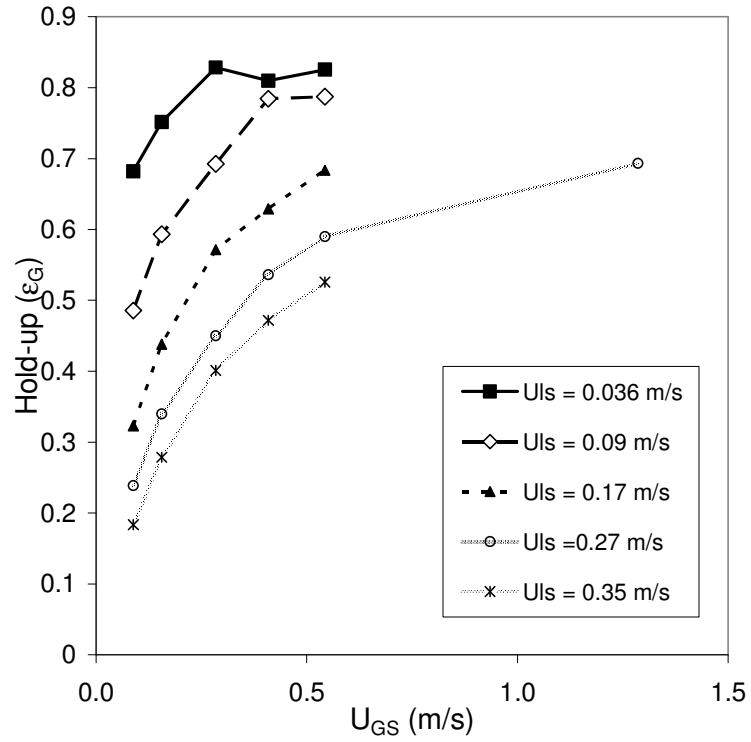
(a) Water/nitrogen system
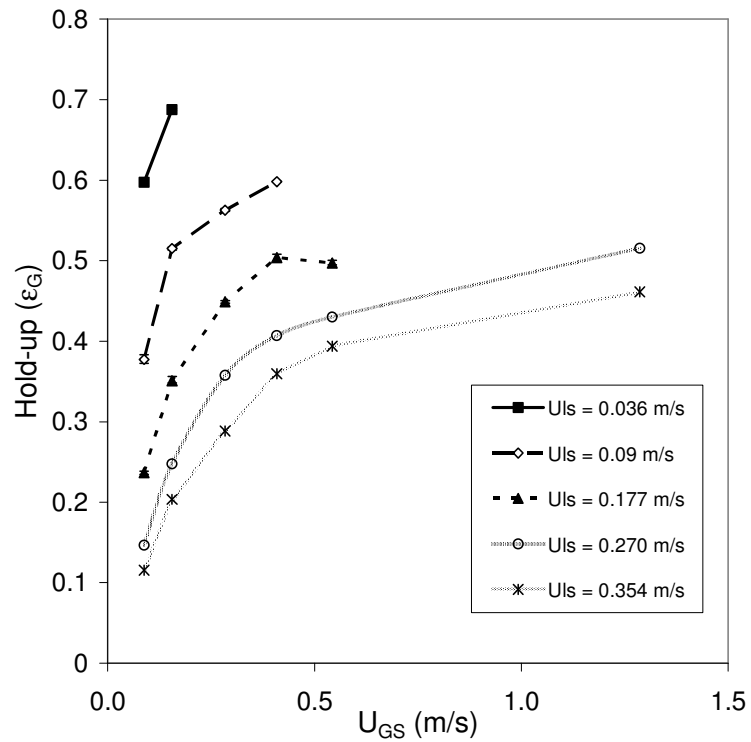
(b) Water-glycerol / nitrogen system

Figure 2.16: Variation of time averaged gas-holdup (ε_G) with superficial gas velocity (U_{GS})
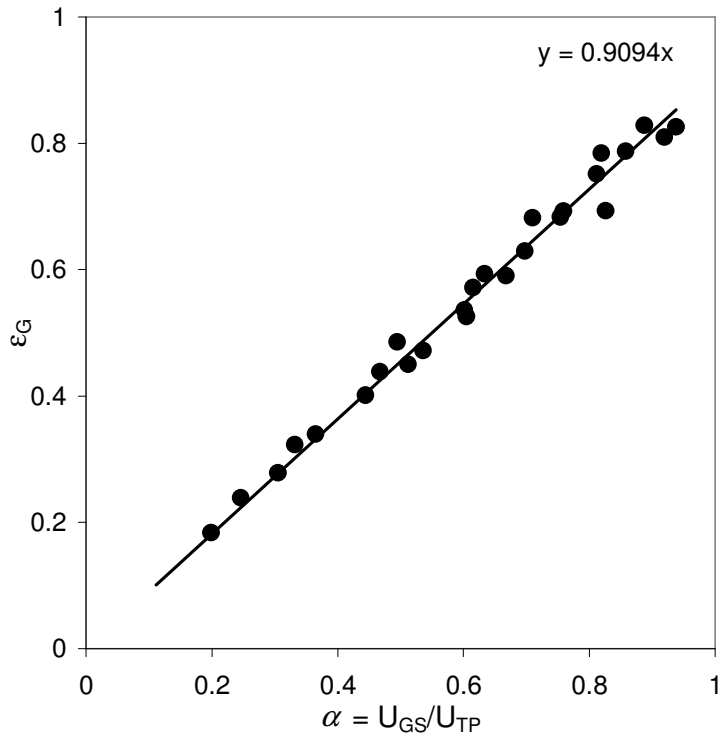
(a) Water/nitrogen system
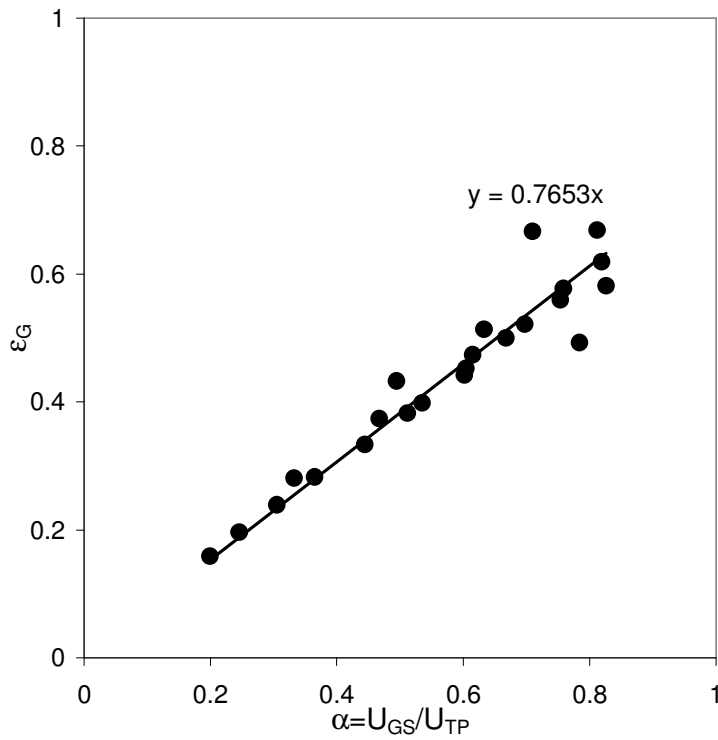
(b) Water-glycerol / nitrogen system

Figure 2.17: Armand type plot for gas holdup (ε_G)

2.3.6.   Bubble and slug length

Bubble and slug lengths are generally not discussed in the literature because of their complex dependence on the inlet geometry. In our experiments the average bubble length varied between 3D - 30D and slug length varied between 2D - 15D respectively. Tables 2.6 (a) and 2.6 (b) gives the details of variation of minimum maximum and average bubble and slug lengths for all sets of gas-liquid flow rates studied for water/nitrogen and water-glycerol /nitrogen system respectively.

Figures 2.18 and 2.19, show variation of average bubble and slug length with superficial gas velocity at different superficial liquid velocities for water-nitrogen and water-glycerol nitrogen system. It shows that the bubble length initially increases with increasing gas velocity. However, once a particular length is reached the transition from single Taylor bubble regime to 2-3 Taylor bubble regime occurs and bubble tend to break into a bigger bubble followed by a smaller bubble.

Different correlations are discussed in the literature for predicting bubble and slug lengths (Table 2.2). As can be seen most of researchers have tried to correlate the lengths with relevant dimensionless numbers for flow in capillaries. However there is a huge gap between any two of these correlations. This is primarily because the lengths are strong function of the type of inlet used for study, which is not accounted in the correlation. Also observed from most of the correlations is that, the lengths are strong function of volumetric quality $\left(\alpha = \dfrac{U_{GS}}{U_{GS} + U_{LS}} \right)$ or Reynolds number of the respective phase and are weak function of Capillary number (Qian and Lawal 2006) indicating negligible effect of system properties (surface tension and viscosity).

Figure 2.20 shows the comparison of the correlation of Laborie et al. (1999) and Qian and Lawal (2006) with our experimental data. The Laborie's correlation is in complete disagreement with our data. This could be because the correlation was developed on the experimental data in which air was introduced into the liquid through a porous membrane. The Qian's correlation predicts reasonably well.
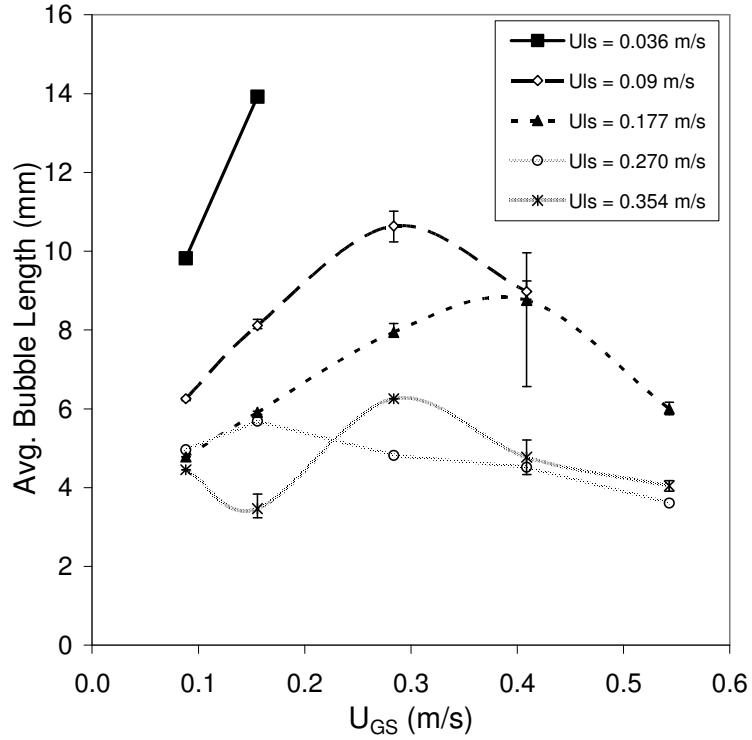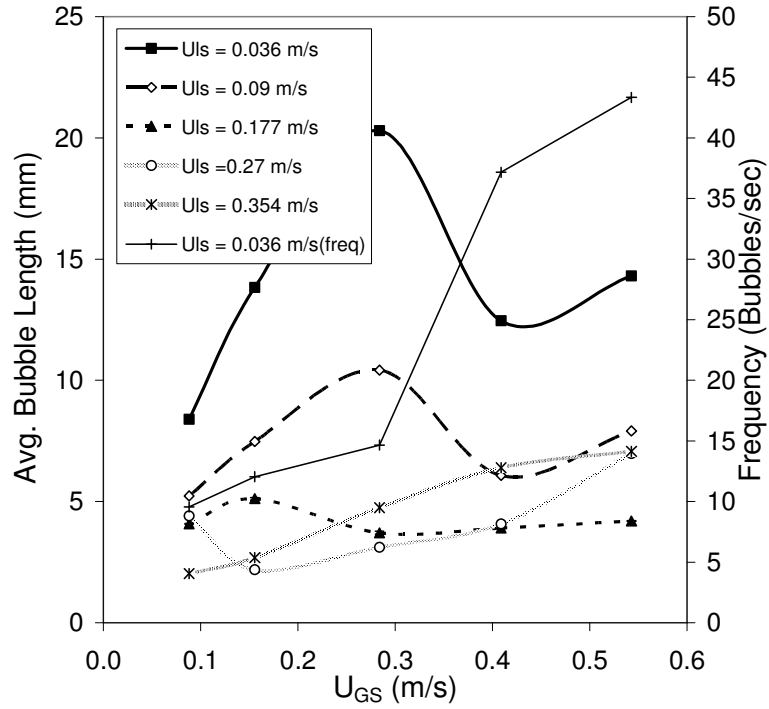
Figure 2.18: Variation of time averaged bubble length with superficial gas velocity (U_{GS}) (a) Water/nitrogen system (b) Water-glycerol / nitrogen system
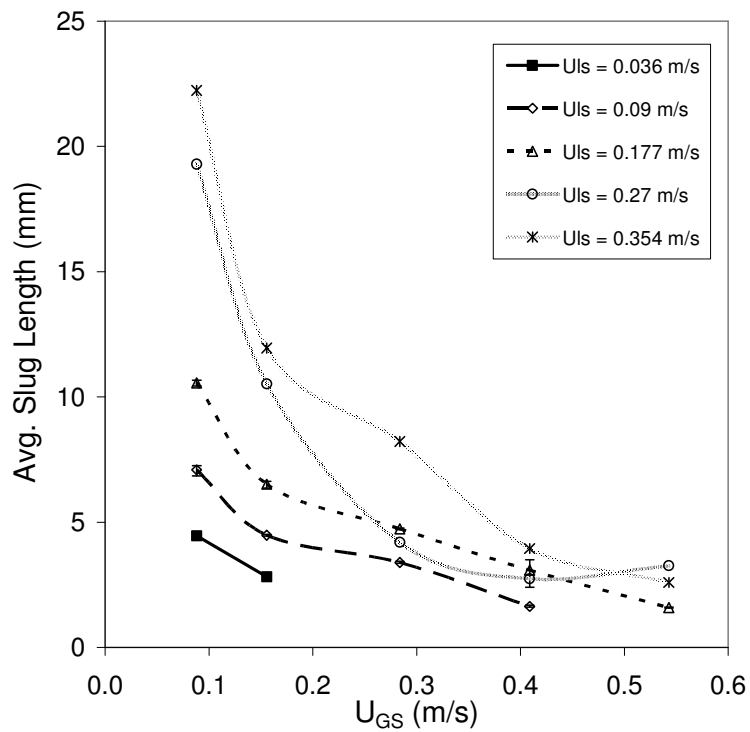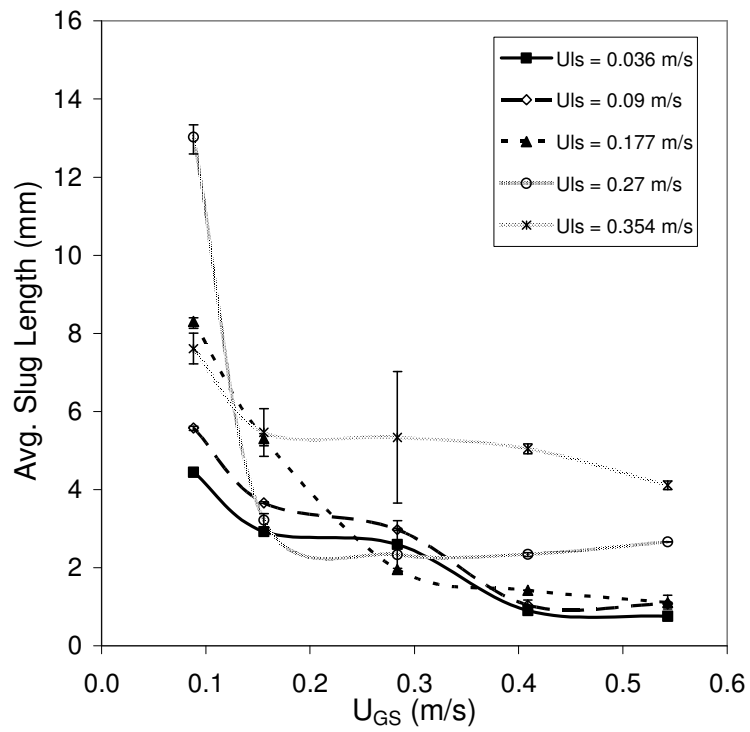
Figure 2.19: Variation of time averaged slug length with superficial gas velocity (U_{GS}) (a) Water/nitrogen system (b) Water-glycerol / nitrogen system
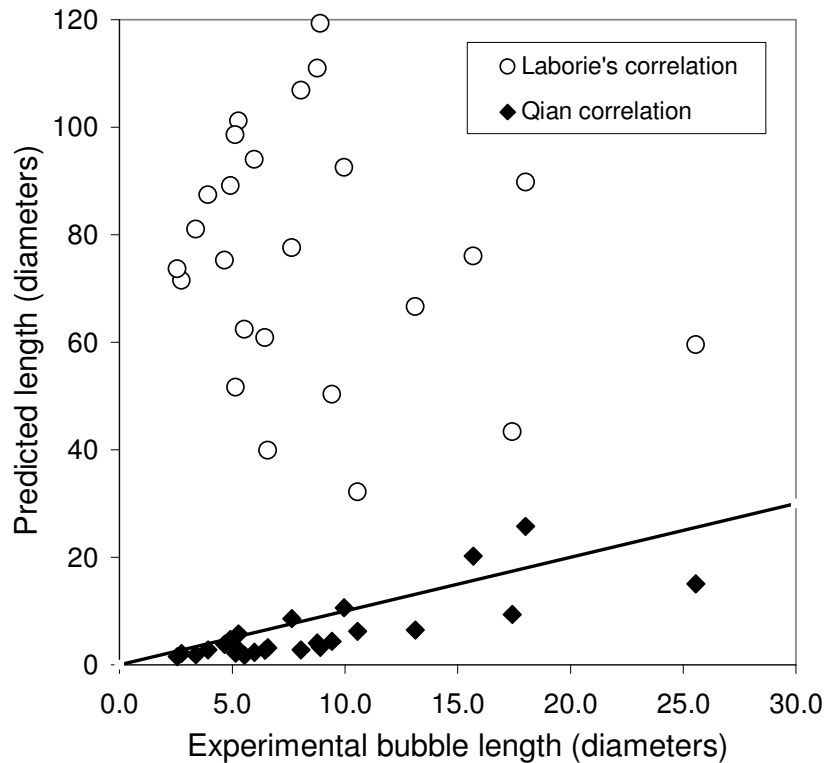
Figure 2.20: Comparison of our experimental data with the correlations of Laborie et al
(1999) and Qian and Lawal (2006)

As mentioned above experiments indicate bubble length increases with increasing U_{GS} and decreasing U_{LS}. So if a plot of dimensionless bubble length (L_B/D) vs. ratio of (U_{GS}/U_{LS}) is constructed a linear relationship of the type $\dfrac{L_B}{D} = a + b\left(\dfrac{U_{GS}}{U_{LS}}\right)$ is observed. This trend however was observed only for P1 regime. (There are difficulties in correlating the bubble length over the entire slug pattern because of the transition from P1 to P2, where the bubble length is underestimated due to the averaging effect.)

This trend is explained using the squeezing-blocking mechanism of slug formation proposed by Garstecki et al (2006) for liquid-liquid flows in a rectangular T-junction channel. At very low Capillary numbers, the interfacial effects dominate over the shear stresses and the bubble-breakup is only based on flow rate of the liquid. This regime of slug formation is called the squeezing regime. Because of the domination of the surface tension force over the viscous force, the gas-liquid interface can expand and block the entire liquid flow. When the tip of the gas front blocks the junction, the flow of the liquid into the main channel is

prevented. Hence, the flow of the liquid tends to squeeze and pinch-off the neck connecting the advancing Taylor bubble and the gas stream in the side inlet channel. Here the pinching action takes places exactly at the end of the inlet junction. More the liquid flow rate, the more vigorous is the squeezing action, and hence lesser the bubble length. The more the gas flow rate, more amount of gas can enter the main channel in the time required for the liquid flow to squeeze and detach the bubble from the source. This justifies agreement with our observed trend.

Yu et al (2007) studies on gas-liquid flows also noted similar observations at lower Capillary numbers (<0.01). However at higher Capillary numbers, he noted the bubbles form through a different mechanism. As the gas-stream enters the main channel the tip of the gas phase keeps expanding and its neck starts thinning and lead to bubble breakup. Here the breakup point is located inside the main channel. This regime is called the shearing regime. In our experiments, the patterns P2, P3 and P4 falls in the shearing regime and the bubble lengths in these patterns could be explained only by a more rigorous study on bubble formation in the shearing regime.

The relationship is further verified for data of Kreutzer et al. (2005) and Qian and Lawal (2006). Figure 2.21 (a) shows the observed trends. Here 'a' and 'b' are constants which are expected to depend upon the inlet configuration of the mixer. However, inlet geometry dependence of the constants needs to be studied and verified. Interestingly such a correlation is also observed for the liquid slug lengths (Figure 2.21 (b)). Table 2.7 summarizes the proposed correlation.
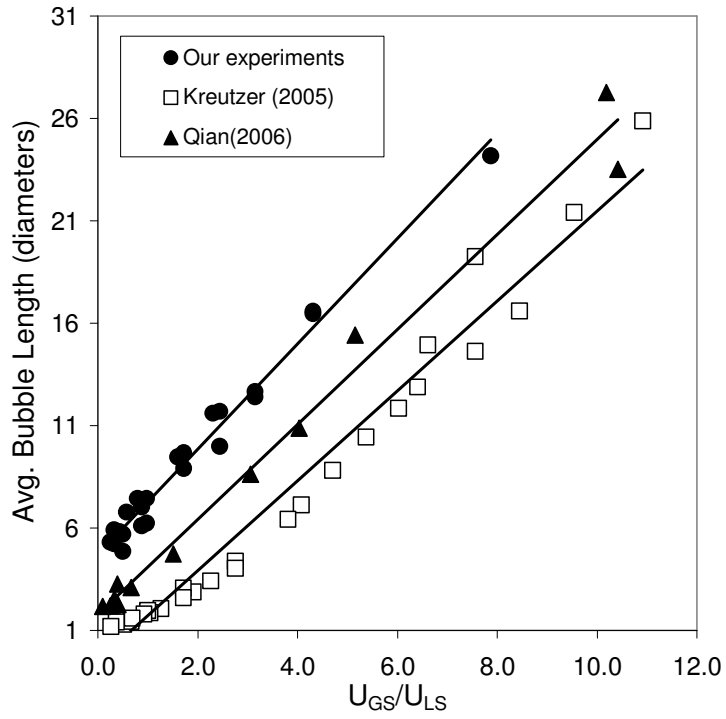
(a)
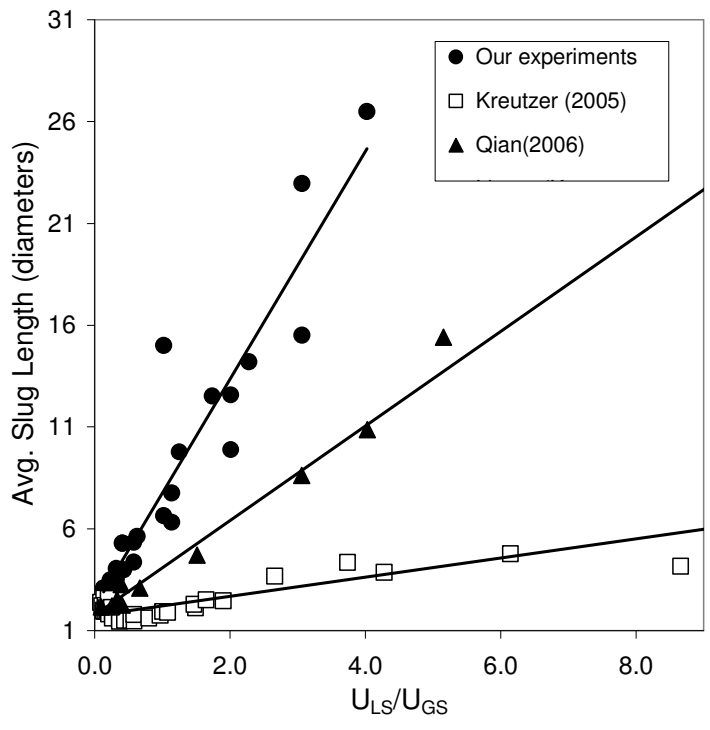
(b)

Figure 2.21: (a) $\dfrac{L_B}{D}$ vs $\dfrac{U_{GS}}{U_{LS}}$ plot (b) $\dfrac{L_s}{D}$ vs $\dfrac{U_{GS}}{U_{LS}}$ plot

Table 2.6(a): Bubble and slug length data for water/nitrogen system

U$_{LS}$(m/s)	U$_{GS}$(m/s)	Bubble length (mm)			Slug length (mm)			Flow pattern
		min	max	avg	min	max	avg	
0.036	0.088	8.127	8.668	8.461	4.082	4.589	4.407	P1
	0.155	13.03	14.04	13.77	2.584	3.076	2.842	P1
	0.283	19.75	20.61	20.19	2.158	2.748	2.513	P1
	0.408	0.981	24.94	12.28	0.244	2.29	0.984	P2
	0.542	0.954	30.74	14.2	0.305	1.432	0.768	P2
	1.28	Annular						P5
0.09	0.088	5.271	5.467	5.393	5.431	5.642	5.513	P1
	0.155	7.314	7.576	7.446	3.636	3.824	3.693	P1
	0.283	0.606	10.7	10.39	0.202	4.269	2.962	P1
	0.408	1.018	11.78	5.508	0.242	2.36	1.076	P2
	0.542	1.36	16.66	7.122	0.342	2.441	0.944	P2
	1.28	Annular						P5
0.177	0.088	3.994	4.144	4.072	7.958	8.303	8.125	P1
	0.155	4.981	5.324	5.149	4.969	5.324	5.122	P1
	0.283	1.462	6.134	3.773	0.971	2.966	1.914	P2
	0.408	1.926	5.889	3.895	0.968	1.954	1.433	P2
	0.542	1.598	6.79	4.2	0.785	1.607	1.103	P2
	1.28	Annular						P5
0.270	0.088	4.085	4.505	4.399	12.92	13.7	13.35	P1
	0.155	0.232	5.106	2.052	0.228	8.179	2.999	P2
	0.283	0.592	6.688	2.526	0.295	6.246	1.847	P2
	0.408	0.358	14.34	4.016	0.373	11.64	2.358	P3
	0.542	0.491	28.11	6.973	0.356	23.12	2.662	P3
	1.28	0.904	38.28	10.87	0.881	5.73	1.796	P4
0.354	0.088	0.455	4.294	1.879	0.23	21.01	7.215	P2
	0.155	0.277	5.306	2.495	0.27	12.95	4.858	P2
	0.283	0.347	9.114	6.407	0.342	9.967	7.025	P3
	0.408	0.409	14.46	6.323	0.362	16.14	4.924	P3
	0.542	0.491	19.42	7.184	0.48	22.91	4.226	P3
	1.28	Not determined						P3

43

Table 2.6(b) Bubble and slug length data for water-glycerol / nitrogen system:

U_{LS}(m/s)	U_{GS}(m/s)	Bubble length (mm)			Slug length (mm)			Flow pattern
		min	max	avg	min	max	avg	
0.036	0.088	9.675	9.872	9.779	4.328	4.471	4.382	P1
	0.155	13.52	14.15	13.84	2.566	3.014	2.814	P1
	0.283	Annular						P5
	0.408	Annular						P5
	0.542	Annular						P5
	1.28	Annular						P5
0.09	0.088	5.038	6.833	6.205	5.65	8.296	6.853	P1
	0.155	7.171	9.192	8.272	3.959	5.362	4.512	P1
	0.283	8.533	14.28	11.02	2.769	3.987	3.359	P1
	0.408	0.246	85.68	8.784	0.28	21.17	1.623	P2
	0.542	Annular						P5
	1.28	Annular						P5
0.177	0.088	4.692	4.91	4.783	10.21	10.7	10.44	P1
	0.155	5.848	6.09	5.94	6.265	6.529	6.355	P1
	0.283	7.294	8.886	8.163	4.255	5.561	4.739	P1
	0.408	0.398	10.56	9.957	0.398	4.02	3.503	P2
	0.542	0.466	12.91	6.167	0.472	3.946	1.613	P2
	1.28	Annular						P5
0.270	0.088	4.729	5.179	4.96	18.64	20.04	19.29	P1
	0.155	5.261	6.047	5.689	9.38	12.05	10.52	P1
	0.283	0.344	8.425	4.136	0.345	15.49	3.606	P2
	0.408	0.455	6.125	4.518	0.45	5.62	2.744	P4
	0.542	0.505	10.28	3.611	0.506	7.507	3.262	P4
	1.28	0.935	26.53	12.18	0.923	5.664	2.026	P1
0.354	0.088	0.279	4.778	4.455	0.558	24.27	22.24	P1
	0.155	0.317	5.526	3.234	0.318	12.68	7.734	P1
	0.283	0.395	6.518	2.948	0.407	9.302	3.723	P2
	0.408	0.479	8.705	5.209	0.482	11.7	4.39	P4
	0.542	0.501	11.43	4.179	0.481	8.956	2.561	P4
	1.28	1.352	39.21	10.66	1.237	6.562	2.407	P1

Table 2.7 Bubble and Slug length correlation.

Data	Bubble length	Slug length
Our experiments	$\dfrac{L_B}{D} = 4.7 + 2.5742\left(\dfrac{U_{GS}}{U_{LS}}\right)$	$\dfrac{L_S}{D} = 2.38 + 4.9\left(\dfrac{U_{LS}}{U_{GS}}\right)$
Qian and Lawal (2006)	$\dfrac{L_B}{D} = 2.32 + 1.78\left(\dfrac{U_{GS}}{U_{LS}}\right)$	$\dfrac{L_S}{D} = 1.77 + 2.32\left(\dfrac{U_{LS}}{U_{GS}}\right)$
Kreutzer et al (2005)	$\dfrac{L_B}{D} = 0.46 + 2.19\left(\dfrac{U_{GS}}{U_{LS}}\right)$	$\dfrac{L_S}{D} = 1.84 + 0.47\left(\dfrac{U_{LS}}{U_{GS}}\right)$

2.4. Conclusions

Gas-liquid flow in a micro channel has been studied using high speed digital imaging. A systematic image analysis algorithm has been developed for the extraction of key hydrodynamic parameters from the captured videos. The extracted features (bubble velocity, bubble and slug lengths, gas holdup and frequency) were compared relevant information from the literature. Following conclusions are drawn from the present study:

- The sub flow patterns of slug flow were classified on the basis of Weber number calculated using two phase velocity U_{TP}. Few similarities with flow patterns in micro-gravity conditions were found.

- The shape of the bubble was found to be a strong function of Capillary number

- The drift model as proposed by Zuber and Findlay (1956) for predicting bubble velocities was found to be relevant. Parameters C_0 and C_1 were found to comparable with those available in the literature for similar studies. Dimensionless bubble velocity (W) was found to be an increasing function of Capillary number.

- Film thickness correlation as proposed by Fairbrother and Stubbs (1935) Aussillous and Quere (2000) were both found to be relevant for the range of Capillary number studied. However, use of Aussillous and Quere (2000) correlation is recommended, as it is valid for the wide range of Capillary number.

- ε_G / α was useful in measuring the deviation from homogeneous flow. The deviation from homogeneous flow increased with increasing Capillary number.

- The non-uniformity in bubble and slug lengths increases with increase in liquid superficial velocity. Correlations were proposed for determining bubble and slug lengths.

$$\frac{L_B}{D} = a_1 + b_1(\frac{U_{GS}}{U_{LS}}) \, ;$$

$$\frac{L_S}{D} = a_2 + b_2(\frac{U_{LS}}{U_{GS}}) \, ;$$

Where 'a' and 'b' are constants expected to be dependent on the geometry of the inlet section. The inlet geometry dependence of the constants needs to be studied and verified (Table 2.7).

Chapter 3

CFD Modeling of Slug Flow

3.1. Introduction

In recent years, many studies have been reported on modeling of gas-liquid flows in capillaries using CFD. For example Heibel et al. (2001) and Roy et al. (2002) developed a full-scale computational fluid dynamics model assuming steady state for a fully developed film flow of liquid with core gas in a single channel. They found good agreement between the model predictions and MRI measurements for overall liquid holdup in channels. However, these studies were limited to the annular flow regime. Kreutzer et al. (2003) modeled slug flow in a circular capillary using 2d-axis symmetric domain. He performed simulations assuming a single phase flow of liquid as gas has very less density and viscosity compared to the liquid with which it is in contact. The simulated results for pressure drop were found to be in good agreement with experimentally measured pressure drop. In another similar study van Baten and Krishna (2004) modeled steady-state slug flow inside the circular capillary by using a unit cell approach. The simulations were performed keeping the bubble stationary and moving the system with its average rise velocity. In the same study they developed a model to determine mass transfer coefficient, k_La for slug flow in capillaries. They compared the predicted results with the k_La predicted using fundamental models (Higbie penetration model and unsteady state diffusion model of Pigford for hemispherical cap and the downward flowing liquid film respectively) and found a good agreement. However these studies were confined to rise of a Taylor bubble in a stationary fluid.

Kashid et al. (2005) used computational fluid dynamics (CFD) simulations based on a unit cell approach to predict the internal circulation within the liquid slugs. The internal circulations were visualized using a CFD particle-tracing algorithm. The internal circulations were qualitatively and quantitatively characterized with the help of the PIV measurements and particle tracing algorithm. They discussed the effect of flow velocity and slug length on the velocity profile and stagnant zones of the internal circulations for a slug with and without a wall film.

In more recent studies, multiphase Volume of Fluid (VOF) approach for simulating Taylor flow in capillaries is being developed. This approach doesn't require assumption of the shape of the bubble as the movement of the gas-liquid interface is tracked based on the distribution of gas volume fraction in a computational cell. Taha and Cui (2004, 2006) used VOF

approach to simulate slug flow in capillaries. However, since these models are computationally intensive, again a unit cell approach having a single unit of bubble and a slug was considered as computational domain. They found good agreement with reported experimental data of Thulasidas et al (1995). In another similar study by Liu and Wang (2008) performed multiphase VOF simulations for non-circular capillaries. They studied bubble shape and size, film thickness velocity flow field and two relative velocities as function of Capillary number and concluded that the flow in sides and corners of a polygonal capillary is different from circular capillaries. However, these studies also require dimensions of unit cell and gas hold-up etc. which need to be determined experimentally.

In most of the work done so far, a prior knowledge of characteristics of slug flow such as length of unit cell, length of bubble/slug (or gas holdup), and bubble velocity is a must. Most of the simulations assumed a fully developed flow profile at the inlet which also needs experimental validation. In the present study a computational fluid dynamic (CFD) model is developed using a unit cell approach to simulate liquid flow field around the bubble in a square capillary. The simulated results are compared with the experimental PIV observations obtained from the research group of University of Birmingham. Furthermore the developed model is extended to predict gas-liquid mass transfer coefficient using a similar approach developed by van Baten and Krishna (2004), to qualitatively and quantitatively understand the influence of the flow field upon mass transfer characteristics within Taylor flow.

3.2. Flow model

3.2.1. Model equations

As mentioned above each slug is modeled as a distinct single-phase domain. The bubble is considered as 'void' acting as a free surface with the surrounding liquid phase. The conservation equations for mass and momentum are given below

$$\nabla.U = 0 \qquad\qquad\qquad \textbf{3.1}$$

$$\frac{\partial U}{\partial t} + \nabla.(U\,U) = -\frac{1}{\rho}\left[\nabla P + \mu\nabla^2 U\right] + g \qquad\qquad \textbf{3.2}$$

Where ρ, U and μ. represent, respectively the macroscopic density, velocity and viscosity of the liquid phase, P is the pressure and g is the gravitational acceleration. Based on magnitudes of Reynolds numbers considered in this work, laminar flow condition was assumed to prevail in the system. The dimensions of the unit cell were obtained from the experiments conducted for co-current downflow of gas and liquid in square capillaries (Tsoligkas et al., 2007).

The species mass balance equation used for determination of mass transfer is as given below

$$\frac{\partial}{\partial t}(\rho_L C_L) \;+\; \nabla\cdot\left(\rho_L U_L C_L \;-\; D\rho_L \nabla C_L\right) \;=\; 0 \qquad\qquad \textbf{3.3}$$

Here, C_L is the concentration of mass-tracer in the liquid (a.u.) and D is the diffusion coefficient of mass tracer in the liquid.

3.2.2. Computational domain

An idealized geometry for a slug flow simulations consist of a Taylor bubble suspended at the centre of two periodic boundaries Figure 3.1 (Unit cell approach). Typically these Taylor bubbles consist of two hemispherical caps at the top and bottom attached to cylindrical/square body. The gas holdup, ε_G and unit cell length, L_{UC} are determined by analyzing the high speed movies recorded during the experiments. By analyzing each movie an average bubble velocity, U_B is determined. For each superficial gas velocity, U_{GS} the gas holdup is calculated as

$$\varepsilon_G = \frac{U_{GS}}{U_B} \qquad\qquad \textbf{3.4}$$

Assuming that all unit cell lengths are of equal lengths, summation of bubble length (L_{Bubble}) and slug length (L_{Slug}) measured from the photograph gives the length of unit cell (L_{UC}).

$$L_{UC} = L_{Bubble} + L_{Slug}$$ **3.5**

Volume of the bubble is then calculated as

$$V_{Bubble} = \varepsilon_G * V_{UC} = \varepsilon_G * d_c^2 * L_{UC}$$ **3.6**
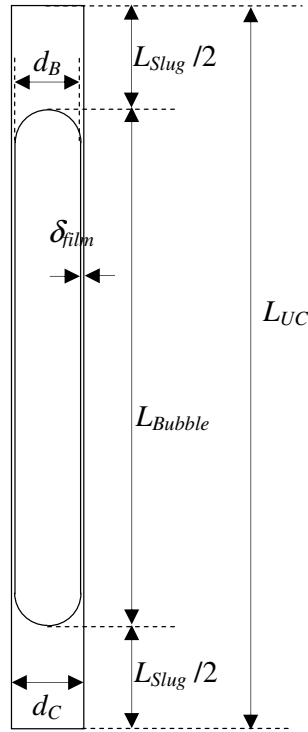
Figure 3.1: Typical representation of a Unit Cell

Once the above parameters are fixed, the shape of the bubble is determined. Ideally a slug bubble should have a cylindrical body attached to a hemispherical cap. However, for low Capillary number (*Ca*< 0.1) the effect of shape of the channel is pronounced and the bubble tends to become non axis symmetric (Thulsidas et al. 1995). This results from the corners being affected by viscous forces to a greater extent than regions near the walls. These bubbles have spherical ends and tend to flatten out against the walls. Hence, the shape of the bubble can typically lie between a perfect cylindrical body with hemispherical caps and a full

parallelepiped body. Assuming an intermediate shape, following methodology was used to determine the shape of the considered bubble. Volume of the bubble is given by

$$V_{Bubble} = \left(a \, d_B^{\,2} \left(L_{Bubble} - d_B \right) + b \frac{\pi}{6} d_B^{\,3} \right)$$ **3.7**

where 'a' accounts for body (cylindrical/parallelepiped) and 'b' accounts for the caps (refer Table 3.1 and Figure 3.2). Bubble shape depends upon the factor 'a' ($\pi/4 < a < 1$). Assuming an intermediate value of 0.9 for rounded corners and 1.1 for cap attached to rounded square base, diameter of the bubble, d_B and hence the film thickness 'δ' is calculated. The radius of curvature at the corners is then calculated using the formula below

$$0.9 \, d_B^{\,2} = k^2 + 4kr + \pi \, r_{Curv}^{\,2}$$ **3.8**

Table 3.1: Parameters for calculation of bubble volume in Eqn. 3.6

Body	Cap	a	b
Cylindrical	Hemispherical	$\pi/4$	1
Parallelepiped	Cap attached to square base	1	≈ 1.1
Parallelepiped with rounded corners	Cap attached to rounded square base	0.9	≈ 1.1

(i) a = $\pi/4$, b = 1   (ii) a = 1, b ≈1.1   (iii) a = 0.9, b ≈1.1
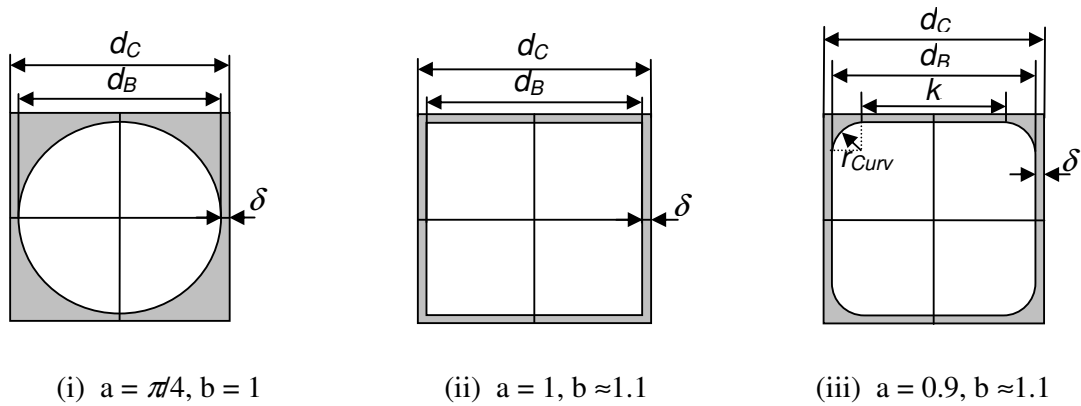
Figure 3.2: Pictorial representation of parameters used to define the shape of bubble

Since for simulation purpose the bubble volume is excluded and only the bubble boundary is considered, the shape of the bubble is subtracted from the unit cell volume to obtain liquid flow domain with bubble 'void'. Also as the domain is symmetric about the central axis in x-y direction, only quarter part of the total domain is simulated to reduce the computational requirement. The grid is made up of hexahedral control volumes. The control volumes are smaller in the vicinity of the wall in order to improve resolution of the flow within the liquid film region. The total grid size varied for all the cases depending upon the unit cell dimensions (i.e L_{UC}, L_{film}, δ and the shape of the bubble: bullet shape/hemispherical). Figure 3.3 gives the details of computational domain and grid generated for the case of U_{GS} = 0.2086m/s and U_{LS} = 0.0926m/s.
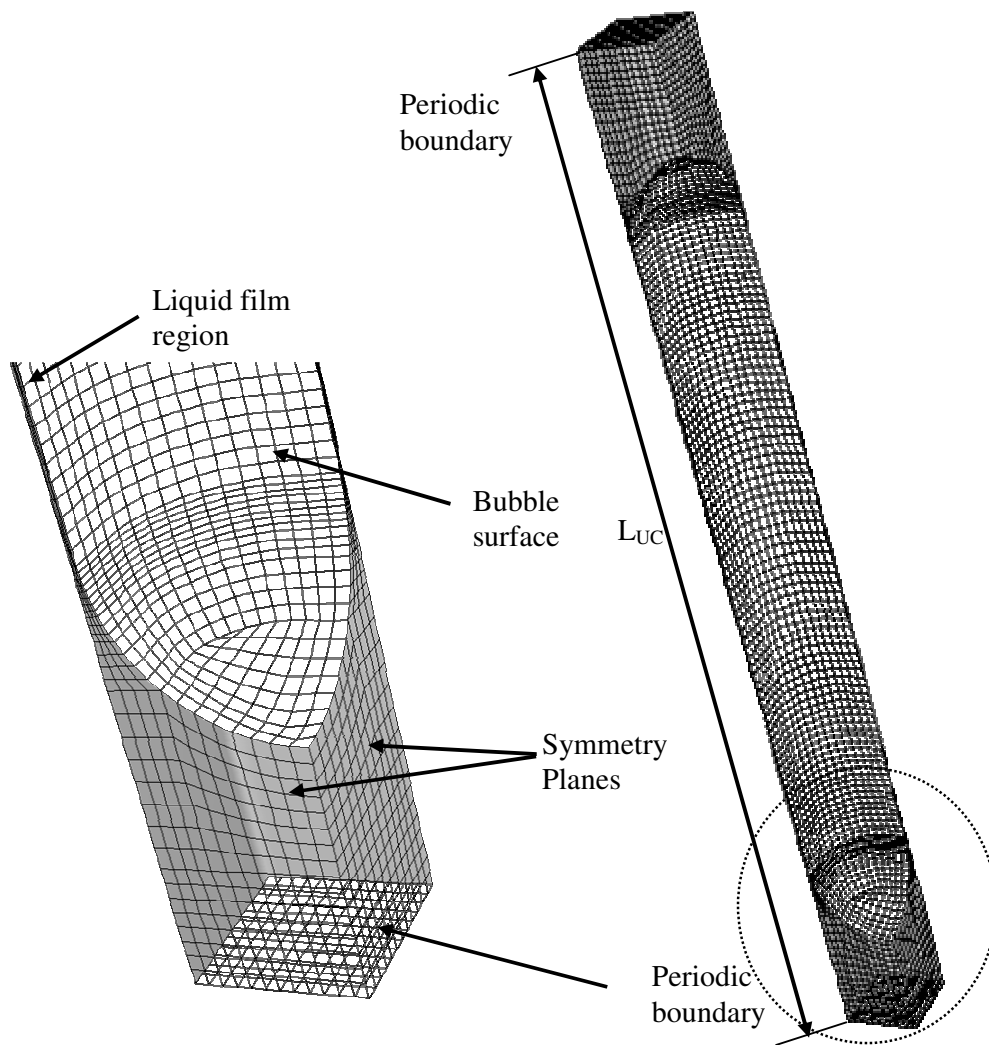
Figure 3.3: Computational domain and grid for the case of U_{GS} = 0.2086m/s and U_{LS} = 0.0926m/s.

3.2.3.   Boundary conditions

All the simulations were carried out in a reference frame in which bubble is stationary and the system moves up with the bubble rise velocity U_B. The boundary condition is periodic in the vertical direction ($U_{top} = U_{bottom}$). At the outer wall, the boundary conditions were set as $U_z = U_{wall} = -U_B$. The bubble surrounding the surface is specified as free slip (zero shear wall). At the symmetry planes we have $dU_z/dx = 0$.

For periodic boundaries one should either specify the net pressure drop or mass flow rate across the periodic domain. The two phase pressure across the unit cell was not known, hence mass flow rate across the periodic domain was calculated which is given below.

Since, for the simulation purpose it is assumed that the gas bubble is stationary and reference frame is moved at velocity U_B in the opposite direction to that of the bubble, a correction in the liquid flow rate because of the wall movement is to be accounted while calculating the net liquid mass flow rate across the periodic domain. This is given by

$$Net \;\; Mass \;\; flow \;\; rate \;\; = \;\; -\dot{m}_{Downward} \;\; + \;\; \dot{m}_{Upward}$$

$$\begin{pmatrix} actual \;\; downward \\ liquid \;\; flow \end{pmatrix} \qquad \begin{pmatrix} upward \;\; flow \;\; because \\ of \;\; wall \;\; movement \end{pmatrix}$$

3.9

$$\left. \begin{aligned} \dot{m}_{Downward} &= U_{LS} \, A \, \rho_L \\ \dot{m}_{Upwnward} &= U_{Wall} \, \varepsilon_L \, A \, \rho_L \\ Net \; \dot{m} &= U_{Wall} \, \varepsilon_L \, A \, \rho_L - U_{LS} \, A \, \rho_L \end{aligned} \right\} \qquad U_{Wall} = -U_B \qquad \textbf{3.10}$$

Figure 3.4 shows the schematic picture of the simulated domain with boundary conditions.

For the determination of mass transfer coefficient, the periodic domain was splitted and rezoned as inlet and outlet with zero concentration of tracer at the inlet. At the bubble surface, the concentration of the tracer was specified as $C_{L\,s} = 1$. Zero tracer flux was allowed at the outer wall. Symmetry conditions apply to the center axis.
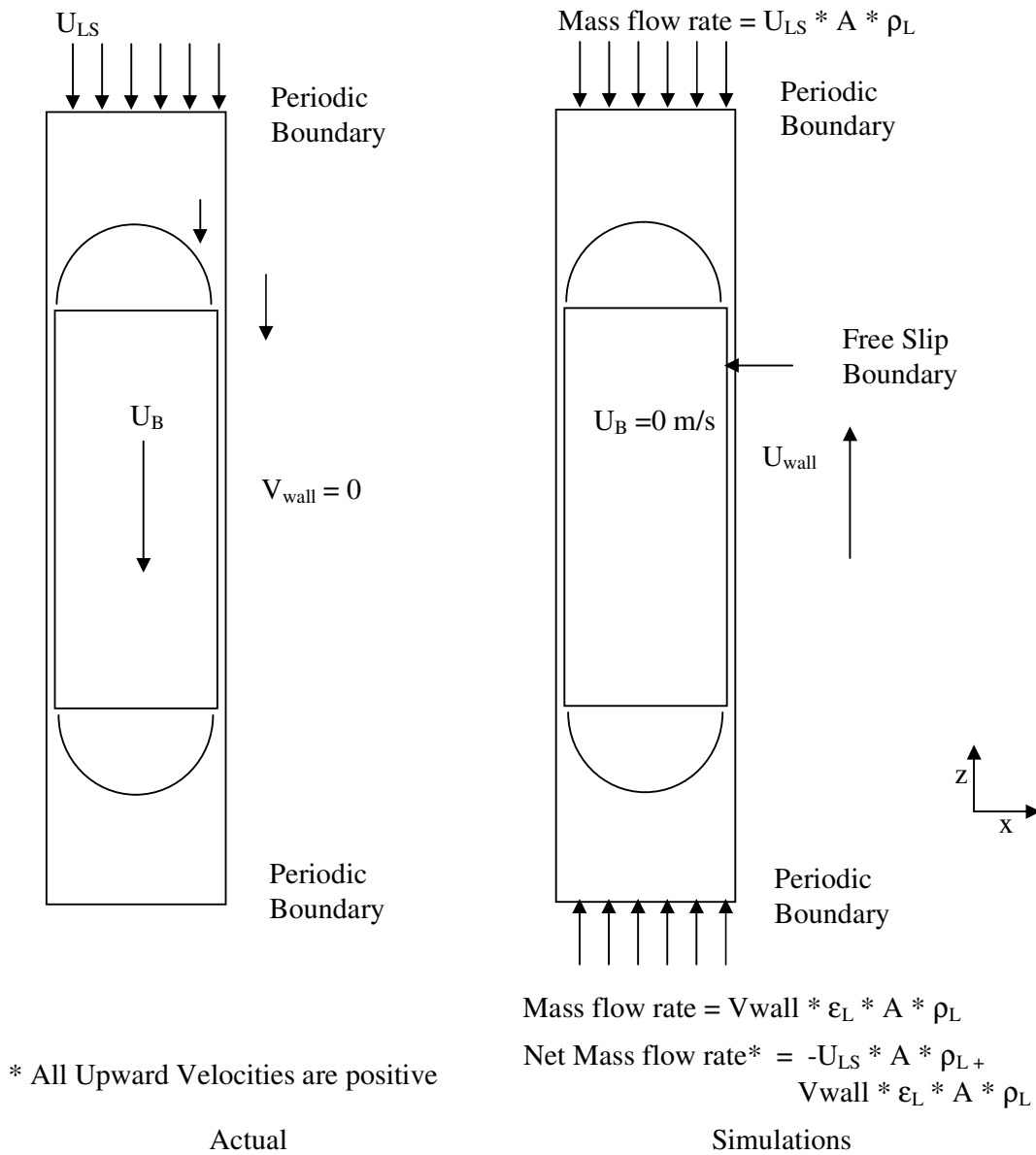
Figure 3.4: Schematic overview of the computational domain with boundary conditions

3.2.4. Numerical solution

The model equations were solved using commercial CFD software, FLUENT version 6.3.26 (of Fluent. Inc USA). Geometry of computational domain was modelled using Gambit 2.0 (Fluent Inc., USA). Appropriate grid was generated for each of the simulated case. The convective terms in eqs. (1) and (2) are discritised using SECOND ORDER UPWIND

differencing scheme. The pressure–velocity coupling was obtained using the SIMPLE algorithm. The steady state solutions were typically obtained within 10,000 iterations. Convergence was verified by checking mass balance conservation across the domain.

The local liquid velocities in the reference velocity frame with a stationary wall are obtained by subtracting the bubble velocity from the simulated velocities.

$$U_{i\_actual} = U_i - U_B \qquad\qquad\qquad \textbf{3.11}$$

The converged velocity field obtained was used in a subsequent mass transfer simulation campaign, carried out in a transient manner, for which 3000 time steps of 0:001 s were used. The tracer concentration throughout the system was initially set to zero. At t = 0.

The total concentration of tracer in the system at each time step was determined from

$$C_{L,system} = \frac{\sum_{domain} vol_i\, C_{L,i}}{\sum_{domain} vol_i} \qquad\qquad\qquad \textbf{3.12}$$

where the summation is carried out over all the volume elements in the computational domain. The difference in the $C_{L,system}$ values at two consecutive time steps is used to determine the mass flux of tracer from the bubble to the domain (liquid). The volumetric mass transfer coefficient $k_L a$ is then calculated from

$$V\left(\frac{\Delta C_{L,system}}{\Delta t}\right) = k_L a \left(C_{surface} - C_{out}\right)V - Q_{out}C_{out} \qquad\qquad \textbf{3.13}$$

Where V is the volume of the unit cell $C_{L,system} = \dfrac{\sum_{domain} vol_i\, C_{L,i}}{\sum_{domain} vol_i}$, Q_{out} is the volumetric flow rate that is going out of the domain and C_{out} is the average concentration of the tracer at the outlet.

3.3. Results and discussion

Simulations were performed for the experimental data of Tsoligkas et al. (2007) on downward gas-liquid slug flow in a 1.5mm square capillary. Three cases as mentioned in Table 3.2 were considered for simulations. The Capillary number for these simulations ranged from 0.18 -0.32. The predicted results on liquid velocity flow field at periodic boundaries were compared with experimentally measured PIV data. Later using the converged flow field, unsteady simulations were performed to predict volumetric mass transfer coefficient.

Table 3.2: Experimental data of Tsoligkas et al. (2007) considered for simulation (system: Air + 30% water-70% Isopropanol (mixture))

Sr. No	Capillary Number (Ca)	U_{LS} (m/s)	U_{GS} (m/s)	U_B (m/s)	Bubble length (mm)	Slug length (mm)	$L_{UC} = L_{Bubble} + L_{Slug}$ (mm)
Case 1	0.0187	0.0673	0.1407	0.2241	8.2	2.19	10.39
Case 2	0.0299	0.0926	0.2086	0.35714	9.375	2.21	11.585
Case 3	0.0318	0.1064	0.2086	0.38	9.321	2.232	11.553

3.3.1. Liquid velocity profiles

The liquid phase velocity profiles (in the reference frame with the stationary wall) are compared with the experimental PIV data Figure 3.5 shows the simulated velocity profiles for case1 at different axial locations and its comparison with experimental data. As observed the flow gets almost fully developed after the distance of one-fourth the length of the liquid slug and assumes a parabolic profile with maximum at the centre of the channel that is 2.1 times the mean fluid velocity ($U_{TP} = U_{LS} + U_{GS}$). The observed trends showed qualitative comparison with experimental data. However quantitatively simulated results showed over prediction. The typical simulated liquid velocity contours in a stationary frame are shown in Figure 3.6 (a). Figure 3.6 (b) shows the typical velocity vectors in a moving reference frame.
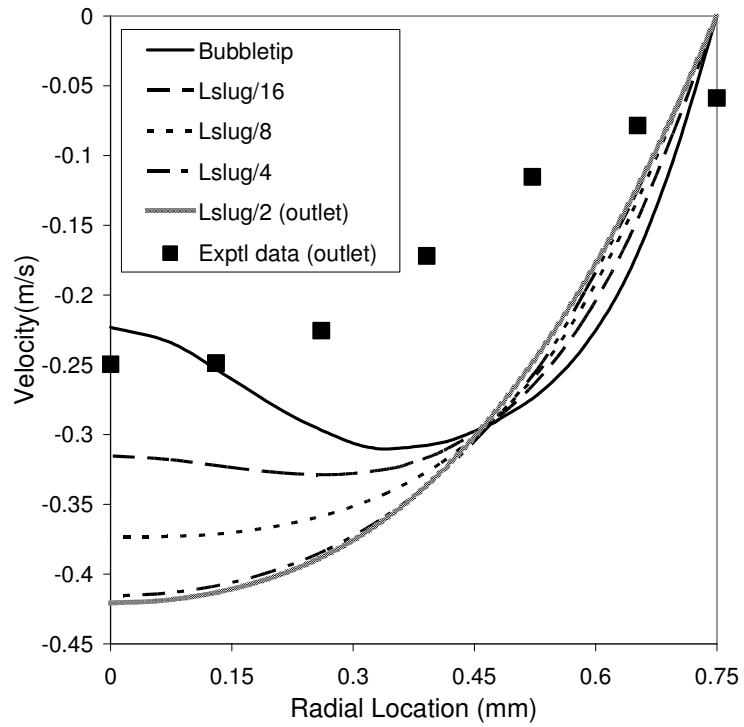
Figure 3.5 : Velocity profiles at different axial locations between bubble tip and periodic boundaries (Case 1)
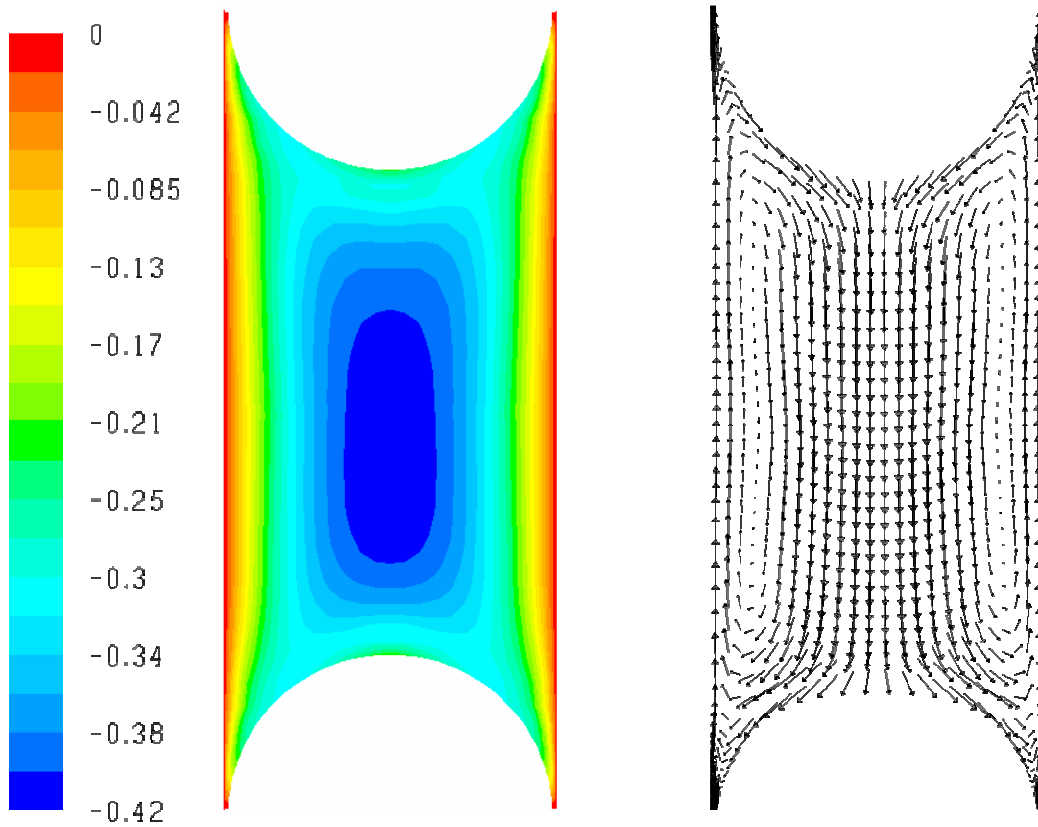
Figure3.6: (a) Axial velocity contours and (b) Velocity vector plot along the vertical centre plane between two successive bubbles: case(1). (for velocity vector plot the frame of reference is with the moving wall

Qualitative comparisons of the simulated results with experimental data for all the three cases are shown in Figures 3.7 – 3.9. These figures show comparison of velocities at the top of the periodic domain and along the vertical central line between two successive bubbles i.e. within the liquid slug). For all the cases the velocities are normalized with respective maximum velocity of the liquid at the centre of the channel on the periodic boundary plane. As observed a reasonably good comparison is observed for all the cases.
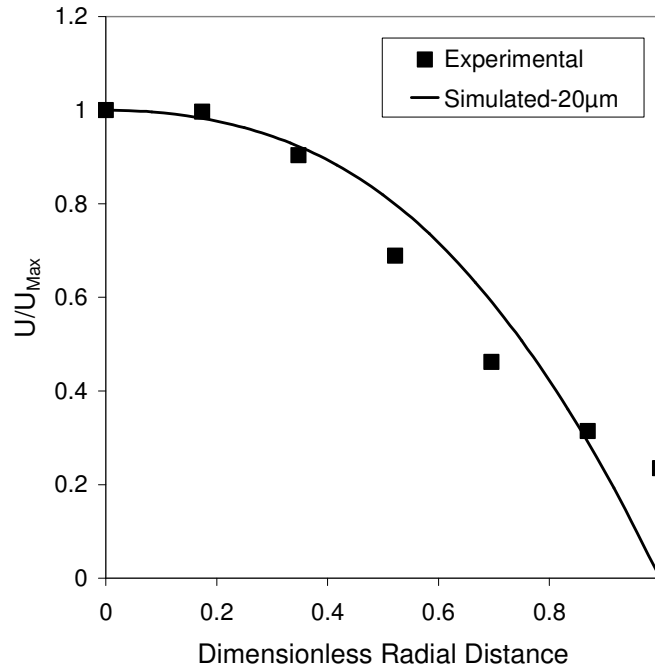
Figure 3.7(a): Normalized Velocity Profile along the horizontal centre plane at the periodic boundaries (Case 1) (normalization done with the maximum velocity U_{max})
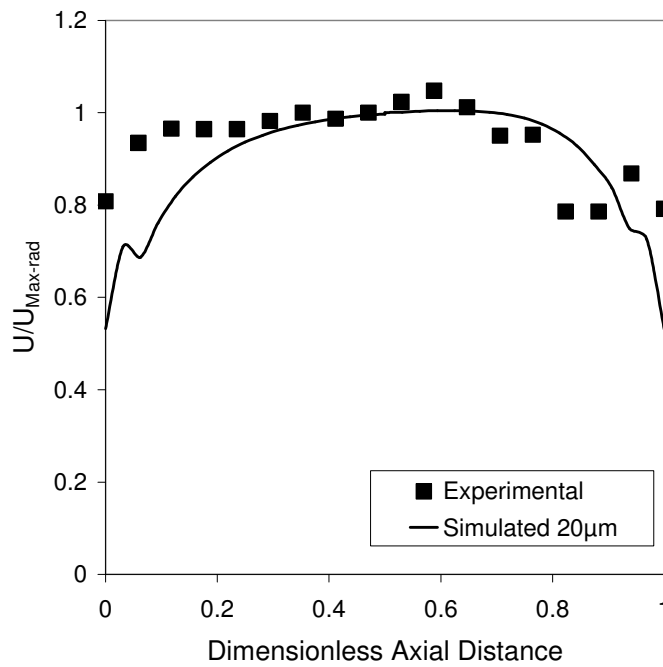
Figure 3.7(b): Normalized Velocity Profile along the vertical centre plane between two successive bubbles (Case 1) (normalization done with the maximum velocity U_{max} at the centre of the axis)
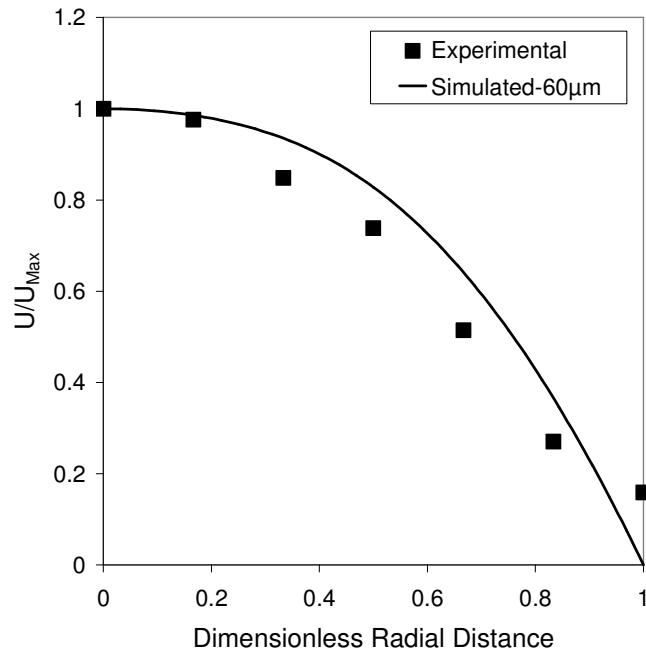
Figure 3.8(a): Normalized Velocity Profile along the horizontal centre plane at the periodic boundaries (Case 2) (normalization done with the maximum velocity U_{max})
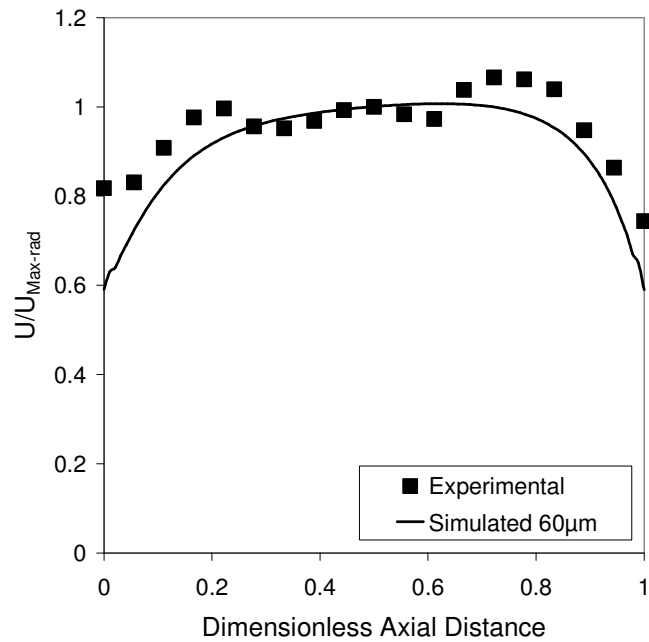
Figure 3.8(b): Normalized Velocity Profile along the vertical centre plane between two successive bubbles (Case 2) (normalization done with the maximum velocity U_{max} at the centre of the axis)
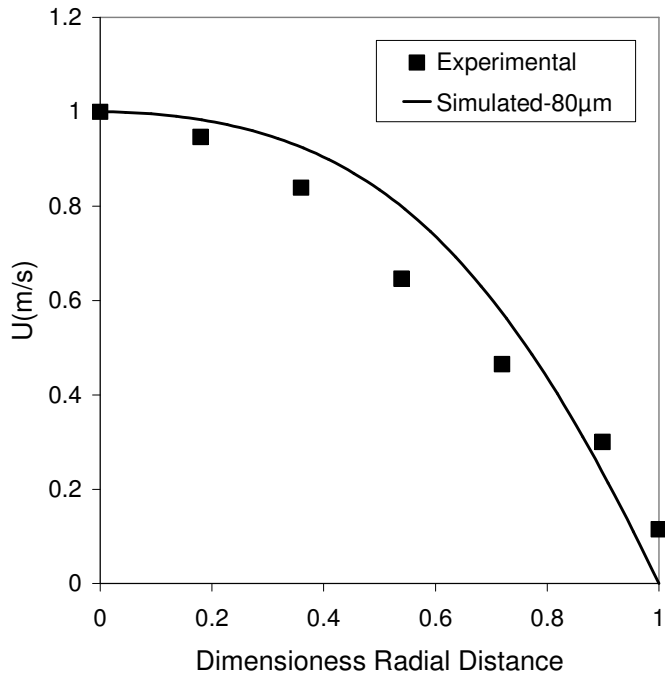
Figure 3.9(a) : Normalized Velocity Profile along the horizontal centre plane at the periodic boundaries (Case 3) (normalization done with the maximum velocity U_{max})
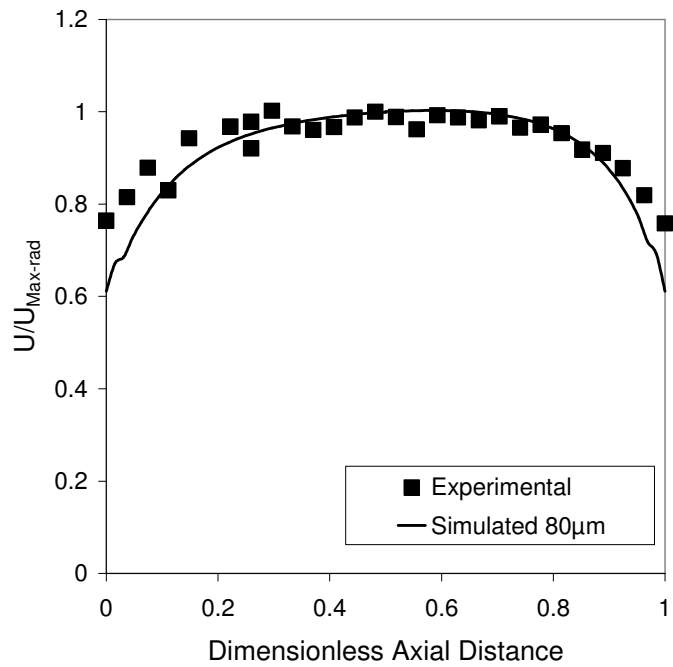
Figure 3.9(b): Normalized Velocity Profile along the vertical centre plane between two successive bubbles (Case 3) (normalization done with the maximum velocity U_{max} at the centre of the axis)

61

3.3.2. Sensitivity with experimental data

To check for the inconsistency in the quantitative over predictions of the simulated results, parametric sensitivity studies were carried out. The different parameters which were provided as an input from the experimental data are U_{LS}, U_{GS}, U_B, L_{Bubble}, L_{slug}, ρ_{Liquid}, μ_{Liquid} and σ. Dependent parameters such as Holdup (ε_L) and film thickness (δ) are calculated as mentioned in the previous section. The physical properties of the fluid are always fixed and the parameters L_{Bubble} and L_{slug} are taken from the snapshot images, and hence their variation is not considered in sensitivity studies.

Simulations were performed for the possible errors in the measurement of superficial gas and liquid velocities U_{LS} and U_{GS} and the bubble velocity U_B. The case1 is considered as a base case for the above simulations. Figure 3.10 and Figure 3.11 shows sensitivity analysis of variation in the measurement of U_{LS} and U_{GS}. Since the contribution of U_{LS} in the mean velocity is only ~30%, theoretically a change of 15% should only account for ~4.5% change in the simulated flow field. Same is also observed in the simulations. Only ~5% change in the U_{Max} is observed, which again is far away from the observed experimental results. Similarly as the contribution of U_{GS} is ~70%, observed changes should be around 10% for 15% variation, which was also observed in the simulations. Table 3.3 gives the summary of these results.

Table 3.3: Summary of parametric sensitivity studies

% Error in the measurement	Contribution to the Mean Velocity (U_{TP})	Expected Change (%)	Simulated	
			U_{Max}	% change Simulated
Basecase	--		-0.42072	
- 5% (U_{LS})	32%	1.6%	-0.41351	1.7%
- 15% (U_{LS})	32%	4.8%	-0.40158	4.54%
- 5% (U_{GS})	68%	3.4%	-0.40645	3.39%
- 10% (U_{GS})	68%	6.8%	-0.39297	6.6%
- 15% (U_{GS})	68%	10.2%	-0.37833	10.07%
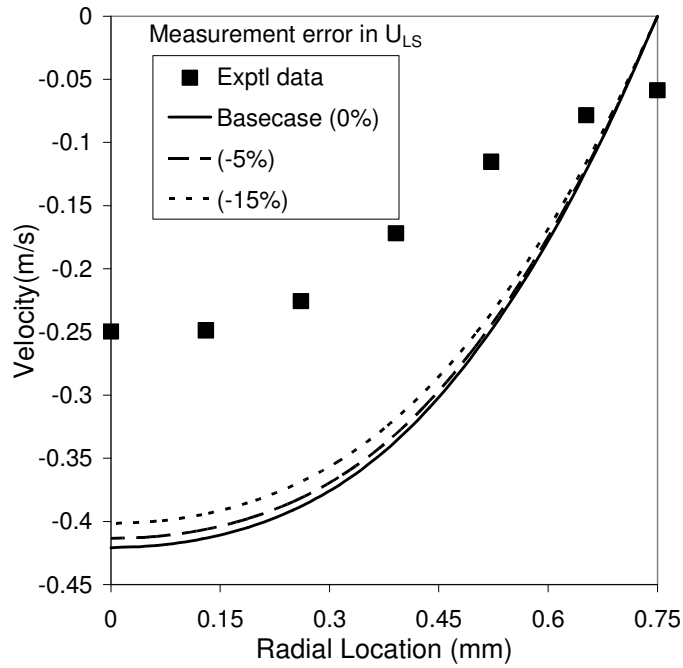
Figure 3.10(a): Effect of possible error in the measurement of superficial liquid velocities on velocity profile at periodic boundaries (Case 1)
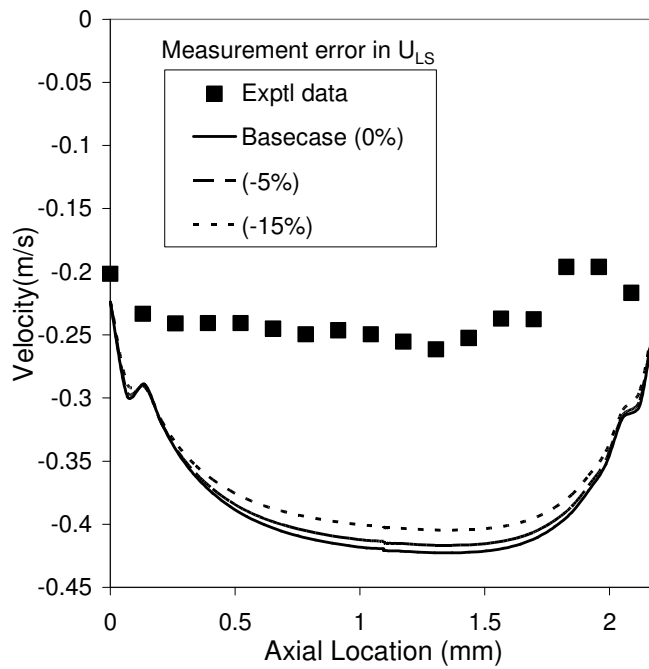
Figure 3.10(b): Effect of possible error in the measurement of superficial liquid velocity on velocity profile within the liquid slug (Case 1)
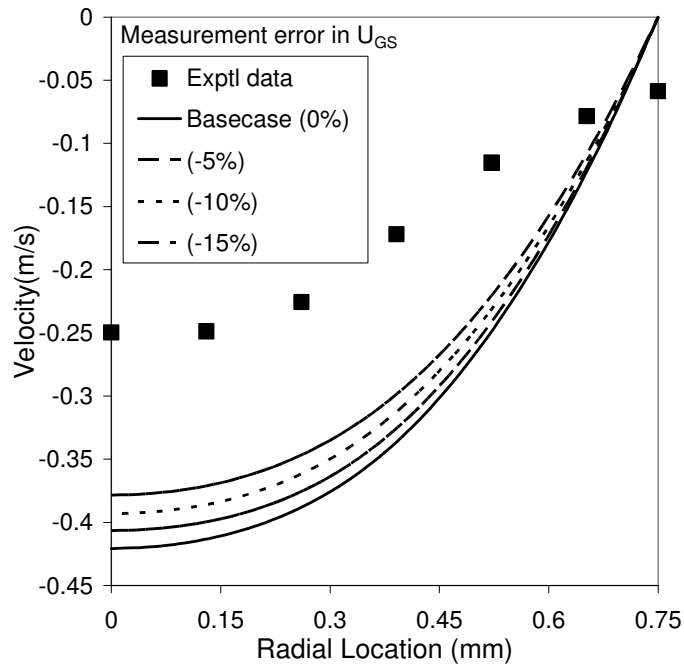
Figure3.11(a): Effect of possible error in the measurement of superficial gas velocity on velocity profile at periodic boundaries (Case 1)
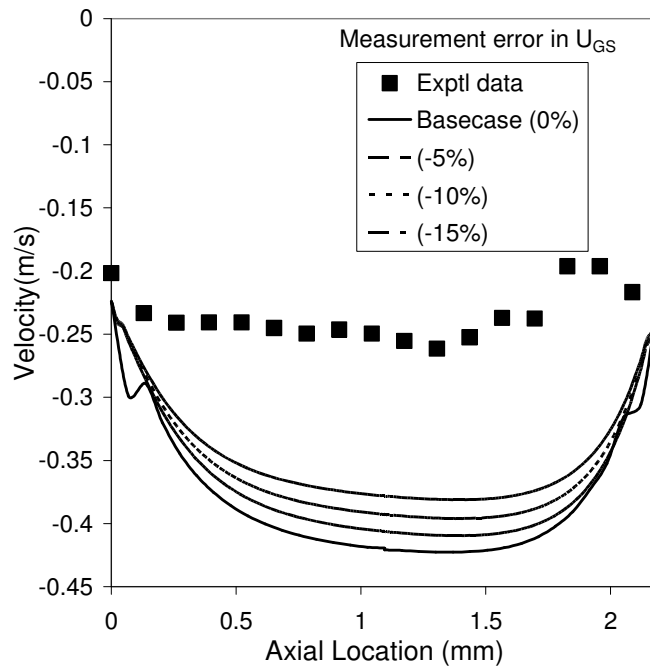
Figure 3.11(b) : Effect of possible error in the measurement of superficial gas velocity on velocity profile within the liquid slug (Case 1)

Figure 3.12 show the simulated results for the sensitivity studies on possible error in the measurement of bubble velocity U_B. Keeping the U_{GS} constant and varying only U_B shall affect only the holdup of the system, which in turn shall affect the film thickness. However as mentioned earlier the flow gets fully developed at a distance not more then $L_{slug}/4$. The effect on velocity profiles at the periodic planes should be negligible. Also since U_{GS} remains constant, the mean velocity U_{TP} remains constant and if the flow is fully developed then the contribution of possible measurement error in U_B on predicted velocity profiles should be negligible. The same is observed from the predicted results. There is hardly any change in the simulated U_{Max} at the periodic planes.

This sensitivity studies indicate either a possibility of systematic error in the reported PIV data. It can be mentioned that calculated mean volumetric flow rate from the experimental data is lower than the reported flow rates. Since the predicted results have shown good agreement with the data after normalization with maximum velocity, the model was further used to examine mass transfer in slug flows.
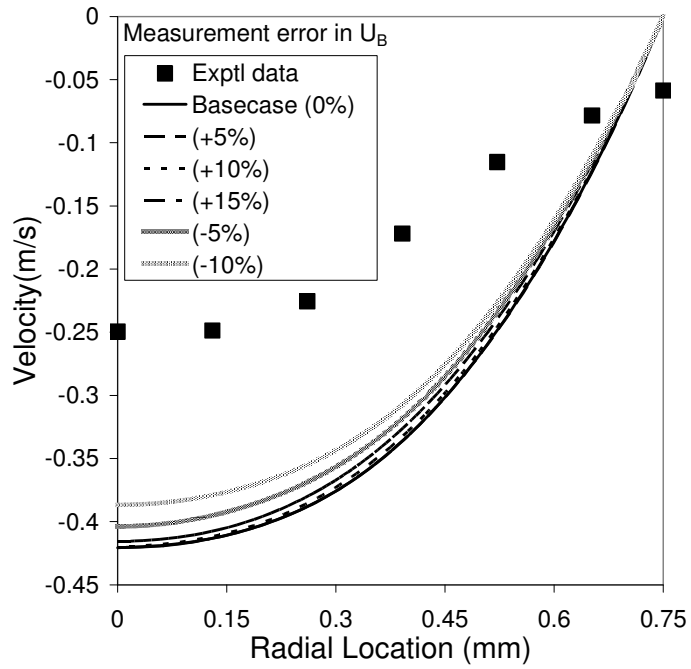
Figure 3.12(a): Effect of possible error in the measurement of bubble velocity on velocity profile at periodic boundaries (Case 1)
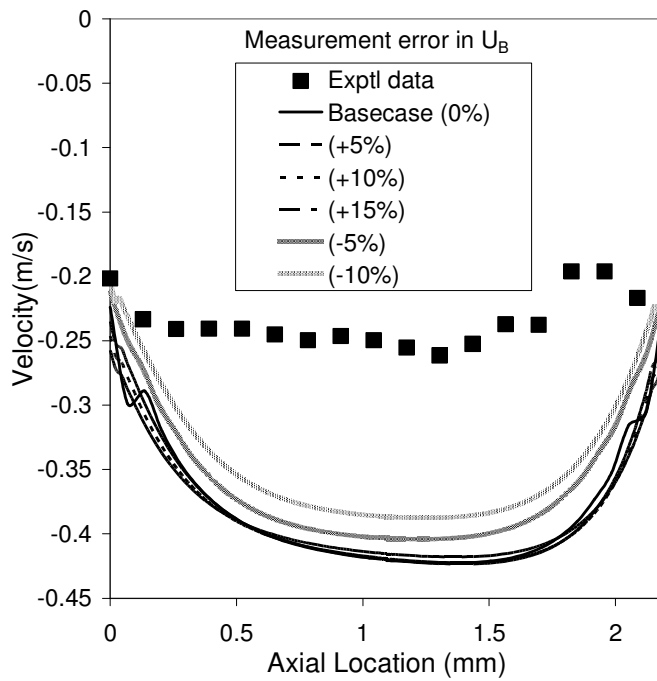
Figure 3.12(b): Effect of possible error in the measurement of bubble velocity on velocity profile within the liquid slug (Case 1)

3.3.3. Mass transfer coefficient

The converged velocity field obtained from the above steady state simulation was used for subsequent mass transfer simulations carried out in a transient manner. However, to correctly capture the steep concentration gradients near the bubble surface and in the film between the bubble and wall a very fine grid is required. Hence, a very fine grid for case-2 was created and again steady-state velocity field was obtained using the interpolated data of coarse grid. This was then used for determination of mass transfer coefficient (k_La). k_La calculated using Eqn. 3.13 is shown in Figure 3.13. We note that the k_La reaches a quasi steady state value after about 1 s and this is the value of the k_La reported in this study (0.0125 sec^{-1}). The calculated k_La value was compared with the correlation of Bercic and Pintar (2003). The correlation prediction was in the range of 10% from the simulated value.
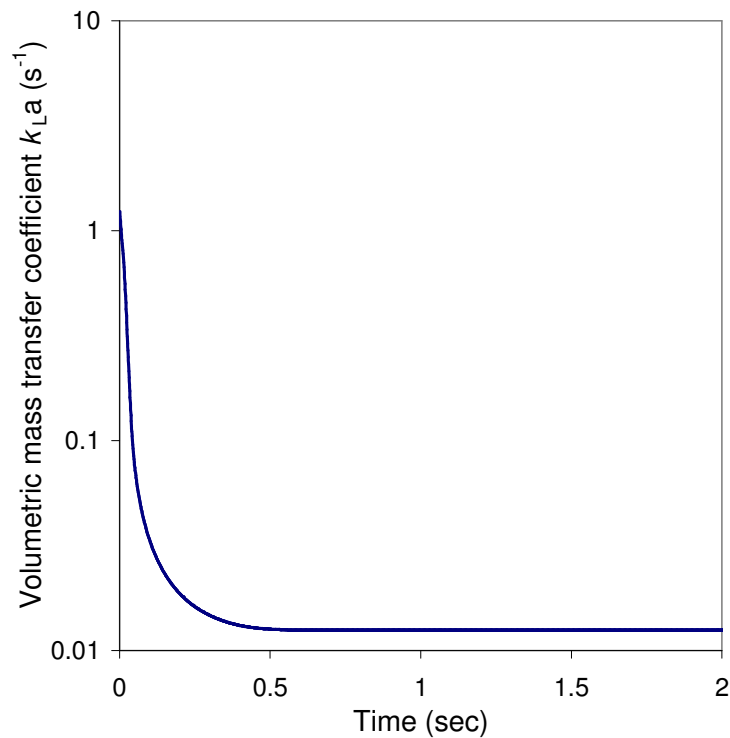
Figure 3.13: Values of k_La from transient mass transfer simulation campaign

3.4. Conclusions

- Model for simulating gas-liquid slug flow in capillaries was developed.
- For the fully developed flow, the liquid velocity profiles are found to parabolic in nature with the maximum velocity at the centre of the channel. The maximum velocity is found to be equal to 2.1 times the mean fluid velocity $U_{TP} = (U_{LS} + U_{GS})$.
- There appears to be systematic differences in quantitative comparison of predicted and experimental results. Further work is needed to resolve these differnces. Despite the differences, normalized (with maximum velocity) predicted results showed good agreement with normalized experimental data of Tsoligkas et al., (2007).
- Methodology was developed to estimate mass transfer in gas-liquid slug flows. As a sample of results, mass transfer coefficient was predicted with one of the considered cases which showed reasonably good agreement with the correlation of Bercic and Pintar (2003).

Chapter 4

Chemical Reaction Engineering Model

4.1. Introduction

An important aspect in design of any reactor is to develop reaction engineering model that can simulate conversion and selectivity of different chemistries that can be practiced using these reactors. These models incorporate various transport processes (mixing, heat and mass transfer) along with reaction kinetics to predict conversion and selectivity. Such models help to identify safe, useful and optimal operating window for a particular reaction in a given reactor. These models also help to classify reactions which can be advantageously carried out in a particular reactor.

Microreactors, because of their very high surface to volume ratio compared to conventional reactors, have recently become very popular to try new, complex and fast chemistries. Many industrially important reactions which have selectivity and conversion issues are also being explored in microreactors. A brief review of such studies was reported by Pennmann et al. (2004) and it was observed that many of these studies showed positive results with microreactors. However due to lack of chemical reaction engineering analysis the observed performance enhancement is not completely understood. Therefore the present work was undertaken to develop a general purpose reactor model that can be coupled with complex reaction kinetics to predict information on conversion and selectivity in microreactors. Further the models can be used to tailor reaction conditions suitable for optimum conversion and selectivity for a given reaction kinetics.

In the present work a generalized reactor model for microreactors is formulated. Since microreactors are an array of number of identical flow channels, any gas-liquid or gas-liquid-solid reactions can be modeled as a tubular reactor in which both gas and liquid can be assumed to be in co-current plug flow and solid catalyst coated on the channel walls. Non-ideal mixing can be taken into account by a dispersion coefficient. In order to keep the developed model equations generic and independent of any specific flow regimes, correlations for hydrodynamic parameters such as holdup, mass transfer coefficient, dispersion coefficient etc. were incorporated in a separate module which can be plugged into generalized reaction engineering model.

The model equations consist of dynamic, mass and energy balances for any gas-liquid and gas-liquid-solid reactions (solid is considered as catalyzed walls) in micro-channels. Separate balance equations are written for each component in the respective phases. These model equations can also be coupled with generalized model equations discerning the regime of the gas-liquid reactions at any location within the reactor. The developed model equations are simulated using gPROMS simulation environment (of PSE, UK).

4.2. Model

A generalized model for co-current gas liquid flow through single channels is formulated. Figure 4.1 shows the typical graphical representation of the model. Gas and liquid are assumed to behave in plug flow manner with channel wall catalyzed.
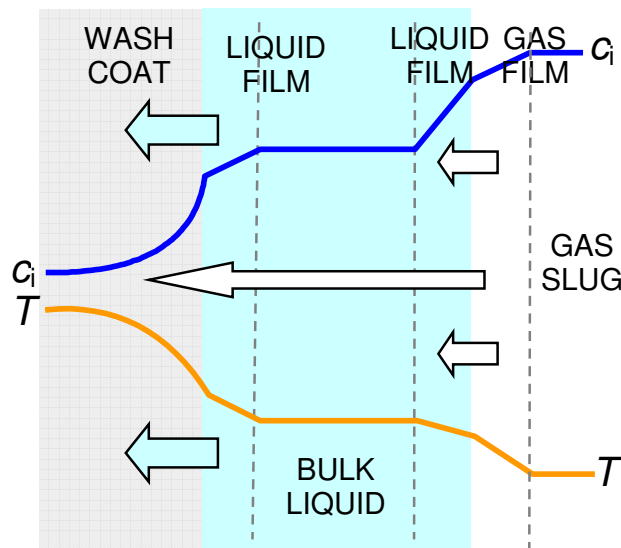
Figure 4.1: Model Representation

4.2.1. Model equations

Liquid phase mass balance for individual components

$$\frac{\partial}{\partial t}\left(\varepsilon_{L\_f}\, C_{i,L\_f}\right) \;=\; -\; \frac{\partial}{\partial z}\left(U_{L\_f}\, C_{i,L\_f}\right) \qquad\qquad Convection$$

$$+\; D_{ax,L\_f}\frac{\partial^2}{\partial z^2}\left(\varepsilon_{L\_f}\, C_{i,L\_f}\right) \qquad\qquad Dispersion$$

$$+\; \left(\left(1-\varepsilon_{L\_f}\right)\phi k_{GL}\, a_{GL}\left(C_i^{*}-C_{i,L\_f}\right)\right) \quad Mass\,Transfer$$

$$-\;\left(\varepsilon_{L\_f}\, k_{LS}\, a_{LS}\left(C_{i,L\_f}-C_{i,S}\right)\right)$$

$$-\;\varepsilon_{L\_f}\sum \upsilon_{i,j}\, r_j \qquad\qquad\qquad Re\,action$$

(4.1)

Boundary conditions

$$z \;=\; 0 \qquad D_{ax,L\_f}\frac{\partial}{\partial z}\left(\varepsilon_{L\_f}\, C_{i,L\_f}\right) \;=\; U_{L\_f\_in}\, C_{i,L\_in}-\; U_{L\_f}C_{i,L\_f} \qquad (4.2)$$

$$z \;=\; L \qquad \frac{\partial}{\partial z}\left(\varepsilon_{L\_f}\, C_{i,L\_f}\right) \;=\; 0 \qquad\qquad\qquad (4.3)$$

Gas Phase Mass Balance

$$\frac{\partial}{\partial t}\left(\varepsilon_{G\_f}\frac{p_i}{RT}\right) \;=\; -\; \frac{\partial}{\partial z}\left(U_{G\_f}\frac{p_i}{RT}\right) \qquad\qquad Convection$$

$$+\; D_{ax,G\_f}\frac{\partial^2}{\partial z^2}\left(\varepsilon_{G\_f}\frac{p_i}{RT}\right) \qquad\qquad Diffusion$$

$$-\;\left(\varepsilon_{G\_f}\,\phi k_{GL}\, a_{GL}\left(C_i^{*}-C_{i,L\_f}\right)\right) \qquad Mass\,Transfer$$

(4.4)

Boundary Conditions

$$z \;=\; 0 \qquad D_{ax,G\_f}\frac{\partial}{\partial z}\left(\varepsilon_{G\_f}\frac{p_i}{RT}\right) \;=\; U_{G\_f\_in}\left(\frac{p_{i\_in}}{RT}\right)-\; U_{G\_f}\left(\frac{p_i}{RT}\right) \qquad (4.5)$$

$$z \;=\; L \qquad \frac{\partial}{\partial z}\left(\varepsilon_{G\_f}\frac{p_i}{RT}\right) \;=\; 0 \qquad\qquad\qquad (4.6)$$

Energy Balance

$$\frac{\partial}{\partial t}\left(\varepsilon_{L\_f}\ \rho_{mix,L\_f}\ C_{p\_mix,L\_f}\ T\right)=\frac{\partial}{\partial z}\left(U_{L\_f}\ \rho_{mix,L\_f}\ C_{p\_mix,L\_f}\ T\right)-\left(\varepsilon_{L\_f}\left(\sum_j r_j\Delta H_{rxn}+\sum_k r_{V,k}\Delta H_{rxn}\right)\right)$$

$\qquad\qquad$ *Accumulation* $\qquad\qquad\qquad\qquad$ *Convection* $\qquad\qquad\qquad\qquad$ *Heat of reaction*

$\hfill$ **4.7**

Boundary Conditions

$z\ =\ 0\qquad T\ =\ T_{in}$ $\hfill$ **4.8**

Wash-coat Mass Balance

$$\frac{\partial}{\partial t}\left(\varepsilon_{L\_wc}\ C_{i,L\_wc}\right)\ =\ D_{eff,L\_wc}\ \frac{\partial^2}{\partial r^2}\left(\varepsilon_{L\_wc}\ C_{i,L\_wc}\right)\ -\ \varepsilon_{L\_wc}\sum_j \upsilon_i r_{V,k}$$

$\hfill$ **4.9**

$\qquad\qquad$ *Accumulation* $\qquad\qquad\qquad$ *Diffusion* $\qquad\qquad\qquad\qquad$ *reaction*

Boundary Conditions

$r\ =\ r_{wc}\qquad D_{eff,L}\ \frac{\partial}{\partial r}\left(\varepsilon_{L\_wc}\ C_{i,L\_wc}\right)\ =\ \varepsilon_{L\_f}\ k_{LS}\ a_{LS}\left(C_{i,L\_f}-C_{i,S}\right)$ $\hfill$ **4.10**

$r\ =\ R\qquad \frac{\partial}{\partial r}\left(\varepsilon_{L\_wc}\ C_{i,L\_wc}\right)\ =\ 0$ $\hfill$ **4.11**

4.3. Case study: Hydrogenation of 2,4,DNT

To demonstrate the application of the developed model a case study of hydrogenation of 2,4,DNT is considered. The process was selected because it is a fast reaction which benefits from the good mass transfer characteristics. The hydrogenation of 2,4,DNT to 2,4,TDA is highly exothermic (ΔH_R = -550kJ/mol per nitro group converted), and heat removal is a primary concern. Typically stirred tank slurry reactors with internal cooling are used on a commercial scale and dinitrotoluene is introduced into the reactor at concentrations of 5-15mol/m^3 along with the solvent. Solvent helps to lower the reaction rates and moderate the

high temperature rise of the reaction medium by evaporation. The solvent used in this process is 2,4,TDA. The upper limit for the operating temperature depends on the rate of unwanted side reactions. At temperatures above 430K, DNT starts to decompose, leading to a strong rise in temperature that may lead to an explosion. Within the desired temperature limits (371-430K), the vapour pressure of 24TDA is below 1kPa, and product evaporation can be ignored.

Following assumptions are made in the reactor model for the hydrogenation of 2,4-dinitrotoluene (24DNT) to 2,4-toluenediamine (24TDA) in microreactor

- No catalyst deactivation
- No internal temperature gradients
- No evaporation of liquid phase components
- Gas and liquid temperature in equilibrium
- Both gas and liquid flows are assumed to be in Plug flow
- Reactions occurs only on the catalyst walls

4.3.1. Kinetics

The kinetics of 2,4,DNT hydrogenation has been reported in open literature. The reaction is known to proceed via two intermediates, 2-amino-4-nitrotoluene (2A4NT) and 4-amino-2-nitrotoluene (4A2NT) to the final product, 24TDA. The reaction pathway is shown in Figure 4.2. In this study, the kinetics of Malyala and Chaudhari (1999) at 333K using a Nickel catalyst has been used. All kinetic parameters have been listed in Table 4.1. The volumetric rates of the individual reactions follow Langmuir-Hinshelwood kinetics, where the rate limiting step is a reaction of adsorbed dissociated hydrogen with a nitro-aromatic compound. Numbering the reactions according to Figure 4.2 the rate expressions are given by Equations

$$r_{v,1} = \frac{k_1 \sqrt{c_H} c_A}{(1 + \sqrt{K_H c_H} + K_A c_A + K_B c_B)^2} \qquad \textbf{4.12}$$

$$r_{v,2} = \frac{k_2 \sqrt{c_H} c_A}{(1 + \sqrt{K_H c_H} + K_A c_A + K_B c_B)^2} \qquad \textbf{4.13}$$

74

$$r_{v,3} = \frac{k_3 \sqrt{c_H} c_B}{(1 + \sqrt{K_H c_H} + K_A c_A + K_B c_B)^2}$$ 4.14

$$r_{v,4} = \frac{k_4 \sqrt{c_H} c_C}{(1 + \sqrt{K_H c_H} + K_A c_A + K_B c_B)^2}$$ 4.15

The subscripts H, A, B and C denote hydrogen, 24DNT, 4A2NT and 2A4NT respectively. The temperature dependency of the rate constants, k_i and the adsorption coefficients, K_j are given by the Arrhenius equations

$$k_i(T) = k_i(T_{ref}) \exp\left[\frac{-E_A}{R}\left(\frac{1}{T} - \frac{1}{T_{ref}}\right)\right]$$ 4.16

$$K_j(T) = K_j(T_{ref}) \exp\left[\frac{-\Delta H_j}{R}\left(\frac{1}{T} - \frac{1}{T_{ref}}\right)\right]$$ 4.17

Since the temperature in the column increases considerably, the viscosity of 24TDA cannot be considered as constant throughout the column. The viscosity was calculated at each axial position inside the column. The diffusion coefficients were calculated using Wilke-Chang's correlation. Since the diffusion coefficients predicted by this are strong functions of viscosity, they are also calculated at each axial position. An overview of the physical properties is given in Table 4.2
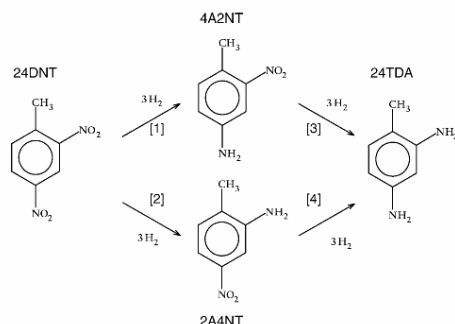
Figure 4.2: Reaction pathway for 2,4-dinitrotoluene (24DNT) to the intermediates 2-amino-4nitrotoluene (2A4NT) and 4-amino-2-nitrotoluene (4A2NT) and subsequently to product 2,4-toluendiamine

Table 4.1: Kinetic Parameters

i	k_i (333K) (m^3/mol/s)	$E_{A,j}$ (kJ/mol)
1	5.20×10^{-2}	30.7
2	6.88×10^{-3}	33.2
3	8.54×10^{-3}	31.0
4	4.68×10^{-3}	33.8

j	K_j (333K) (m3/mol)	ΔH_j, (kJ/mol)
H_2	9.36×10^{-4}	-34.07
24DNT	1.11×10^{-2}	-14.11
4A2NT	9.8×10^{-4}	-12.19

Table 4.2: Physical Properties

Hydrogen	
Henry coefficient	0.44 mol/m^3/bar
Diffusion coefficient (383K)	2.3×10^{-8} m^2/s
Diffusion coefficient (433K)	5.9×10^{-8} m^2/s
Water	
Diffusion coefficient (383K)	7.5×10^{-9} m^2/s
Diffusion coefficient (433K)	1.9×10^{-8} m^2/s
24TDA	
Density	1020 kg/m^3
Viscosity (383K)	7.4×10^{-4} Pa s
Viscosity (433K)	3.2×10^{-4} Pa s
Surface Tension	4.2×10^{-2} N/m
Heat Capacity	3.1 kJ/kg/K
24DNT, 2A4NT, 4A2NT, 24TDA	
Diffusion Coefficient (383K)	1.9×10^{-9} m^2/s
Diffusion Coefficient (433K)	4.9×10^{-9} m^2/s

4.3.2. Hydrodynamic parameters

The hydrodynamic parameters used in the model are obtained from the correlations available the literature. For example the film thickness is calculated using Aussilous and Quere (2000) correlation.

$$\delta = d_c \left(\frac{0.66 \, Ca^{\frac{2}{3}}}{1 + 3.33 \, Ca^{\frac{2}{3}}} \right) \qquad\qquad 4.18$$

where

$$Ca = \frac{\mu U_{TP}}{\sigma} \qquad\qquad 4.19$$

For the transfer of components to the catalyst surface the correlation proposed by Kreutzer et al. (2003) was used. The correlation is valid for full mass transfer limited reactions

$$k_{GS} = \varepsilon_G \frac{D}{\delta} \qquad\qquad 4.20$$

$$k_{LS} = \varepsilon_L \left(\frac{\delta}{D} + \frac{d_{ch}}{Sh \, D} \right)^{-1} \qquad\qquad 4.21$$

where

$$Sh = 90 + 104 \left(\frac{L_{slug}}{d_{ch}} \right)^{-\frac{4}{3}} \qquad\qquad 4.22$$

Studies from the literature (Jensen et al., 2005 and Kreutzer et al. 2003) indicate that the residence time distribution in a capillary is close to that of plug flow so a constant value of assumed.

4.3.3. Numerical solutions

The simulations were performed for the experimental data discussed in Chapter 2. Although the earlier experiments were carried out at room temperature and atmospheric pressure, it is assumed that the similar flow conditions prevail at operated pressures and temperatures in the simulation. Also it is assumed that the channels are coated in such a way that the channel cross-section is circular with a diameter of 0.84mm and such that the wash-coat thickness is

as considered for the simulation (25µm for the base-case). Inside the column, the bubbles shrink due to the consumption of hydrogen and operating the column at higher pressures ensures that the bubbles retain their elongated shape and Taylor flow is ensured all along the reactor. Base case formulation is as given in Run 1 of the Table 4.3.

The partial differential equations described in the model were discretized using the Central Finite Difference Method (CFDM) on a 2D grid of 100 points in the axial direction and 15 points in the radial (wash-coat) direction Here it is important to mention that the domain in the wash-coat region is only, discretized in radial direction.. The initial conditions for the simulation were that all variables were equal to the feed conditions. The resulting ODEs were integrated till steady state was reached. Simulations were performed using gPROMS simulation environment (of PSE, UK). Grid sensitivity studies were done for the base case and its effect was found to be negligible.

4.4. Results and discussion

Before we go into discussion of the results, it is important here to mention that the case-study was selected because the reaction is very fast and highly exothermic and forms an ideal case-study for studies in microreactors. Such a study shall be useful to demonstrate the application of the developed model. However, since all the reactant is finally getting converted into product, the question of selectivity and yield isn't of much importance for this particular case. To illustrate possible influence on selectivity, for the purpose of present study, 4A2NT was assumed to be a desired product and influence of various parameters on yield of this intermediate product 4A2NT was examined.

Figure 4.3 shows the concentration profile of the aromatic liquids at different space time $\left(\tau = \dfrac{L}{U_{LS}} \right)$ of the reactor for the base case formulation. As can be seen more than 99 % of the reactant is converted into the product after $100\,\tau$. The maximum conversion of the 4A2NT was observed around 60τ. The temperature rise in the reactor is 43K which is just within the desired temperature limit of 430K. Figure 4.4 shows the component concentration in the catalyst wash-coat in the radial direction. Though each molecule of 24DNT consumes 3 molecules of hydrogen for conversion, the effect of reaction on the concentration profile of 24DNT in the wash-coat is more pronounced since the diffusion co-efficient of 24DNT is lower than that of hydrogen. The high concentration of hydrogen in the catalyst prevents its deactivation.
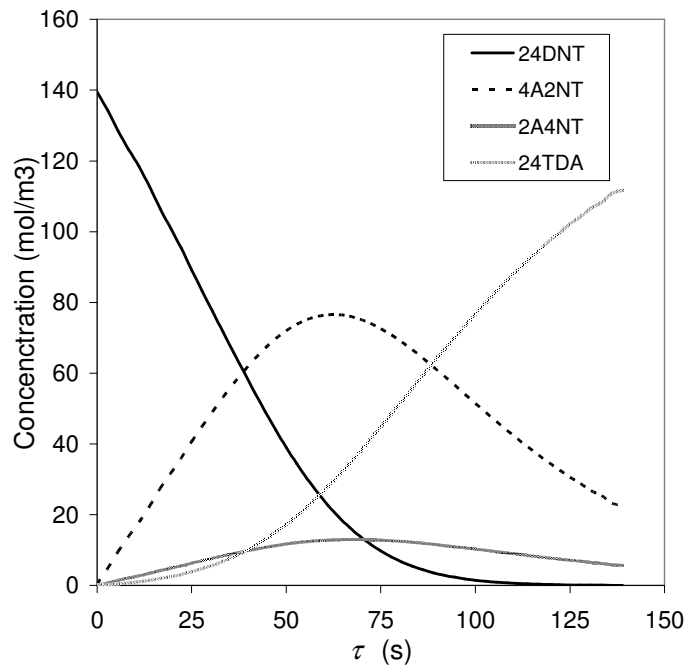
Figure 4.3: Concentration Profile of Aromatic compounds at various space times of the reactor (P=16bar)
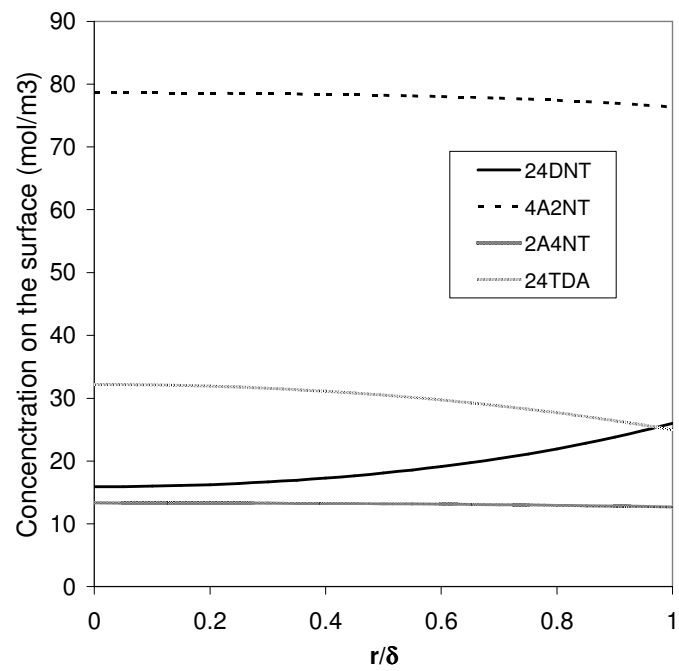
Figure 4.4: Concentration profile in the catalyst wash-coat at z =2m

Different simulations were performed to check the sensitivity of different parameters on the selectivity of 4A2NT. Table 4.3 summarizes all the simulations performed. The conversion of 24DNT and selectivity of 4A2NT was calculated as given below

$$Conversion \;\; = \;\; \frac{moles\ of\ 24DNT\ consumed}{moles\ of\ 24DNT\ feed} \qquad \textbf{4.23}$$

$$Selectivity \;\; = \;\; \frac{moles\ of\ 4A2NT\ formed}{moles\ of\ 24DNT\ consumed} \qquad \textbf{4.24}$$

Since the product 4A2NT is an intermediate product it reaches maximum and drops thereafter along the length of the reactor, hence for all the simulations an optimum space time (τ_{opt}) at which the maximum concentration of the product is obtained is determined. All the parametric sensitivity studies were reported for this (τ_{opt})

Table 4.3: Details of the variation of parameters used in the parametric sensitivity simulations

Run No	d_{ch} (mm)	L_{ch} (m)	δ_{WC} (μ)	U_{Ls} (m/s)	U_{Gs} (m/s)	C_{in} (mol/dm^3)	T_{in} (K)	P (bar)	Pe	T_{out}
1.	0.84	5	25	0.036	0.088	140	383	16	500	426.8
2.	0.84	5	25	0.036	0.088	70	383	16	500	404.1
3.	0.84	5	25	0.036	0.088	40	383	16	500	394.8
4.	0.84	5	25	0.036	0.088	140	383	32	500	430.5
5.	0.84	5	10	0.036	0.088	140	383	16	500	414.8
6.	0.84	5	40	0.036	0.088	140	383	16	500	428.3
7.	0.84	5	25	0.036	0.088	140	383	16	50	426.3
8.	0.84	5	25	0.036	0.088	140	383	16	5000	426.8
9.	0.5	5	25	0.036	0.088	140	383	16	500	430.2
10.	1.5	5	25	0.036	0.088	140	383	16	500	413.6

Run 2 and Run 3 show the effect of operating the reactor at lower feed concentration. Figure 4.5 compares the selectivity and conversion for all the three cases. Selectivity decreases with decrease in feed concentration. This is because the reaction is very fast and exothermic at higher inlet concentrations higher conversions of 24DNT at shorter lengths due to increased concentration gradients. Because the reaction is exothermic for the same conversion of

24DNT, amount of heat released per unit length is higher thereby causing higher temperature rise. Since the value of rate constant (k) for reaction 1 is greater then that for reaction 2, rate of reaction 1 ($r_{V,1}$) is more benefited by the increased temperature as compared to rate of reaction 2 ($r_{V,2}$) and hence the selectivity of 4A2NT
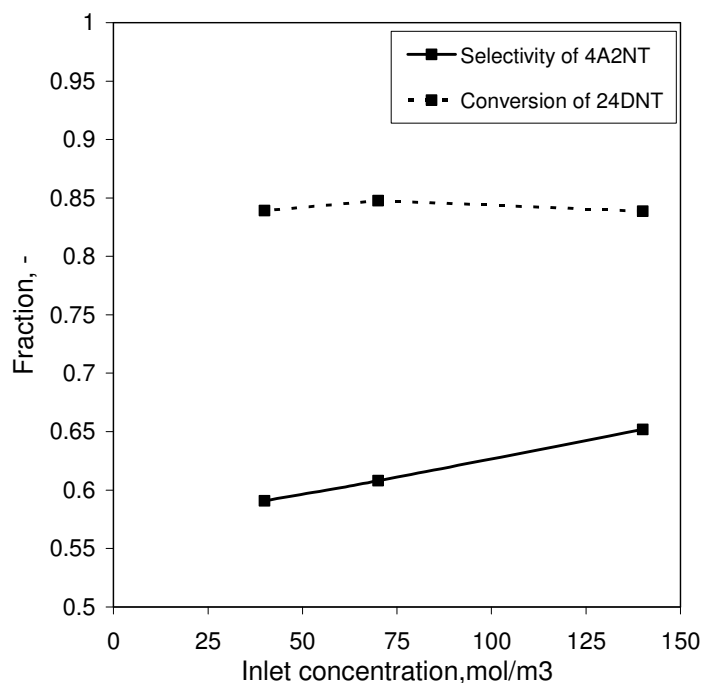
Figure 4.5 : Effect of inlet concentration on conversion and selectivity (4A2NT)

Run 4 show the effect of increasing the reaction pressure. At higher pressure the rate of the reaction increases, but the residence time of the liquid inside the column is decreased. A lower fraction of gas is consumed as a result the conversion and selectivity of 4A2NT decreases. Similar observations are also made for increase in the superficial gas velocity (Figures 4.6 and 4.7). Run 5 & 6 shows the effect of using a thinner and thicker wash-coat. Conversion and selectivity of 4A2NT are found to decrease with increase in the wash-coat thickness (Figure 4.8).

Run 7 & 8 show the effect of axial dispersion coefficient. Figure 4.9 indicate no change in conversion where as selectivity is slightly reduced for higher dispersion indicating plug flow behavior is desirable.

Finally run 9 and 10 show the effect of varying the channel diameter. Figure 4.10 indicate negligible change in the conversion however, Selectivity of 4A2NT increases with decreasing channel diameter. This is because of following reasons: The reaction is mass transfer limiting (very fast reaction). Decreasing the channel diameter increases the mass transfer rates because of increased gas-liquid interfacial area per unit volume of the reactor. Due to increased mass transfer rates the same conversions are obtained at shorter lengths within the reactor. As explained earlier this causes increase in the selectivity at lower channel diameters.
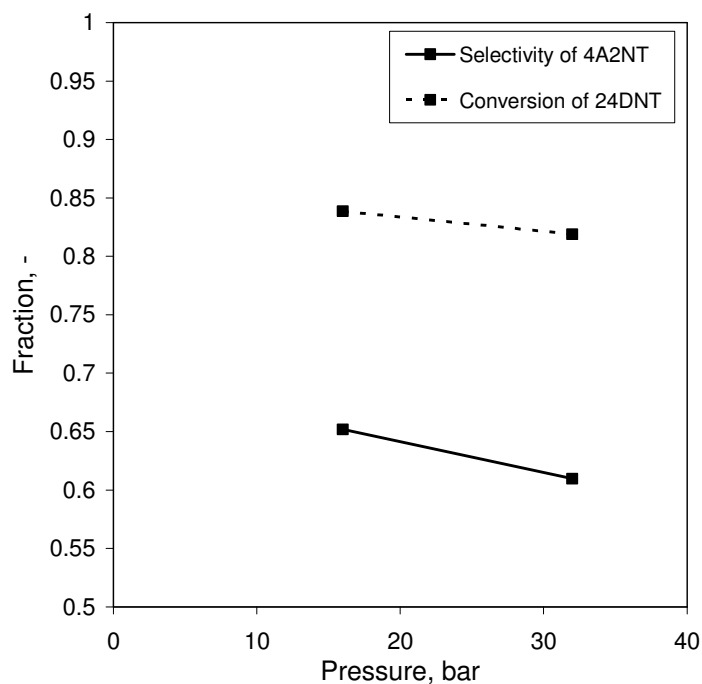
Figure 4.6 : Effect of pressure on conversion and selectivity (4A2NT)
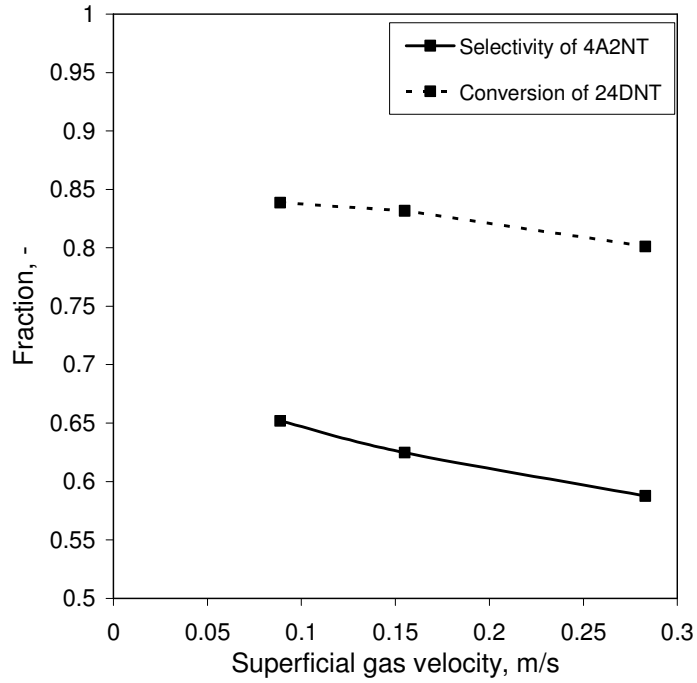
Figure 4.7 : Effect of superficial gas velocity on conversion and selectivity (4A2NT)
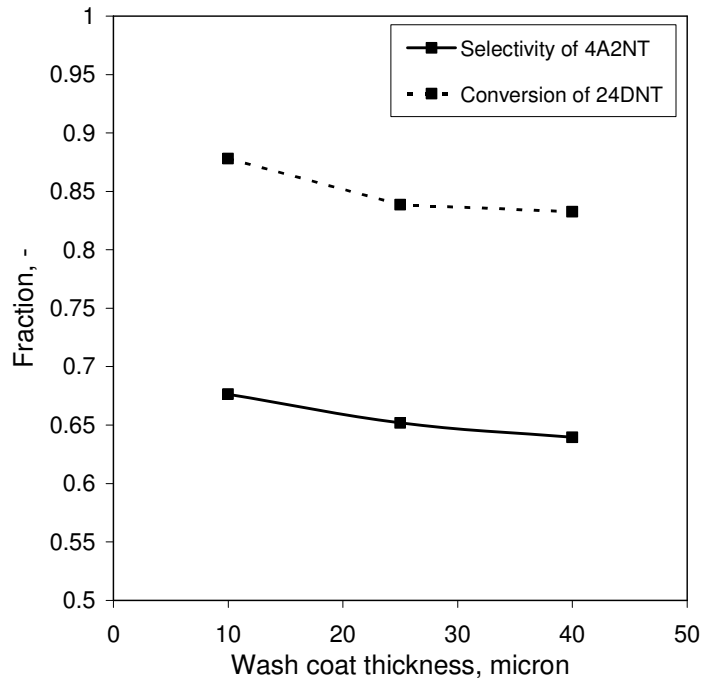
Figure 4.8 : Effect of wash-coat thickness on conversion and selectivity (4A2NT)
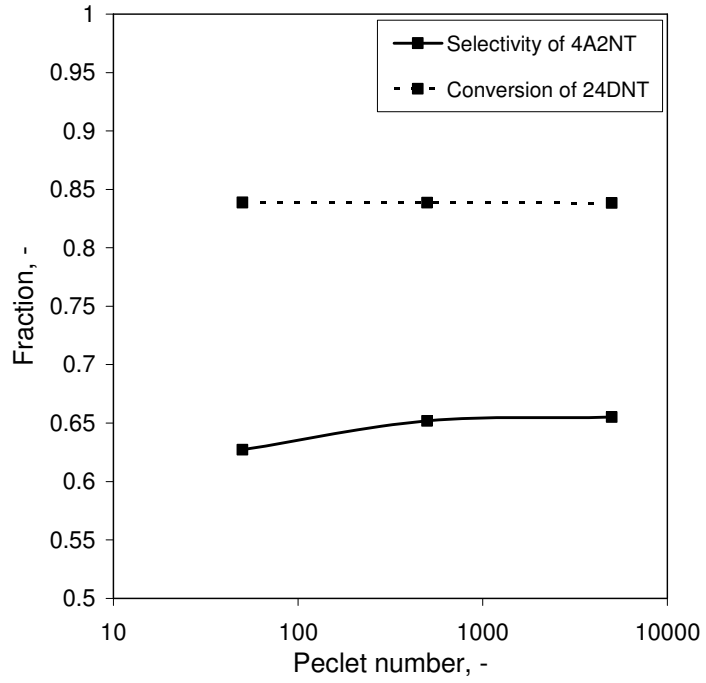
Figure 4.9 : Effect of Peclet number on conversion and selectivity (4A2NT)
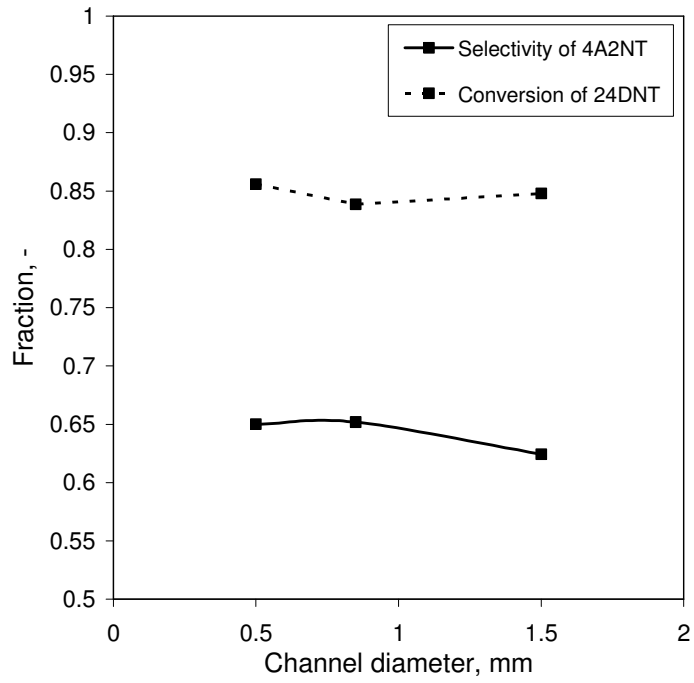
Figure 4.10 : Effect of channel diameter on conversion and selectivity (4A2NT)

4.5. Conclusions

Following conclusions can be drawn from the above study

- A generalized reactor model based on mass and energy balance is developed

- The model is quite general and can account for any gas-liquid, liquid-liquid and gas-liquid solid reactions in microchannel. Also the model equations are independent of any specific flow regimes. Correlations for different hydrodynamic parameters determined independently (as discussed in the pervious chapter 2 &3) can be plugged into the model equations

- A case-study of hydrogenation of 24DNT was used to demonstrate the application of the developed model.

- Several parametric studies were conducted to study effect of various operating parameters on conversion and selectivity of 4A2NT.

- The tool can be useful for deciding the operating parameters to be used while conducting experiments using capillary-microreactors

Chapter 5

'Mesh-microreactor'

5.1. Introduction

Many investigators have designed and demonstrated various designs of microreactors for reactions of different types (viz. single and multiphase, catalytic and non-catalytic reactions). Although for many of these devices some engineering analysis has been reported, no specific design procedures are developed that would give a guideline for design and development of the same. Recently a few studies (Pfund et al. 2000, Yeong et al. 2004, Traschel et al. 2005, Abdallah et al. 2006) report estimation of a few design parameters or hydrodynamic properties (viz. pressure drop, RTD, mixing and dispersion, mass transfer coefficient, etc.) of different microdevices. However, the information in the literature is discrete and can not be connected to derive any design procedures. As emphasized by Hasebe (2004), now that the potential of microreactors for various applications has been recognized, it is necessary to carry out certain experiments and simulations that would help to design these microreactors for different applications.
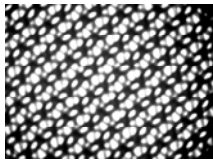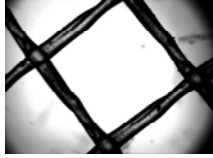
Conventionally, for gas-liquid and gas-liquid-solid reactions, fixed bed reactors, slurry bubble columns, three phase stirred reactors are used. At microscale operation, although analogous devices of reduced dimensions have been studied, the factors that affect the performance are largely different than the conventional designs. Here we focus on a microreactor for gas-liquid and gas-liquid-solid catalytic reactions. A few attempts that demonstrate feasibility of the technology for three phase reactions include hydrogenation in catalyst coated microchannels, hydrogenation of cyclohexene in fixed bed reactor (Losey et al. 2001), recycle loop reactor for hydrogenation of 2-butyne-1,4-diol using Pd loaded on activated carbon fibers (Kiwi-Minsker, et al. 2004), mesh microreactor for gas-liquid, gas-liquid-solid oxidation, hydrogenation and asymmetric hydrogenations (Wenn et al. 2003, Abdallah et al. 2004), etc. These studies have illustrated the feasibility of microreactors for multiphase reactions and would offer great potential if approach is developed for enhancing the operational capacity. In this work we have studied a microreactor which contains several connected microvolumes. It offers better contact among gas, liquid and solid phases and is also easier to scale-up. It is easy to build and does not need any high end micromachining.

5.2. Experimental setup

The present study aims at studying the hydrodynamics of a mesh microreactor. For this purpose, the microreactor was fabricated in transparent polyacrylate. The reactor mainly includes two flat acrylic sheets (5mm thick) which were used to sandwich a mesh of polypropylene. Four different types of mesh (100mm x 200 mm x mesh thickness) were studied. Details about the used meshes are given in Table 5.1 The mesh acts as a separator between the two plates maintaining a gap equal to the mesh thickness and also helps in realizing better contacting of gas-liquid phases. The mesh types were selected either in plain or flat top weaved form such that on sandwiching between two flat plates, the fluid will change the compartments (microvolume ranging between $0.003 – 0.054$ mm^3 depending upon the mesh type) as it would move towards the outlet. The microreactor has an inlet for liquid from the top and the gas is sparged through a slotted pipe below the liquid inlet. The gas entry pipe has tiny entry ports (~ 500 μm) at every 10 mm. The liquid which first of all enters in the inlet tank pushes the gas coming out of the downward oriented gas ports. Schematic of a mesh microreactor is shown in Figure 5.1. The woven meshes allow interaction between the surrounding mesh structures and intensify local mixing. The gas-liquid dispersion leaves the mesh microreactor through the bottom channel. The reactor is sealed properly on the remaining two sides of the plates such that no fluid leaks through it even at very high flow rates.

At the bottom of the reactor, two conducting copper wires (unpolished surface) of 50μ were placed with an acrylic support on both sides of the reactor. The wires were held parallel across the plate area that sandwiches the mesh (see Figure 5.1). While one end of each of the wires was wound over the acrylic support, the other ends were connected to a standard conductivity electrode (cell constant of 1.0) along with digital conductivity meter (M. S. Electronics, India, Model601E). This probe was used for measurement of local conductivity of the liquid phase. This specific arrangement was used for studying the residence time distribution (RTD) for the flow in the mesh reactor. The experimental procedure is discussed later.

Table 5.1: Specifications of the different Mesh used for the current work

Mesh		Thickness	Dimension of unit side	Open area (%)
M1		100 μm	0.25 mm	20
M2		200 μm	1 mm	40
M3		400 μm	2 mm	68
M4		700 μm	3 mm	95.8
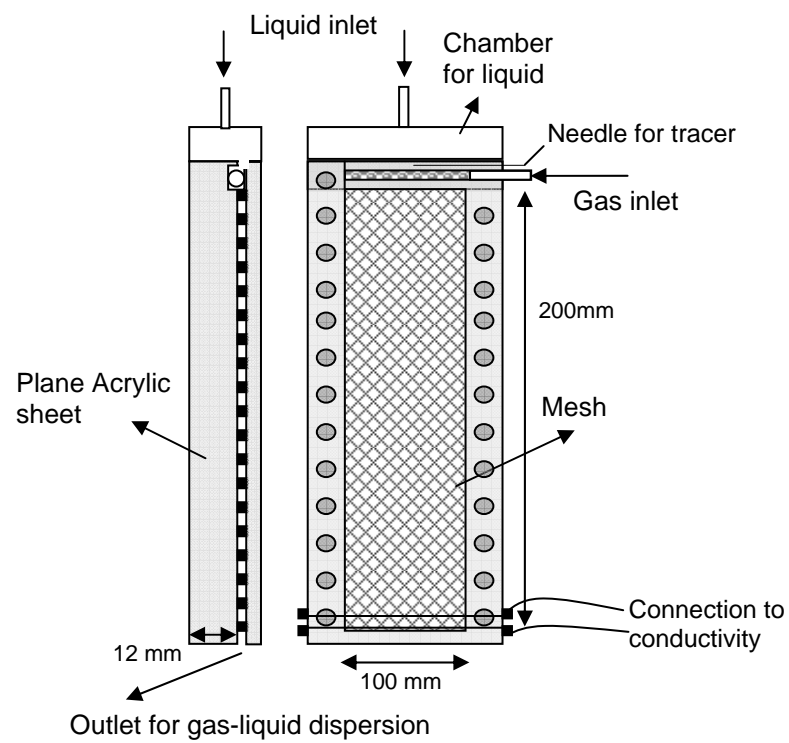
Figure 5.1: Schematic of the Mesh Microreactor

The mesh microreactor was operated for gas-liquid system (air and tap water in our case) in a continuous manner. The liquid entering from the top covered the gas inlet and thus carried the gas along with it while passing through the reactor. Air was supplied from a compressed air cylinder and a set of pre-calibrated rotameters were used to regulate and monitor the gas and liquid flow rates. The air and water flow rates could be varied in the range of 20 – 2500 ml/min and 50 – 800ml/min, respectively. Experiments were carried out to study the phase hold-up variation and RTD for different gas-liquid flow rates and for different mesh types.

5.3. Measurement techniques used in this work

A high speed CMOS camera (Red Lake, max frame rate: 2000fps), was used to acquire the data at 100 fps. The images were acquired over a region of 100mm x 100mm over the mesh reactor for all the experiments. A backlight provided better illumination of the focus area. The images were stored in a PC and later digitized using software ImagePro. For every combination of gas-liquid flow rates, minimum 1000 frames were obtained. For higher gas-liquid flow rates, more number of frames was obtained to capture the high frequency dynamic nature of the dispersed flow in the mesh region

The liquid phase RTD for various combinations of gas-liquid flow rates was measured by monitoring the variation in the liquid conductivity at the outlet of the microreactor. A pulse of 1 ml salt solution (NaCl, 20 gm in 100 ml water) was given manually (in less than 0.7 s) just above the mesh region where the gas-liquid flow has already entered the microreactor. The change in the concentration of salt solution at the exit was monitored using the two parallel copper wires kept open for the whole surface. Care was taken that the wires do not touch each other physically and only the continuously flowing liquid film between the wires would give the conductivity values with time. The data was acquired using a micro-computer via a 16-bit PCMCIA A/D converter card at a sampling frequency of 100 Hz for 100 s. The data was then processed separately to study the residence time distribution.

5.3.1. Image analysis

The images obtained using the high speed camera were analyzed for estimation of fractional phase volume occupied by gas and liquid. The images were also analyzed for the estimation of interfacial length that separates the two phases. Individual image was transformed into an array of pixel intensity using the software ImagePro. The digitized intensity data was further processed using a MATLAB code that analyzes the intensity array in a row-wise manner. For phase discrimination, the code estimates a threshold intensity value conditional to the intensity data from individual rows, which helps in better discrimination of the phases rather than applying a single threshold for the entire image. This procedure helped to deal with the unequal distribution of light intensity along the length of reactor. The processed data was further transformed in binary values conditional to the detected phase and a contour plot of the binary numbers was plotted to compare against the original image itself. The original image and the one in terms of binary data showed excellent resemblance and hence the binary data was used for further analysis. The phase hold-up values were obtained from the ratio of the pixel number that contains one of the binary numbers to the total number of pixels in the image. Since the solid hold-up values could be estimated from the mesh dimensions and thickness, suitable corrections were made in the estimated fluid phase hold-up. The changes from 0 to 1 or 1 to 0 were also traced and the number of pixels that fall at the gas-liquid interface was estimated. The pixel dimension and the number of pixels at the interface were used to estimate the length of interface available for gas-liquid contact. This procedure was followed for all the data sets acquired during the experiments.

5.3.2. Residence time distribution

The concentration profiles resulting out of a pulse of salt solution given at the reactor inlet were monitored at the outlet using the conductivity electrode. Typical distribution profiles at the outlet are shown in Figure 5.2 (a) – (b). The transient behavior of the conductivity of the outlet fluid was taken from the data and the mean residence time was obtained as (Levenspiel, 1999):

$$\bar{t} = \frac{\sum_{i=1}^{n} t_i c_i(t_i) \Delta t}{\sum_{i=1}^{n} c_i(t_i) \Delta t}$$

<div align="right">5.1</div>

where i corresponds to the sequential time element, n is the number of recorded data points. $c_i(t_i)$ is the observed time averaged conductivity at the outlet within the specified resolution of the data acquisition system. The time step Δt is defined as t_{i+1} - t_i , and is constant for the predefined data acquisition rate. For each flow rate, we analyzed three individual measurements separately. The average values were used for further analysis while the variation in the results is also noted for the sake of realizing the possible range of parameters that would be obtained from such experiments.

Initially, the Residence time distribution was studied using the standard tanks in series model. The acquired data was used to estimate the number of tanks (N) required for individual pulse responses and the estimated values of N and Pe were used to verify if the tanks in series model was appropriate one for the RTD studies of the system under consideration. As it can be seen in Figure 5.2, since the pulse response were having a relatively longer tail towards its end the tanks-in-series model yielded unreasonably large number of tanks ($1400>N>200$), which was not suitable for such tracer response. Moreover the estimated N and dispersion coefficient values failed to reproduce the E-curve for individual experiments. In view of this, the dispersion model with exchange between the static and dynamic concentration zones (van Swaaij et al. 1969, Iliuta et al. 1991), was applied and used to analyze the tracer response. The mesh microreactor was expected to have a few features similar to that of a trickle bed reactor. Hence the possibility of some tracer concentration being adsorbed and desorbed on the corners of the individual mesh elements, which would continuously exchange some of its mass with the dynamic concentration (that flows along with the liquid) segment was more likely. Importantly, (i) the mesh threads did not have any internal pores and (ii) no reaction takes place between the mesh threads and the liquid. Thus, the possibility of intra-particle tracer dilution does not exist significantly while the tracer adsorption/desorption can prevail.
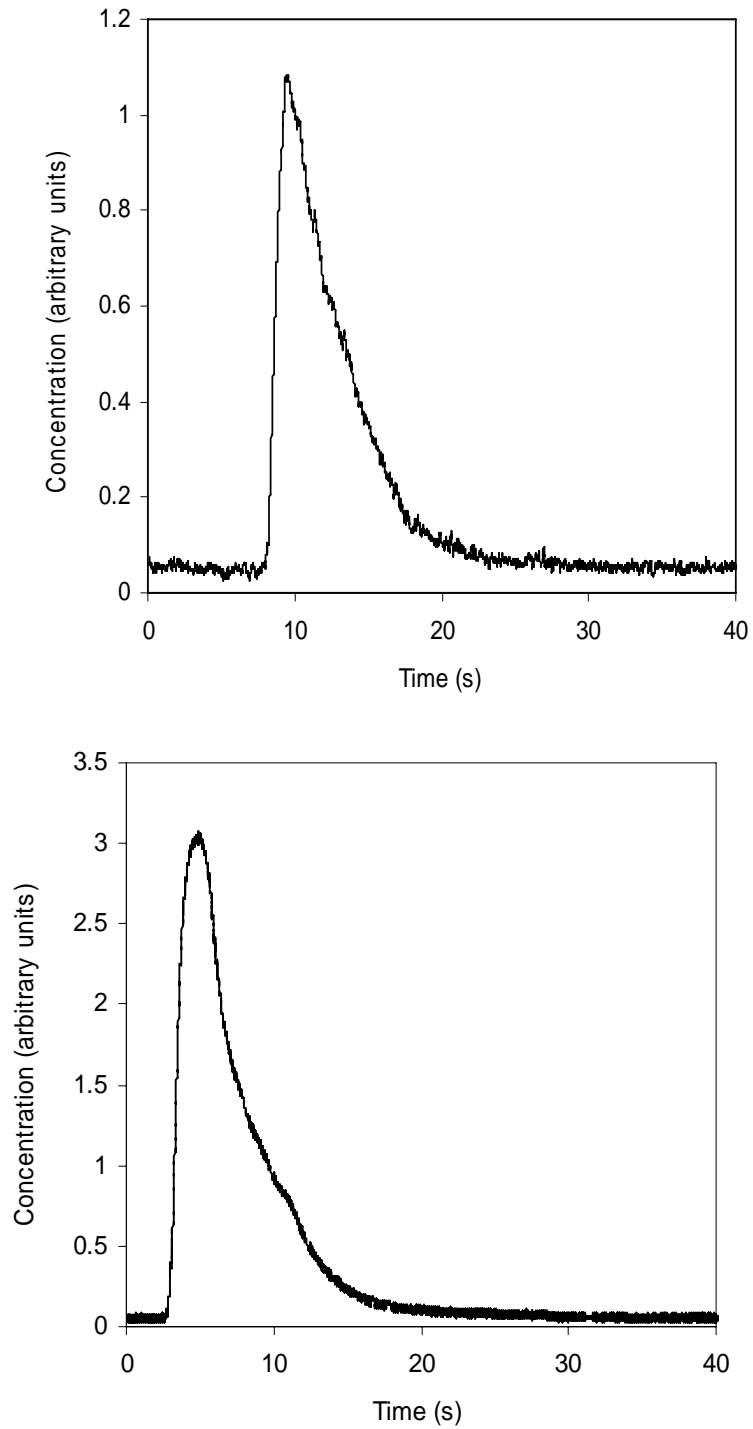
Figure 5.2: Typical concentration curve obtained at the reactor outlet for $Q_L = 400$ ml/min, $Q_G = 2486$ ml/min, Tracer volume 1 ml. A) Mesh 1, B) Mesh 4.

5.4. Axial dispersion exchange model

In view of the above conditions and the literature available on the variants of axial dispersion model with zonal exchange, it was decided to use the standard Axial Dispersion Exchange Model (ADEM) for our analysis. In ADEM, liquid phase back-mixing is an outcome of axial dispersion and mass interchange between dynamic and static regions. Axial dispersion in the flowing liquid is incorporated to improve RTD tail prediction. ADEM is particularly suitable for beds packed with nonporous particles.

Here, the data for liquid RTD in a mesh microreactor with individual mesh elements was studied by considering its similarity with the trickle bed reactor containing non-porous particles in the trickle-flow regime. The liquid structure with mesh elements (with nonporous threads) incorporates mass transport between both dynamic and external static liquid zones. the intra-mesh-element mass transfer was not considered. It was assumed that the liquid in the dynamic zone flows in an axially dispersed manner, whereas the external static zone is in direct contact with the dynamic zone and the threads of individual mesh element. Based on this flow or zonal structure, new data on liquid axial dispersion and mass transfer coefficients between dynamic and static zones were obtained and interpreted.

In trickle flow regime or the pulsating flow regime, the mesh elements are either partially externally wetted at tiny liquid flow rates, or utmost fully externally wetted at higher liquid flow rates. Thus typically it contains three zones (i) a dry zone covered by the gas phase, (ii) a wetted zone covered by the flowing dynamic liquid and (iii) a wetted zone covered by the stagnant liquid. With these assumptions, the RTD for the liquid in mesh microreactor with different mesh types were interpreted using ADEM. Possible distortion of RTDs by tracer adsorption/desorption was neglected. Tracer mass balance equations, respectively, in axially dispersed dynamic liquid zone and external liquid stagnant zone given in Iliuta et al. (1999) were used for simulations. The derivation of these equations and the solution methodology based on the method of moments can be seen in van Swaaij et al. (1969) and Villermaux and Van Swaaij (1969). The model equations are given below:

Dynamic liquid zone

$$\varepsilon_{L,d} \frac{\partial C_d}{\partial t} + \frac{v_L}{H}\frac{\partial C_d}{\partial x} + N\frac{v_L}{H}(C_d - C_{St}) = \frac{1}{Pe}\frac{v_L}{H}\frac{\partial^2 C_d}{\partial x^2}$$ **5.2**

Static liquid zone

$$\varepsilon_{L,St} \frac{\partial C_{St}}{\partial t} + N\frac{v_L}{H}(C_{St} - C_d) = 0$$ **5.3**

The relevant boundary and initial conditions are:

$$x = 0, \qquad \delta(\theta) = C_d \mid_{x=0^-} = C_d \mid_{x=0^+} - \frac{1}{Pe}\frac{\partial C_d}{\partial x},$$ **5.4**

$$x = 1, \qquad \frac{\partial C_d}{\partial x} = 0, \text{ and } t = 0, \quad C_d = C_{St} = 0$$ **5.5**

The model involves three tuning parameters viz. $Pe = v_L L/D$, k_L (exchange coefficient $k_L = Nv_L/H$ characterizing the mass transfer between dynamic and static liquid zones) and the dynamic $\varepsilon_{L,d}$ (or static $\varepsilon_{L,St}$) liquid hold-up. The tuning parameters were adjusted such that the difference in the mean and standard deviation values calculated for the experimental 'C' curve (measured at the exit of the mesh-reactor) and the simulated result is minimum Equations (2-3) were solved using gPROMS$^\copyright$ – 3.0.2. The confidence limits for the individual tuning parameters were assigned by repeating the simulations several times for the same experimental data.

5.5. Results and discussion

In this section we bring out our observations from the images and the concentration curves and subsequently discuss a few interesting aspects of a mesh microreactor. Hereafter, we indicate the different mesh types as M1, M2, M3 and M4 as given in Table 5.1

5.5.1. Characterization of gas-liquid flows in mesh-microreactor

The intensity data from images were used for the estimation of different hydrodynamic properties of the mesh-microreactor. For M2, large liquid slugs were seen to enter the mesh region and with minimal break-up move towards the exit. The slugs were formed on both sides of the mesh (slugs on two sides show different intensity, Figure 5.3) and they even cross the mesh from 'open area adjacent of one plate' to other (Figure 5.3d). However the formation of large slugs is undesirable as this may hamper the desired gas-liquid contacting.

<div align="center">(a)   (b)   (c)   (d)</div>
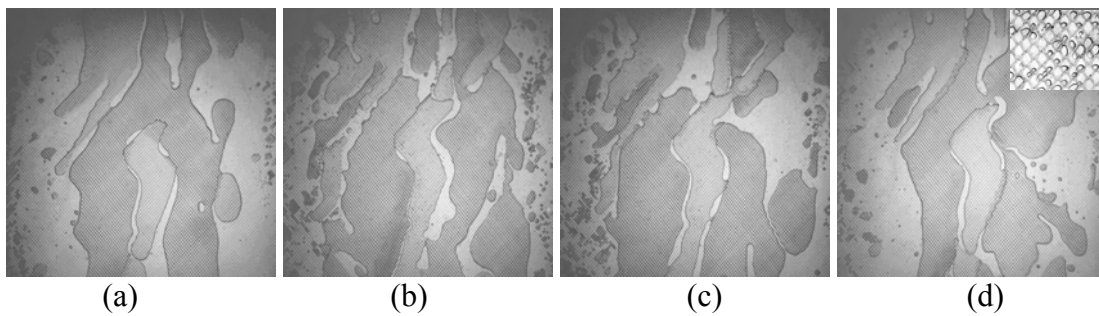
Figure 5.3: Images of a section (100mm x 100mm) of the mesh reactor with Mesh 2 for different gas and liquid flow rates. (a) Q_G = 1253 ml/min, Q_L = 602 ml/min, (b) Q_G = 2486 ml/min, Q_L = 151 ml/min, (c) Q_G = 2486 ml/min, Q_L = 301 ml/min, (d) Q_G = 2486 ml/min, Q_L = 602 ml/min. The internal figure in 'd' is a zoomed view.

The phase hold-up data were estimated using the digitized binary data sets. Analysis showed that for M2, ε_L was always higher than ε_G (Figure 5.4a) and at low gas flow rates, ε_G increased with Q_L. For a completely wet mesh, at higher Q_G ε_G was independent of Q_L, and it was function of Q_G and the open area. For M3, ε_G had a positive dependence on Q_G as well as Q_L (Figure 5.4 b). Due to relatively larger open area available for the flow, extent of channeling was less and a good quality gas-liquid dispersion prevailed in the reactor. At constant Q_G, increase in Q_L contributed to very small increase in ε_G (e.g. at Q_G = 2486 ml/min, with Q_L increased from 50 ml/min to 600 ml/min contributed for only 8% increase in ε_G). The images showed that lesser the open area (i) higher is the possibility of slug formation and (ii) higher is the slug size (channeling). With increasing Q_L due to more wetting of the mesh the overall transparency of the mesh increased yielding brighter images. However, gradual reduction in Q_L did not change the brightness of images significantly, but the channeling existed at lower Q_L. Thus, although the entire mesh was wet only small

section of the mesh was active for flow. As it can be seen in Figure 5.5 for the case of M1, at $Q_G = 2486$ ml/min, the plot of ε_G vs. Q_L was seen to go through a maximum. The smaller flow area resulted in very high gas-liquid velocities further reducing ε_G.
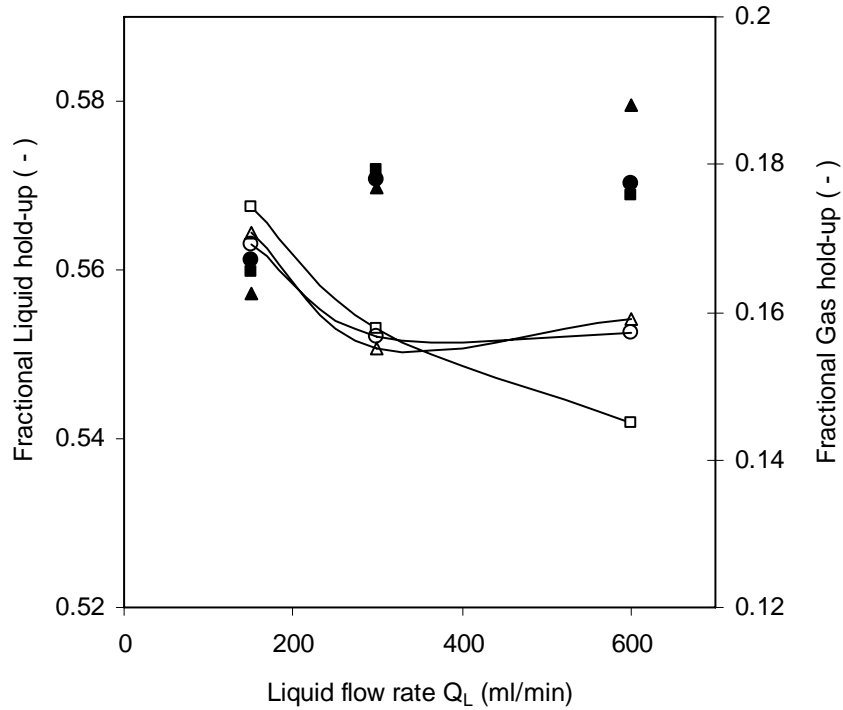
(a)
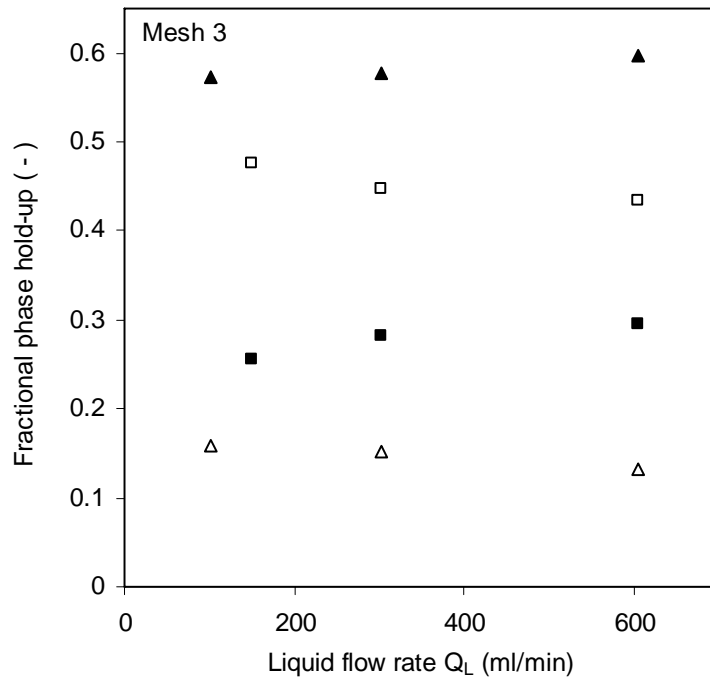
(b)

Figure 5.4: Variation in the estimated gas (filled symbols) and liquid hold-up (Open symbols) with Q_L for different gas flow rate Q_G (a) for Mesh 2 and (b) for Mesh3 (—□—, ■: $Q_G = 638$ ml/min; —▲—, △: $Q_G = 1254$ ml/min; —●—, O: $Q_G = 2486$ ml/min).

98
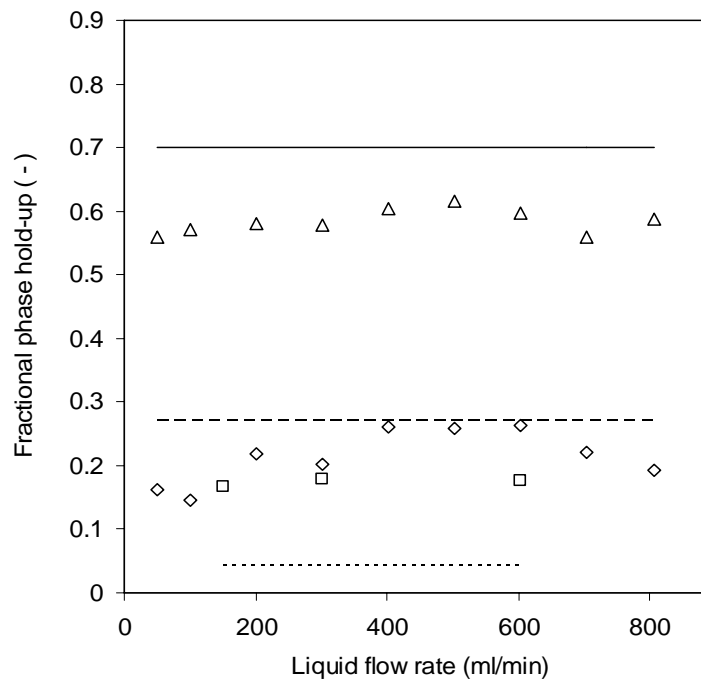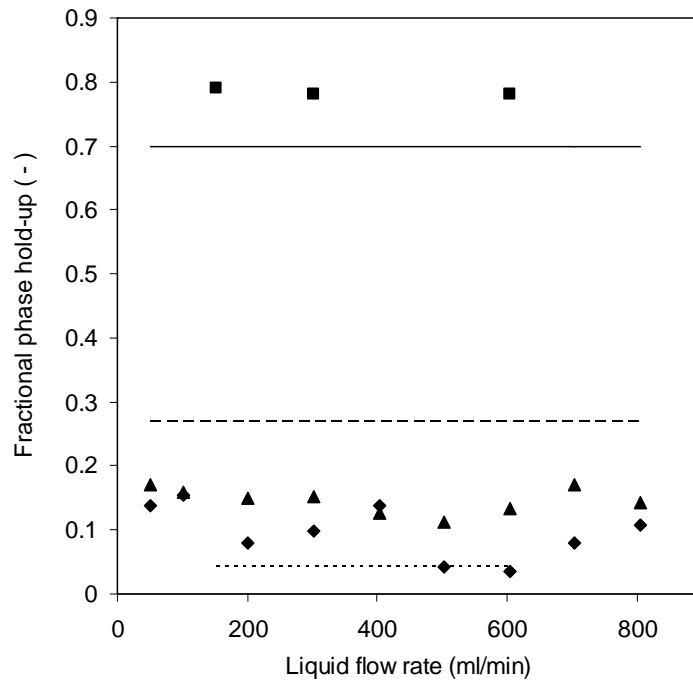
Figure 5.5: Variation in the phase hold-up for different mesh types at different gas and liquid flow rates. Open symbols – gas hold-up, filled symbols – liquid hold-up and solid lines – solid hold-up (,♦, ◊: Mesh 1;   , □, ■: Mesh 2; ----, ▲, Δ: Mesh 3)

The extent of dispersion or channeling can be expressed in terms of the length of gas-liquid interface (L_{int}). Higher is the value of L_{int}, better is the dispersion and the lower values would lead to channeling. Typical observations are shown in Figure 5.6. At the highest Q_L and Q_G, the value of L_{int} was relatively lower due to inability of capturing the rapid break-up of gas jets along with high velocity liquid slugs. At $Q_G = 2486$ ml/min, for M1 and M3 the value of L_{int} was seen to have weak dependence on Q_L, while for M2, it decreased at higher liquid flow rates. At lower Q_G, the values of L_{int} were higher than for $Q_G = 2486$ ml/min. The deviation from the trend possibly corresponds to different flow regimes due to wetting status and active flow region.
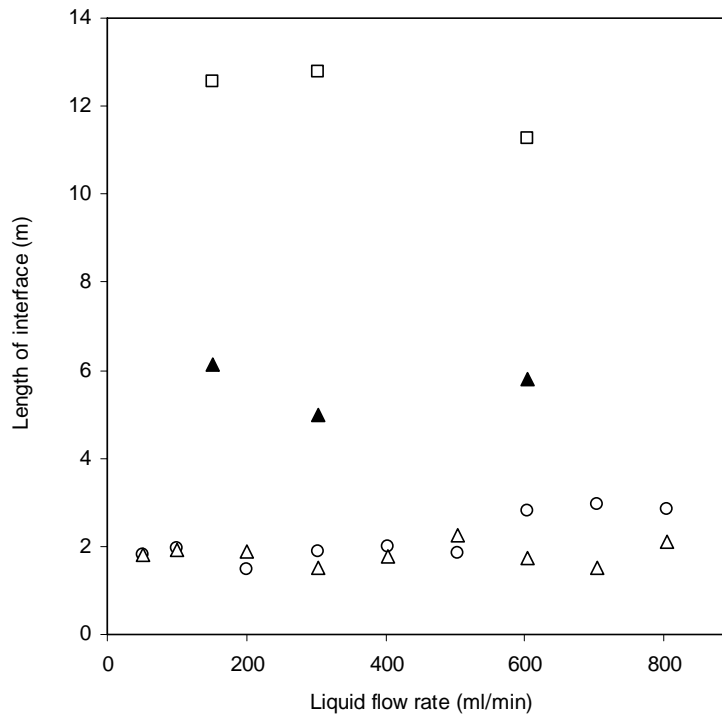
Figure 5.6: Effect of liquid flow rate on the interfacial length for three different mesh types. The gas flow rate was maintained at 2486 ml/min. (O - Mesh 1; □ - Mesh 2; Δ - Mesh 3, all at $Q_G = 2486$ ml/min and ▲ - Mesh 3 at $Q_G = 1254$ ml/min).

The images at lower Q_G and Q_L showed interesting features (Figure 5.7). In all the cases at for $Q_L > 150$ ml/min and $Q_G > 500$ ml/min, the images at different time instants showed the existence of a pulsating periodic flow. The observations for the highest Q_L (~ 600 ml/min) and $Q_G = 1340$ ml/min showed that although the liquid flow is periodic, in this case, it

occupies most of the mesh area. However the period of pulsation varied with gas-liquid flow rates and the open area.

(a) 0.01s   1.55 s   1.74 s   3.01 s   5.01 s   7.94 s

(b) 2.64 s   467 s   883 s   934 s   1401 s   2011 s

(c) 0.01 s   2.35 s   6.93 s   14.6 s   24.12 s
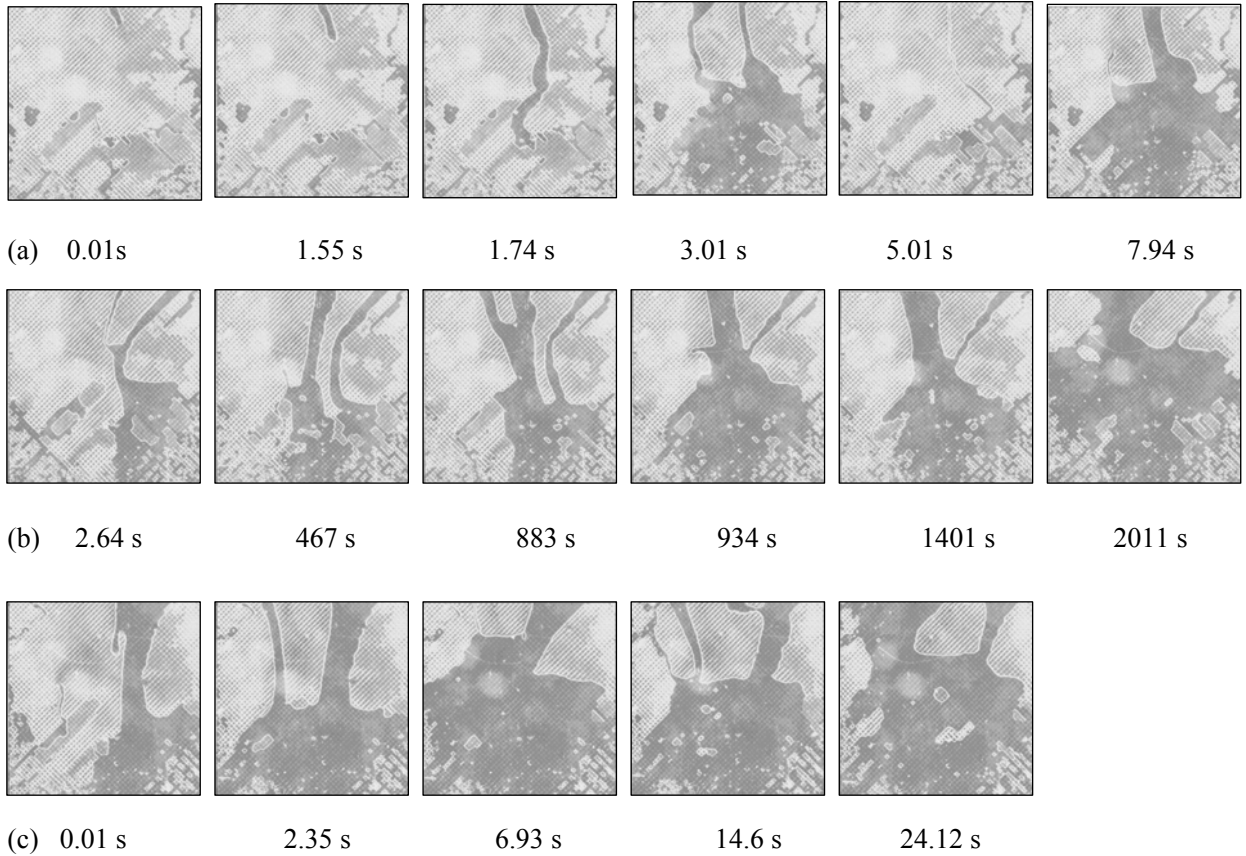
Figure 5.7: Intensity images of the Mesh 3 (M3) for different gas and liquid flow rates. Dark gray color indicates the region occupied by liquid while the relatively lighter shades of gray indicate the region occupied by the gas phase. (a) $Q_L = 150$ $Q_G = 1253$, (b) $QL = 300$ $Q_G = 2486$ (c) $Q_L = 600$ $Q_G = 2486$. Time indicates the time in seconds after a sequence of images was taken.

5.5.2.   Residence time distribution

Typical simulated tracer concentration curves for different liquid flow rates at $Q_G = 2486$ ml/min are shown in Figure 5.8. With the ADEM it was possible to fit the tracer response curves with a tailing end. A set of three parameters, i.e. Pe, number of transfer units N and the dynamic (or static) liquid hold-up that would give the best fit to the experimental tracer concentration curve was obtained for individual data sets. The effect of individual tuning parameters on the predicted concentration history was studied.
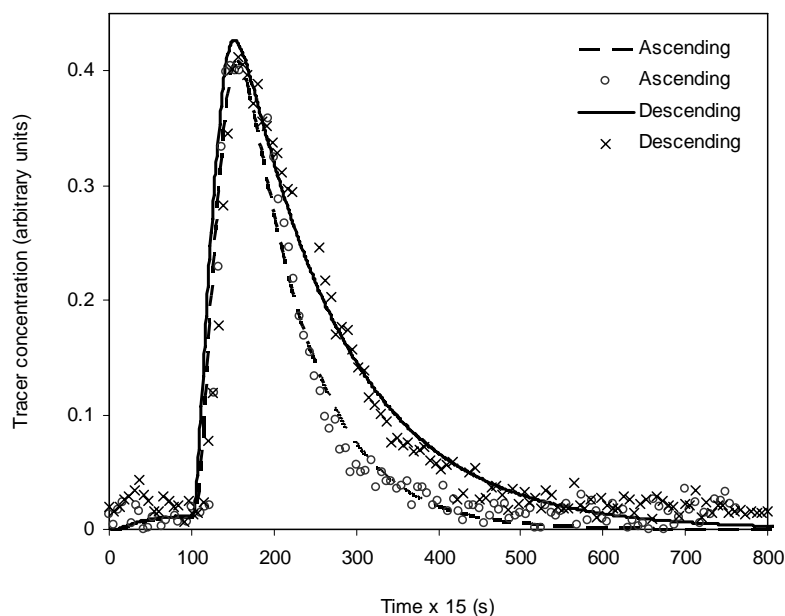
Figure 5.8: Typical experimental and simulated tracer response curves using ADEM

Since the nature of flow in a mesh-microreactor is expected to be analogous to a typical fixed bed reactor, it was also desirable to check the effect of wetting of the mesh on the nature of residence time distribution. Hence, at $Q_G = 2486$ ml/min, the RTD experiments were carried out at different liquid flow rates in increasing order from 50 ml/min to 800 ml/min. Simultaneously the images of the mesh were acquired using high-speed camera. The concentration curves were processed as discussed earlier for both, ascending and descending liquid flow rates. The estimated data were used to obtain the k_L for the exchange of tracer concentration between the static and the dynamic zones and is shown in Figure 5.9 (a) – (b). It was seen that with increasing Q_L, the exchange coefficient increased continuously. However on decreasing Q_L gradually, the variation in the exchange coefficient did not retrace the previous path as for the ascending order of Q_L. This observation was analogous to the typical hysteresis phenomenon observed in the fixed bed reactor. Similar observations were seen for M4. Importantly, although the range of k_L for the two cases was similar, the open area of mesh has an effect on the nature of their variation. The phenomenon of hysteresis was further analyzed using the variation in the Pe for different liquid flow rates in ascending and descending orders. Interestingly, the values of Pe were lower for the experiments involving descending order of Q_L (Figure 5.10). Thus, at $Q_L = 50$ ml/min, Pe is low due to channeling

and it increases with the liquid flow rate making it more a plug flow with larger wetted region of the mesh. At the relatively higher Q_L, the dispersion (mixing) takes over the plug flow nature and the *Pe* is seen to decrease. With a completely wet mesh, even at lower Q_L the dispersion was dominant and the *Pe* was always lower then the corresponding Q_L in the experiments with increasing order of liquid flow rates. On analyzing the images of the mesh at corresponding liquid flow rates, it was seen that the status of wetting of the mesh has a significant influence on enhancing the dispersion. This enhanced dispersion makes the liquid to have less plug flow characteristics than the corresponding situation with less wetted area of the mesh for the case of experiments involving ascending order of liquid flow rates. The same observation prevails for other mesh types.

The estimated static and dynamic hold-up values were confirmed by comparing them against the total liquid hold-up obtained form image analysis. The deviation in the total liquid hold-up was in the range of ±5.6%. The static liquid hold-up was also verified by carrying out the gravimetric analysis at zero liquid velocity and the deviation in the values was in the range of ±8%. These deviations are in the acceptable range and thus confirm the hold-up estimations from the images.
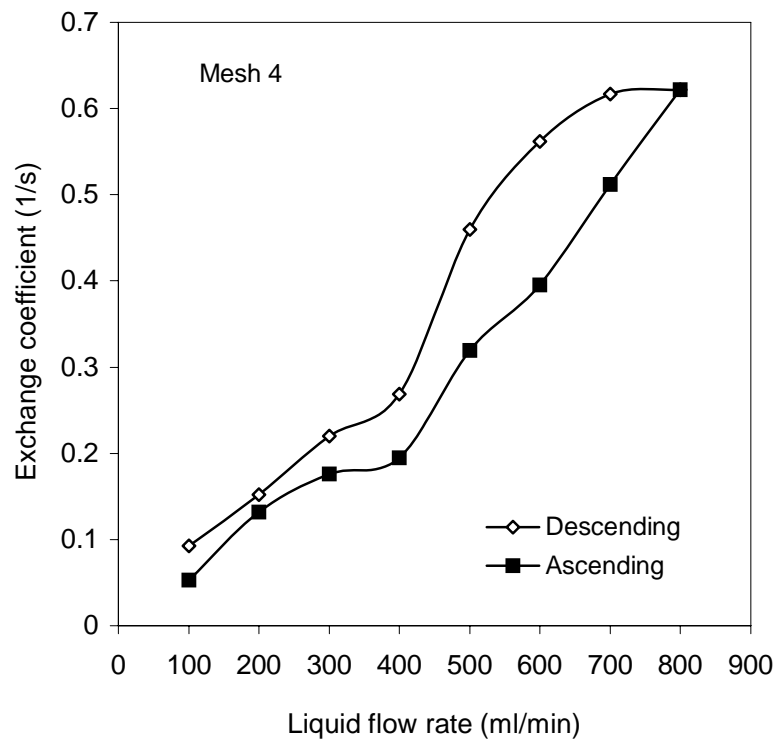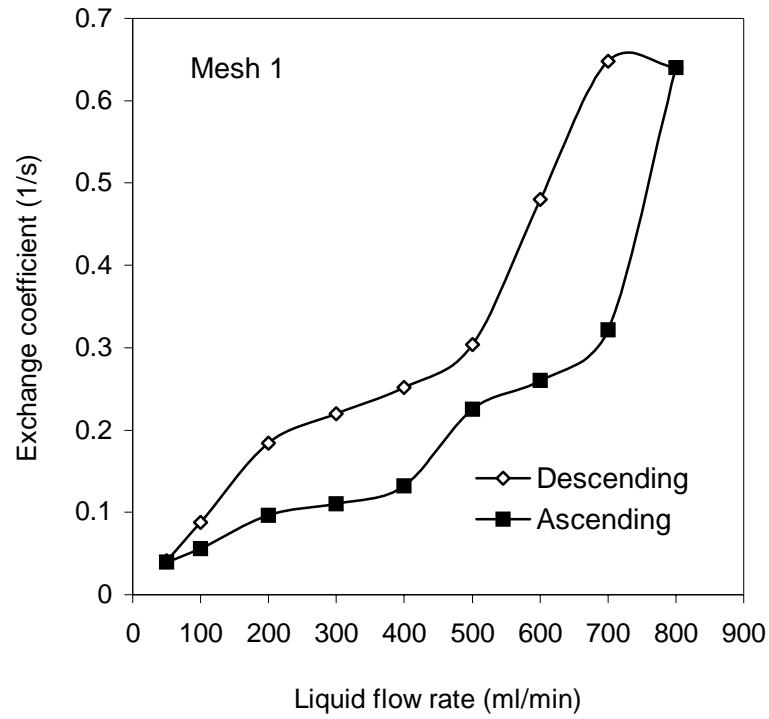
Figure 5.9: Experimental observation of the hysteresis in the exchange coefficient estimated from the concentration curves for mesh-microreactors with Mesh 1 and Mesh 4.
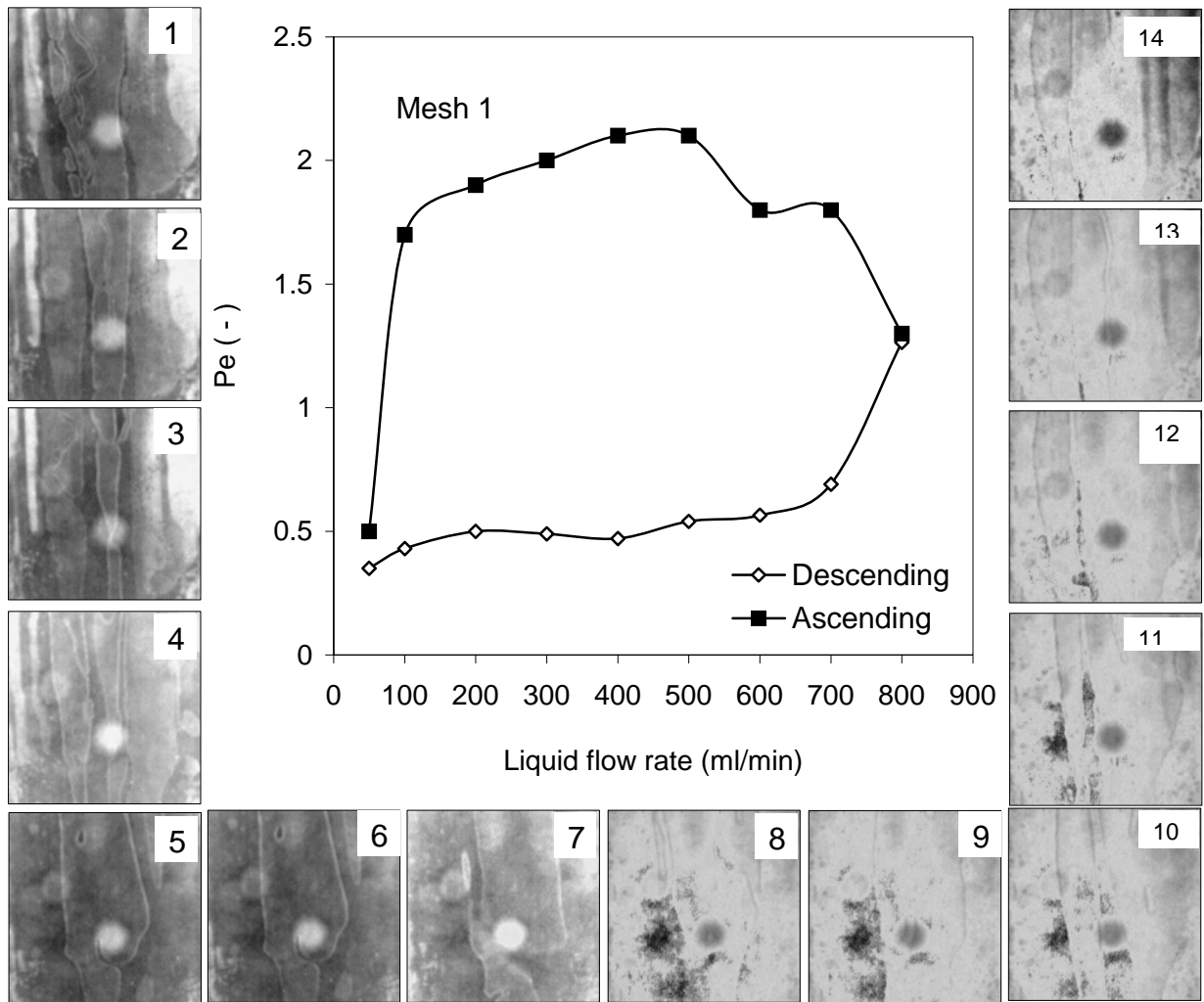
Figure 5.10: Variation in the Peclet number (*Pe*) for different liquid flow rates at Q_G = 2486 ml/min for the case of ascending and descending nature of varying liquid flow rates for Mesh 1. Numbers 1 – 14 indicate the image numbers corresponding to specific liquid flow rates. The bright/dark spot in the lower half of the images is due to the internal reflection of the background illumination.

5.6. Conclusions

Following conclusions are drawn from the above study

- Mesh microreactor is a simple and easy to build kind of a micro-device for gas-liquid and gas-liquid-solid catalytic reactions. No high end micromachining is required. The analysis of the flow in the mesh microreactor with different mesh types shows that the mesh design and open area have a significant effect on the hydrodynamics of the mesh microreactor. The phase hold-up data shows different trends for each mesh and hence it is necessary to choose the right mesh for specific application.

- At high Q_G, the fractional gas hold-up was found to be independent of Q_L and was only a function of the Q_G and the mesh type. The operating range for the liquid is limited by the flow area available for individual mesh types.

- Liquid phase RTD was studied by tracer pulse experiments and the conductivity of the liquid at the outlet of reactor was monitored. ADEM was used to simulate the RTD response curve by assuming non-porous mesh threads and no intra-mesh element mass transfer. The estimated Pe, N and dynamic hold-up data were used for the interpretation of RTD studies.

- The image analysis and the RTD studies showed the existence of hysteresis due to wetting characteristic of the mesh.

Chapter 6

'Y' Separator for Liquid-liquid Separations

6.1. Introduction

Extensive efforts are being made to integrate different process operations such as mixing, heating, reaction and separations into a compact micro-reactor configuration which can be optimized as per the requirements of the reactions under consideration. For example, Jensen and co-workers (Kralj et al. 2007) have integrated mixer, contactor and separator in a single device for conducting liquid-liquid reactions in a capillary microreactor. The separator unit described in this work is based on use of a membrane for separation. Instead of using membranes, Agar and coworkers (Kashid, 2007 and Kashid et al. 2007) have developed a contact angle mediated device for separation of immiscible phases used for liquid-liquid reactions in micro-reactor operated in a slug flow regime. In this case, a 'Y' type separator device is coupled to a capillary micro-reactor and separation of two phases is achieved using a preferential wettability of the phases to the channel surfaces of the 'Y' separator. Preliminary experiments showed reasonable separation effectiveness. 'Y' separators therefore open up new way of manipulating and optimizing separation of liquid-liquid systems. In this work, a systematic investigation fluid dynamics and separation effectiveness of 'Y' separators is carried out. The presented approach and experimental as well as computational results will be useful for further development of such contact angle and geometry mediated compact phase separators.

Effectiveness of separations depends on variety of factors such as geometrical configuration of 'Y' separator, contact angles and flow rates of liquids etc. Balance of inertia and surface forces and their interaction with geometric configuration will ultimately determine the separation efficiency. Considering the large number of parameter space controlling the effectiveness of 'Y' separators, it is essential to develop adequate computational model to interpret and complement experimental results. Such an attempt is made here

6.2. CFD model

Volume of the fluid (VOF) based CFD model was developed for studying flow of two immiscible fluids through 'Y' splitter/separator. VOF method as described by Hirt and Nichols (1981) is one of the most widely used methods in modeling of free surfaces. This is a

fixed mesh method, in which, the interface between immiscible fluids is modeled as a discontinuity in characteristic function (such as volume fraction). Several methods are available for interface reconstruction such as SLIC (simple line interface calculation), PLIC (piece wise linear interface calculations) and Young's PLIC method with varying degree of interface smearing (see, for example, Rider and Kothe, 1995; Rudman, 1997 and Ranade, 2002 for more details). In the present work, VOF method [with PLIC] was used. Both liquid phases were modeled as incompressible, Newtonian fluids with constant value of viscosity and surface tension. Flow was assumed to be laminar. It is important to model surface forces and surface adhesion correctly. Continuum Surface Force (CSF) model developed by Brackbill et al. (1992) was used in this work. Details of model equations are discussed below.

6.2.1. Model equations

The mass and momentum conservation equations for each phase is given by

$$\nabla.u = 0 \qquad\qquad \textbf{6.1}$$

$$\frac{\partial v}{\partial t} + \nabla.(u\,u) = -\frac{1}{\rho}\left[\nabla P + \mu\nabla^2 u\right] + g + \frac{1}{\rho}F_{SF}\,\mathrm{n} \qquad\qquad \textbf{6.2}$$

Where, v is the velocity vector and P is the pressure. $\mathbf{F}_{SF}$ is the continuum surface force vector This single set of flow equations were used throughout the domain and mixture properties as defined below were used. The density of the mixture was calculated as:

$$\rho = \sum \alpha_i \rho_i \qquad\qquad \textbf{6.3}$$

Where, α_i is the volume fraction of the ith fluid. Any other mixture property, Φ, was calculated as:

$$\Phi = \frac{\sum \alpha_i \rho_i \Phi_i}{\sum \alpha_i \rho_i} \qquad\qquad \textbf{6.4}$$

When in a particular computational cell,

$\alpha_i = 0$: the cell is empty (of the ith fluid).

$\alpha_i = 1$: the cell is full (of the ith fluid)

$0 < \alpha_i < 1$: the cell contains the interface between the ith fluid and one or more other fluids.

The interface between the two phases was tracked by solution of a continuity equation for volume fraction function as:

$$\frac{\partial \alpha_i}{\partial t} + (u_i . \nabla) \alpha_i = 0 \qquad\qquad 6.5$$

Volume fraction for the primary phase (gas) was not solved and was obtained from the following equation:

$$\sum \alpha_i = 1 \qquad\qquad 6.6$$

In addition to the mass and momentum balance equations, surface tension and wall adhesion was accounted for. Surface tension was modeled as smooth variation of capillary pressure across the interface. While representing the surface force in the form of volumetric source terms, stresses arriving due to gradient in the surface tension were neglected. Following Brackbill et al. (1992), it was represented as a continuum surface force (F_{SF}) and was specified as a source term in the momentum equation as:

$$F_{SF} = \sigma k n \left(\frac{\alpha_1 \rho_1 + \alpha_2 \rho_2}{\frac{1}{2}(\rho_1 + \rho_2)} \right) \qquad\qquad 6.7$$

$$n = \nabla \alpha_2 \qquad\qquad 6.8$$

$$k = -(\nabla . \hat{n}) = \frac{1}{|n|} \left[\left(\frac{n}{|n|} . \nabla \right) |n| - (\nabla . n) \right] \qquad\qquad 6.9$$

where, n is the surface normal, $\hat{n}$ is the unit normal and κ is curvature. Surface normal n was evaluated in the cells containing interface and requires knowledge of amount of volume of

fluid present in the cell. Geometric reconstruction scheme (based on piece wise linear interface calculation, PLIC) was used to calculate the interface position in the cell. Adhesion to the wall influences the calculation of surface normal.

6.2.2. Computational domain

A typical geometry for the simulation is as shown in Figure 6.1. It consists of a 'Y' shape element at the inlet and exit connected to each other with a capillary tube. The dimensions of all the capillaries are kept constant (0.75mm) except at the exit which was kept to be 0.5mm. This was done to keep in consistent with the experimental design. The length of the capillary was taken as 15mm (the basis for this was that the length of the capillary should be greater then at-least two times the expected slug length). A commercial grid-generation tool, GAMBIT 2.3 (of Fluent Inc., USA) was used to model the geometry and to generate the computational grids.

For VOF simulations there is always a catch between the accuracy of the simulation and the physical time required for the simulation using available resources. The time step and grid size are always maintained such that the Courant number (which compares the time step in a calculation to the characteristic time of transit of a fluid element across a control volume) is always maintained below 0.25 so that the minimum transit time for any cell near the interface is at-most one-fourth of the time step.

$$Courant\ number\ =\ \frac{\Delta t}{\Delta x_{cell} \big/ u_{fluid}} \qquad\qquad \textbf{6.10}$$

Since the objective of the present study was to see if VOF simulations are capable of capturing the separation phenomenon occurring at the junction of 'Y' separator a grid size not less then 50μm was used in the simulations. For applications which intend to capture liquid film region between the liquid slug and the capillary wall which is of the order of 50-100 micron size the grid must be resolved to the extent of 5-10 micron size. The number of cell count within the domain was also kept below 25000 cells. This was done so that the

simulations could be run for a longer time of at-least 2-3s to get a better time averaged values.

The option of considering a 2d geometry instead of 3d geometry was also considered to reduce the grid count. However considering a 2d geometry will have two effects on the simulated results. First is the surface tension force acting per surface area will be less in a 2d as compared to a 3d geometry thereby leading to less effective separation. It will also effect the slug formation at the 'Y' mixer. Secondly some of the geometric constraints such as the junction of 0.5mm capillary with a 0.75mm capillary (Figure 6.1) would not had been captured. Hence, instead of a 2d geometry, a 3d geometry with 180° domain was considered for the simulation.
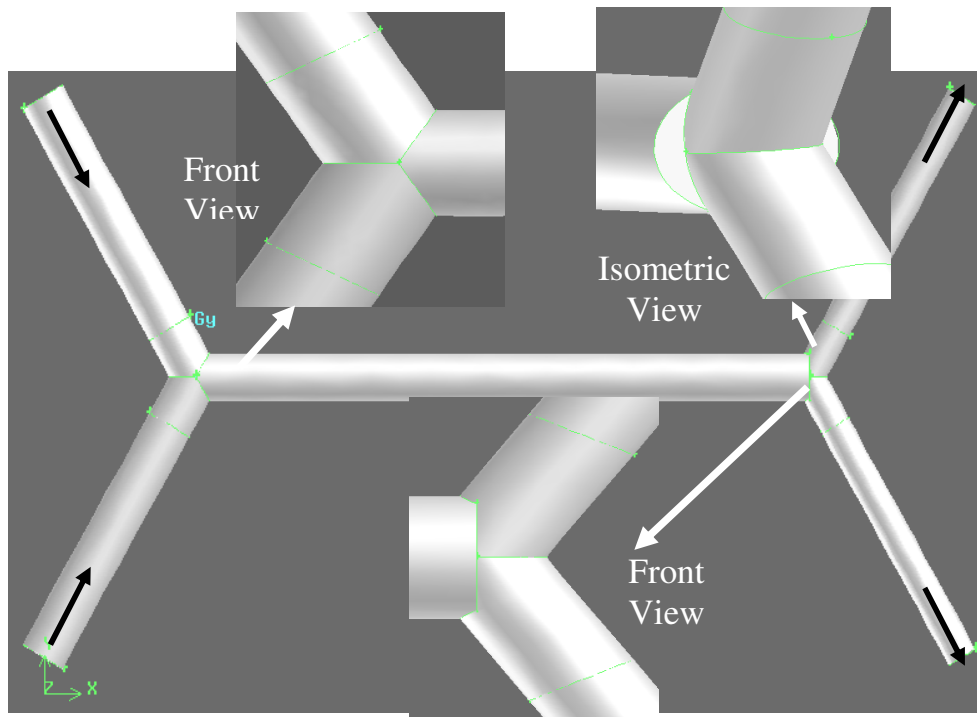
Figure 6.1: Computational Domain

6.2.3. Boundary conditions

Simulations were performed for Kerosene-water system. The capillary MOC was considered as Teflon, same as used in the experiments of Kashid (2007). Kerosene being the wetting liquid was considered as continuous/ primary phase and water being non-wetting was considered as dispersed/ secondary phase. The physical properties of the above mentioned fluids are as given in Table 6.1. The interfacial tension between kerosene and water was taken as 50 dynes/cm

Table 6.1: Characteristics of liquids used in simulations

Liquid	Density(Kg/m^3)	Viscosity(10^{-3} Pas)
Kerosene	780	2.1
Water	1000	1

For all the simulations fully developed velocity profiles were specified for both the liquid inlets. At the exit pressure outlet boundary conditions were used and the pressure at the exit was equal to the atmospheric pressure ($p_{outlet} = p_{atm}$). All the walls were specified as hydrophobic (Teflon, $\theta_W = 30°$) except one arm of the 'Y' splitter at the exit, which was specified as hydrophilic (Steel, $\theta_W = 150°$). No slip boundary conditions also prevailed at all walls. Figure 6.2 shows the schematic of the boundary conditions used.

Figure 6.2: Boundary conditions for the flow

113

6.2.4. Numerical solution

The set of model equations was solved with boundary conditions discussed above using the commercial flow solver Fluent 6.3.26 (of Fluent Inc., USA). Mass and momentum equations were solved using second order implicit 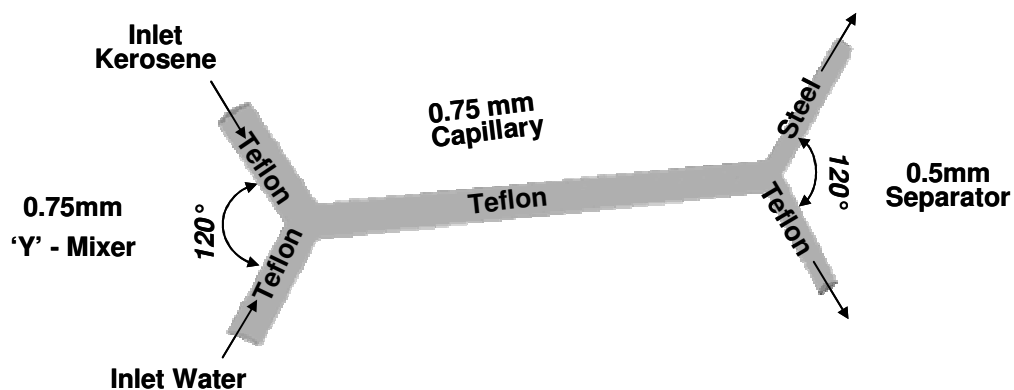method for space and first order implicit method was used for time discretization. Pressure interpolation was performed using body force weighted scheme. This scheme is useful when gravitational force is comparable with pressure force. Pressure implicit with splitting of operator (PISO) was used for pressure velocity coupling in momentum equation. This scheme was used to reduce the internal iteration per time step and (relatively) larger under relaxation parameters can be used. Solution was initialized by zero velocity in all the cells and phase fraction of the primary phase (kerosene) = 1. Time step between one to five microseconds (1-5 μs) was found to capture key features of dynamics of slug flow adequately (simulations using $2 * 10^{-6}$ and $4 * 10^{-6}$ showed no significant difference in the predicted results). Twenty to thirty internal iterations per time step were performed, which were found to be adequate for bringing down the normalized residuals below $1 * 10^{-5}$. With further increase in time step ($5 * 10^{-6}$), required number of internal iterations was found to be increasing. Mass flow rate of individual phase from each outlet is monitored after every one 1ms interval.

6.3. Results and discussion

Simulations were first performed for different flow rate of water keeping flow rate of kerosene constant. Typical contours of volume fraction at the central plane for the case of Q_k =10ml/hr and Q_w = 20ml/hr are shown in Figure 6.3. As observed in each phase uniform sizes of the slugs are formed. The capillary wall being hydrophobic the water slugs form the closed curvatures where as kerosene slugs have open curvatures. Also as discussed in the previous section, since the grid resolution wasn't fine, there was no kerosene film observed around the water slug near the wall. Figure 6.4 shows the axial velocity profiles predicted at the centre of the slugs in both the phases. The velocity profiles are parabolic in shape with maximum velocity at the centre of the channel. This was compared with fully developed flow profile for single phase having an average velocity equal to two phase velocity U_{TP} given by

$$U_{TP} = \frac{Q_k + Q_w}{A}$$
<div align="right">**6.11**</div>

The velocity profiles are normalized with maximum velocity of fully developed flow profile ($2*U_{TP}$). It is observed that with increasing volumetric flow rate of water the velocity profile of kerosene shifts towards the fully developed flow. However, the velocity profile of water remains same
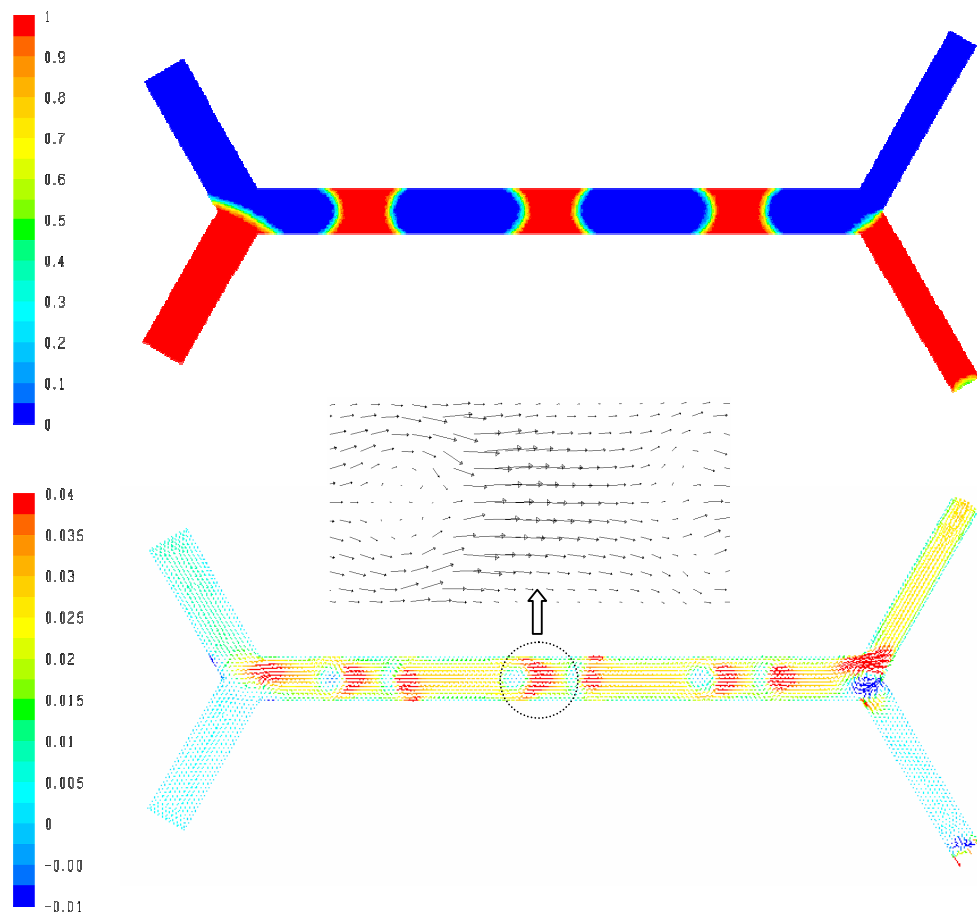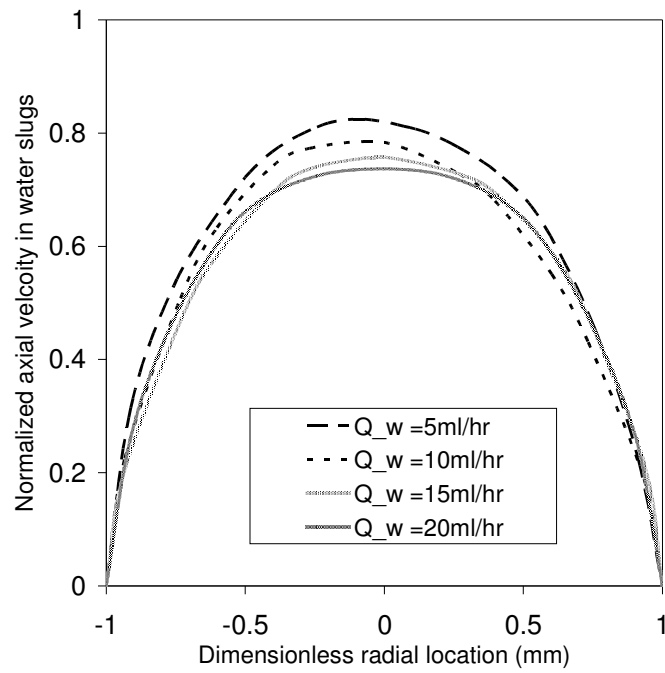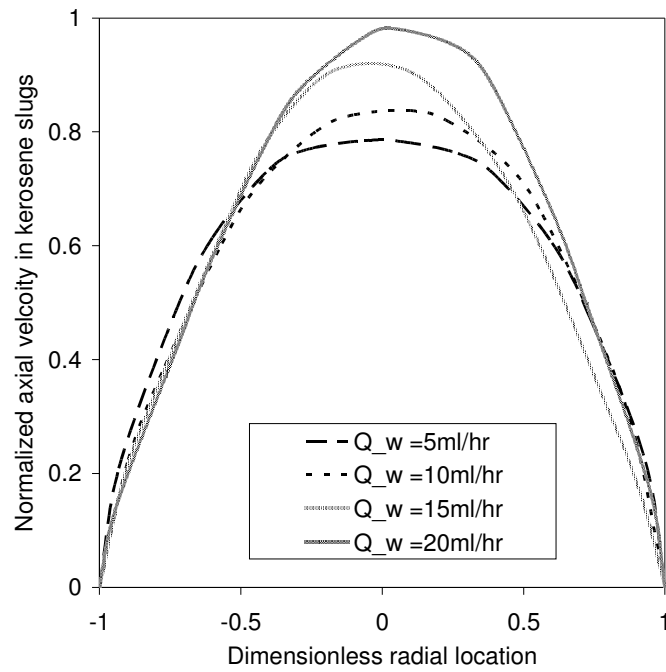

Figure 6-3 : Typical contour plot of volume fraction of water and velocity vector plot of axial velocity ($Q_k = 10$ml/hr and $Q_w =20$ml/hr)

.

(a) : Velocity profiles at the centre of the water slugs

(b) Velocity profiles at the centre of the water slugs

Figure 6.4. Normalized velocity profiles found at the centre of the respective slugs.

Figure 6.5(a) shows the variation of length of slugs with varying flow rate of water keeping the kerosene flow rate constant at 10ml/hr. The length of water slugs increases where as that of kerosene slugs decreases. Figure 6.5(b) shows variation of length of slugs with varying flow rate of kerosene at constant water flow rate. A similar trend is observed. This data is then compared with experimental data of Kashid et al (2007). A relatively good agreement is observed.

Computation of separation efficiency required monitoring the time history of the mass coming out of the capillary from respective outlets. However, it was observed that there is a significant amount of reverse flow back into the domain from both the outlets. Analysis revealed that the reverse flow is because of the negative pressure built at respective outlets caused due to fluctuations occurring at the 'Y' separator during slug separation.

Experimental observations indicate similar behavior during experimental runs. However, in the actual experiments the system was open to atmosphere, and hence the reverse flow was that of air and so the separation was unaffected by the reverse flow. On the other hand, while solving the model equations only two phases (water and kerosene) were considered and because of this the separation efficiency was governed by the backflow volume fraction specified at the outlet. Hence it was required to perform to three phase simulations instead of two phase simulations.

The above work shall however, serve as a useful basis for further efforts to quantify separation efficiency.
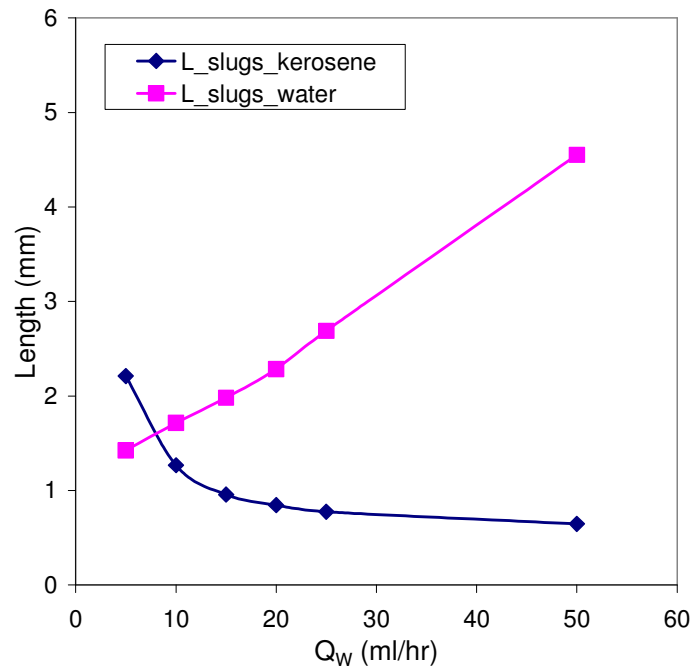
(a) keeping flow rate of organic phase constant = 10ml/hr
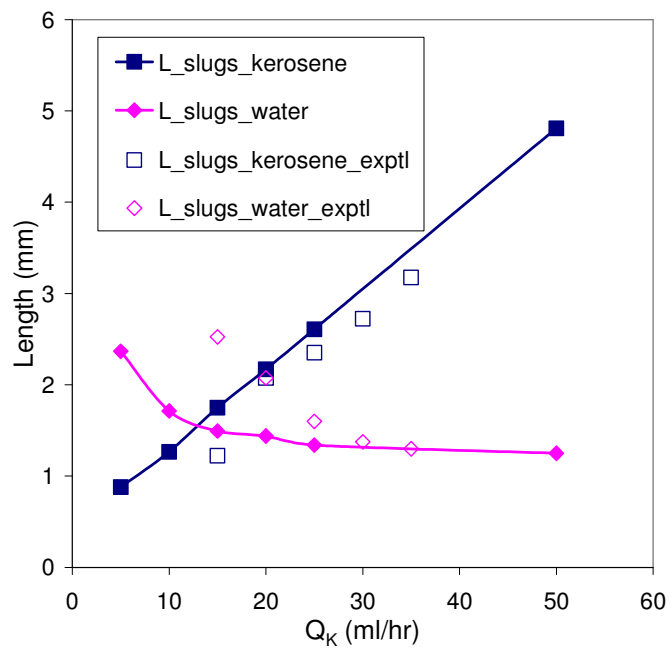
(b) keeping flow rate of aqueous phase constant = 10ml/hr

Figure 6.5: Effect of volumetric flow rate on lengths of slugs

6.4. Conclusions

Following conclusions are drawn from the above study

- The concept of 'Y' separator as proposed by Agar and coworkers for liquid-liquid separation in a slug flow capillary microreactor was studied using multiphase CFD simulations.
- The model was qualitatively able to capture the phenomenon of separation occurring due to preferential wettability of the phases to the channel surfaces.
- The simulated results for the observed slugs lengths of respective phases at various flow rates were compared with experimental data and a reasonably good agreement was observed

Chapter 7

Summary and Conclusions

The first part of this thesis focuses on gas-liquid flow in a single capillary channel. Parameters such as flow patterns, holdup, bubble/ slug lengths/ velocities were determined experimentally. Models to quantify liquid velocity profiles and volumetric mass transfer coefficient were developed. Furthermore a reactor model to predict performance of microreactors was developed and evaluated. The second part of this thesis explores new designs of microreactors such as 'mesh-microreactor' and 'Y' separator.

Experiments were conducted in a 0.84mm capillary for co-current downflow of gas and liquid using a 'T' type mixer. Flow visualization technique was used to identify sub flow patterns of slug flow. Using image analysis, key hydrodynamic parameters such as bubble shape, velocity and lengths were determined. Parameters such as gas holdup and film thickness were estimated from the measured parameters. Measured parameters were compared with the published correlations. Also a correlation for predicting bubble and slug lengths in sub flow pattern P1 was proposed and verified with the other data available in the literature

A CFD model based on a unit cell approach was developed to simulate co-current downward gas-liquid slug flow in a square capillary. The Taylor bubble was considered as a "void", acting as a free surface with the surrounding liquid phase. CFD simulations were performed to determine liquid velocity profiles and volumetric mass transfer coefficients in slug flows. The model predictions were compared with the experimental PIV data from Birmingham University. A consistent error between the numerical analysis and experiment work was realized. Further work is needed to resolve these differences. Despite the differences, normalized (with maximum velocity) predicted results showed good agreement with normalized experimental data of Tsoligkas et al. (2007).

A general purpose reaction engineering model based on mass and energy balances was developed to simulate multiphase reactions occurring in micro-channel reactors. Appropriate correlations for different hydrodynamic parameters such as film thickness, holdup, bubble and slug length, mass transfer and dispersion coefficients were used from the literature and prior conducted studies. A case-study of 2,4,DNT was used to demonstrate the application of the developed model. Parametric sensitivity studies were conducted to study the effect of various operating parameters on conversion and selectivity of 4A2NT

A relatively new type of micro-reactor namely 'mesh-microreactor' was studied in this work. The focus was on hydrodynamics and mixing. Experiments were conducted to determine different hydrodynamic parameters such as flow patterns, holdup and mixing in mesh-microreactor. An ADEM model to characterize mixing was developed and model predictions were compared with the experimental results. An observed hysteresis in the flow was verified using the RTD and image analysis results.

A 'Y' separator as reported by Agar and co-workers (Kashid, 2007) for separating liquids based on preferential wettability of liquid to the solid material was also explored using CFD models. A VOF model was developed to simulate liquid-liquid flows in capillaries. Separation of liquid slugs at the 'Y' junction based on contact angle was studied for different flow rates. Although the separation phenomenon is captured by the model, separation efficiency couldn't be quantified due to limitations in the developed model. However, the model will form a useful basis for further efforts to quantify separation efficiency.

References

Abdallah, R., Meille, V., Shaw, J., Wenn, D, de Bellefon, C., (2004). Gas–liquid and gas–liquid–solid catalysis in a mesh microreactor, Chemical Communications, 372–373

Abdallah, R., Magnico, P., Fumey, B., de Bellefon, C. (2006). CFD and kinetic methods for mass transfer determination in a mesh microreactor, AIChE Journal, **52**(6), 2230

Akbar, M.K., Plummer, D.A. and Ghiaasiaan, S.M. (2003). On gas–liquid two phase flow regimes in microchannels. International Journal of Multiphase Flow, **29**, 855–865.

Akbar, M. K., and Ghiaasiaan, S. M., (2006) Simulation of Taylor Flow in Capillaries Based on the Volume-of-Fluid Technique, Ind. Eng. Chem. Res. **45**, 5396-5403

Armand, A. A., (1946) The resistance during the movement of a two-phase system in horizontal pipes, Izv. Vses. Teplotekh. Inst. **1,** 16–23.

Aussilous, P., and Quere. D., (2000) Quick deposition of a fluid on the wall of a tube. Physics of Fluids **12**, 2367–2371.

Bercic, G., and Pintar, A., (2003) The role of gas bubbles and liquid slug lengths on mass transport in the Taylor flow through capillaries. Chemical Engineering Science **52**, 3709–3719.

Brackbill, J. U., Kothe, D. B. and Zemach, C., (1992).A continuum method for modelling surface tension. Journal of Computational Physics, **100**(2): 335

Bretherton, F. P., (1961) The motion of long bubbles in tubes. Journal of Fluid Mechanics **10**, 166–188.

Chen, W. L., Twu, M. C., and Pan, C., (2002) Gas–liquid two-phase flow in microchannels, Int. J. Multiphase Flow **28**, 1235–1247.

Chung, P. M. Y., and Kawaji, M., (2004) The effect of channel diameter on adiabatic two-phase flow characteristics in microchannels, Int. J. Multiphase Flow **30**, 735–761.

Devasenthipathy, S., Santiago, J. G., Wereley, S. T., Meinhart, C. D., and K. Takehara. (2003) Particle imaging techniques for microfabricated fluidic systems.Experiments in Fluids, **34**:504–514,.

Edvinsson, R. K., and Irandoust, S., (1996) Finite-element analysis of Taylor flow. A.I.Ch.E. Journal **42**, 1815–1823.

Ehrfeld, W., Hessel, V., Löwe, H., (2000). Microreactors. Wiley-VCH, Weinheim.

Elperin, T., and Fominykh, A., (1998) Mass transfer during gas absorption in a vertical gas liquid slug flow with small bubbles in liquid plugs. International Communications in Heat and Mass Transfer, **33**:489–494

Fairbrother, F., and Stubbs, A. E., (1935) Studies in electroendosmosis-VI. The bubble tube method of measurement. Journal of Chemical Society **1**, 527- 529.

Fukano, T., and Kariyasaki, A., (1993) Characteristics of gas–liquid two-phase flow in a capillary tube. Nuclear Engineering and Design **141**, 59–68.

Garstecki P., Fuerstman M.J., Stone H.A. and Whitesides G.M. (2006). Formation of droplets and bubbles in a microfluidic T-junction—scaling and mechanism of break-up. Lab on a Chip **6**, 437–446.

Gregory, G., and Scott, A., (1969) Correlation of liquid slug velocity and frequency in horizontal co-current gas–liquid slug flow, AIChE J. **15**, 933–935.

Hasebe, S., (2004). Design and operation of micro-chemical plants—bridging the gap between nano, micro and macro technologies, Computers and Chemical Engineering 29, 57–64

Heibel, A. K., Heiszwolf, J.J., Kapteijn, F., Moulijn, J. A.(2001). Influence of channel geometry on hydrodynamics and mass transfer in the monolith film flow reactor, Catalysis Today 69,153-163

Heiszwolf, J. J., Kreutzer, M. T., van den Eijnden, M. G., Kapteijn, F., and Moulijn, J. A., (2001) Gas–liquid mass transfer of aqueous Taylor flow in monoliths. Catalysis Today **69**, 51–55.

Hessel, V, Löwe, H., (2003) Micro chemical engineering: components-plant concepts-user acceptance. Chemical Engineering and Technology **26**(1), 13.

Hirt, C. W. and Nichols, B. D. (1981) Volume of fluid (VOF) method for the dynamics of free boundaries. Journal of Computational Physics, 39:201–225

Ide, H., Kariyasaki , A., and Fukano, T., (2007) Fundamental data on the gas–liquid two-phase flow in minichannels, International Journal of Thermal Sciences **46**, 519–530

Irandoust, S., and Andersson, B., (1989) Liquid film in Taylor flow through a capillary. Industrial and Engineering Chemistry Research **28**, 1684–1688.

Jayawardena, S. S., Balakotaiah, V., and Witte, L., (1997) Flow Pattern Transition Maps for Microgravity Two-Phase Flows. AIChE Journal **43** (6), 1637-1640

Kariyasaki, A., Fukano, T., Ousaka, A., and Kagawa, M., (1991) Characteristics of time-varying void fraction in isothermal air–water co-current flow in horizontal capillary tube, Trans. JSME **57** (544), 4036–4043.

Kashid M. N, PhD Dessertation, Dortmund University, Germany (2007)

Kashid, M. N., Gerlach, I., Goetz, S. Franzke, J., Acker, J. F., Platte, F., Agar, D. W., and Turek, S., (2005), Internal Circulation within the Liquid Slugs of a Liquid-Liquid Slug-Flow Capillary Microreactor, Ind. Eng. Chem. Res. 44, 5003-5010

Kashid, M. N., Harshe, Y. M. and Agar, D. W., (2007) Liquid-liquid slug flow in a capillary: an alternative to suspended drop of film contactor, Industrial and Engineering Chemistry Research, 46 (25), 8420 -8430,

Kawahara, A., Chung, P. M. Y., and Kawaji, M., (2002) Investigation of two phase flow pattern, void fraction and pressure drop in a microchannel, Int. J. Multiphase Flow **28,** 1411–1435.

Kiwi-Minsker, L., Joannet, E., Renken, A., (2004). Loop reactor staged with structured fibrous catalytic layers for liquid-phase hydrogenations, Chemical Engineering Science, 59, 4919 – 4925

Kralj, J. G., Sahoo, H. R, Jensen, K. F., (2007). Integrated continuous microfluidic liquid–liquid extraction, Lab on Chip, 7, 256–263

Kraus, T., G̈unther A., de Mas, N., Schmidt, M. A., and Jensen, K. F. (2004) An integrated multiphase flow sensor for microchannels, Experiments in Fluids, **36**,819–832

Kreutzer, M. T., (2003) Hydrodynamics of Taylor flow in capillaries and monoliths channels. Doctoral dissertation. Delft University of Technology, Delft, The Netherlands

Kreutzer, M. T., van der Eijnden, M. G., Kapteijn, F., Moulijn, J. A., and Heiszwolf. J. J., (2005) The pressure drop experiment to determine slug lengths in monoliths. Catalysis Today **105**, 667–672.

Laborie, S., Cabassud, C., Durand- Bourlier, L., Lainé, J. M. (1999). Characterisation of gas-liquid two-phase flow inside capillaries, Chemical Engineering Science 54, 5723-5735

Levenspiel, O. (1999). Chemical Reaction Engineering, Wiley Eastern Univ. Edition, NY

Liu, H. Vandu, C. O. and Krishna, R. (2005) Hydrodynamics of Taylor Flow in Vertical Capillaries: Flow Regimes, Bubble Rise Velocity, Liquid Slug Length, and Pressure Drop, Ind. Eng. Chem. Res., **44**, 4884-4897

Liu, D., and Wang, S., (2008), Hydrodynamics of Taylor flow in noncircular capillaries, Chemical Engineering and Processing : Process Intensification, 47, 2098-2106

Losey, M. W., Schmidt M. A, Jensen, K. F., (2001). Microfabricated multiphase packed-bed reactors: mass transfer and reactions, Industrial & Engineering Chemistry Research, **40**, 2555

Malyala, R. V., Chaudhari, R.V., (1999) Hydrogenation of 2,4-dinitrotoluene using a supported Ni catalyst, Ind. Engg. Chem. Res., **38**, 906-915.

Mamayev, V. A., Odisharia, G. E, Klapchuk O. V, Tochigin A. A., and Semyonov N. I (1978) Motion of Gas-Liquid Mixtures in Pipes, Nedra, Moscow.

Mishima, K., and Hibiki, T., (1996) Some characteristics of air-water two-phase flow in small diameter vertical tubes. Int. J. Multiphase Flow **22**, 703-712.

Paglianti, A., Giona, M., and Soldati, A., (1996) Characterization of subregimes in two-phase slug flow. International Journal of Multiphase Flow, **22**(4), 783–796,

Pennemann, H., Watts, P., Haswell, S. P., Hessel, V., and Lowe, H., (2004) Benchmarking of Microreactor Applications Organic Process Research & Development **8**, 422-439

Pfund, D., Rector, D., Shekarriz, A., Popescu, A., Welty, J., (2000). Pressure drop measurements in a microchannel, **46**(8), AIChE Journal, 1496

Qian, D., and Lawal , A., (2006) Numerical study on gas and liquid slugs for Taylor flow in a T-junction microchannel, Chemical Engineering Science **61**, 7609 – 7625

Ranade V. V. 2002, Computational flow modeling for chemical reactor engineering, Academic Press, London.

Rider W. J. and Kothey, D. B., (1998). Reconstructing Volume Tracking, Journal of Computational Physics, 141**,** 112–152,

Roy, S., A. K. Heibel, W. Liu, and T. Boger, (2002) Design of Monolithic Catalysts for Multiphase Reactions," Oral Presentation, 17th ISCRE.

Rudman, M., (1997). Volume tracking methods for interfacial flow calculations, International Journal for Numerical Methods in Fluids, 24, 671

Serizawa, A., Feng, Z., and Kawara, Z., (2002) Two-phase flow in micro-channels, Exp. Therm. Fluid Sci. **26**, 703–714.

Simmons, M.. J., Wong, D. C. Y., Travers, P. J., and Rothwell, J. S., (2003) Bubble behaviour in three phase capillary microreactors. International Journal of Chemical Reactor Engineering, 1, **A30**.

Taha, T., and Cui, Z. F. (2004) Hydrodynamics of slug flow inside capillaries, Chemical Engineering Science **59**, 1181 – 1190

Taha, T., and Cui, Z.F., (2006) CFD modeling of slug flow inside square capillaries.Chemical Engineering Science **61**, 665–675.

Thulasidas, T. C., Abraham, M. A., and Cerro. R. L., (1995) Bubble-train flow in capillaries of circular and square cross section. Chemical Engineering Science **50**, 183–199.

Thulasidas, T.C., Abraham, M.A., Cerro, R. L. (1997). Flow patterns in liquid slugs during bubble-train flow inside capillaries, Chemical Engineering Science **52**, 2947-2962

Trachsel, F., Günther, A., Khan, S., Jensen, K. F., 2005. Measurement of residence time distribution in microfluidic systems, Chemical Engineering Science 60, 5729.

Triplett, K. A., Ghiaasiaan, S. M., Abdel-Khalik, S. I., and Sadowski, D. L., (1999) Gas–liquid two-phase flow in microchannels Part I: two-phase flow patterns, Int. J. Multiphase Flow **25**, 377–394.

Tsoligkas, A.N., Simmons, M.J.H., and Wood, J., (2007) Influence of orientation upon the hydrodynamics of gas–liquid flow for square channels in monolith supports. Chemical Engineering Science **62**, 4365-4378

Van Baten, J. M., and Krishna, R., (2004) CFD simulations of mass transfer from Taylor bubble rising in circular capillaries, Chemical Engineering Science **59**, 2535-2545

Van Swaaij, W. P. M., Charpentier, J. C., & Villermaux, J. 1969. Residence time distribution in the liquid phase of trickle flow in packed columns. Chemical Engineering Science, **24**, 1083

Villermaux, J., Van Swaaij, W. P. M. 1969. Modèle représentatif de la distribution des temps de s'jour dans un réacteur semi infini a dispersion axiale avec zones stagnantes, Chemical Engineering Science, **24**, 1097

Wallis, G. B., (1969) One-Dimensional Two-Phase Flow. McGraw-Hill, New York..

Warnier, M. J. F., Rebrov, E. V., de Croon, M. H. J. M., Hessel, V., and Schouten, J. C., (2008) Gas hold-up and liquid film thickness in Taylor flow in rectangular microchannels. Chemical Engineering Journal **135S**, S153–S158

Wenn, D. A., Shaw, J. E. A, Mackenzie, B., 2003. A mesh microcontactor for 2-phase reactions, Lab on Chip, **3**, 180–186

Wren, E., Baker, G., Azzopardi, B. J., and Jones, R., (2005) Slug flow in small diameter pipes and T-junctions, Experimental Thermal and Fluid Science **29**, 893–899

Yeong, K. K., Gavriilidis, A., Zapf, R., Hessel, V. 2004. Experimental studies of nitrobenzene hydrogenation in a microstructured falling film reactor, Chemical Engineering Science, 59, 3491

Yu, Z., Hemminger, O. and Fan, L.S. (2007). Experiment and lattice Boltzmann simulation of two-phase gas–liquid flows in microchannels, Chemical Engineering Science, **62**, 7172-7183

Zhao, L., and Rezkallah, K. S., (1993) Gas–liquid flow patterns at micro-gravity conditions, Int. J. Multiphase Flow **19**, 71–763.

Zuber, N., and Findlay, J., (1969) Average Volumetric Concentration in Two-Phase Systems," Trans ASME Jul Ht Transfer **87**, p 453

List of Publications/Conference Presentations

Gorasia, A. K., Ezhilan, B., Mahajani, S. M., and Ranade V.V. Characterization of Gas-Liquid Slug Flow in Circular Micro-Channels. (to be submitted to I&ECR)

Kulkarni, A. A., Gorasia, A. K. and Ranade, V. V. (2007), "Hydrodynamics and Liquid Phase Residence Time Distribution in Mesh Microreactor", Chemical Engineering Science, 62, 7484-7493

Kashid, M. N., Gorasia, A. K., Ranade, V. V, and Agar, D. W. "Y Separator for Liquid-Liquid Microreactors: Experiments and CFD Simulations", accepted for oral presentation at International Symposium on Chemical Reaction Engineering 'ISCRE-20', Kyoto, Japan

Gorasia A. K., Tsoligkas, A. N., Wood, J., Simmons, M.J. and Ranade V. V. (2006), "Hydrodynamics of Two-Phase Flow in a Capillary: PIV Measurements and CFD Simulations", presented at FLUENT-UGM, 2006, Pune, INDIA

Nanduru, C, Aditya Kumar, Gorasia, A.K. and Ranade, V.V. (2006), "Study of Flow Regimes in Micro-Channels", ORAL presentation at ChemCon, 2006, Ankleshwar

Parvathikar, S., Gorasia, A. K., and Ranade, V.V. (2006), "Gas-Liquid-Solid Reactions in Micro-Channel Reactors: A Case study of Nitro Aromatic Hydrogenation", ORAL presentation at ChemCon, 2006, Ankleshwar

Gorasia, A. K., Khopkar, A. R., and Ranade V. V. (2004), "CFD Simulations of Flow and Mass Transfer in Taylor Flow Through a Narrow Channel", Presented at IIChe-AIChE Joint meeting – ChemCon 2004, Mumbai

Acknowledgements

This thesis is culmination of work done during last few years at the Industrial Flow Modeling Group (iFMg), NCL Pune. Many people in many ways have helped me through this endeavor. Their support has kept me motivated throughout the course of the PhD

First of all, I am greatful to my supervisor Dr. Vivek V. Ranade at National Chemical Laboratory (NCL), Pune. Working with him was one of the most fortunate things that have happened in my life. I could not have imagined having a better advisor and mentor for my PhD, and without his knowledge, perceptiveness and approach to crack problems, I would never have finished my work in time.

I would like to thanks my guide at IITB Prof. Sanjay Mahajani for his useful discussions during the research work. I would also like to thanks to Research Progress Committee members, Professors V. A. Juwekar and Prof. A.K. Suresh for their valuable suggestions and guidelines during the RPC meetings.

I would also like to thank Dr Amol Kulkarni, Saurabh, Aditya, Chanukya and Barath with whom I worked during the course of my PhD work.

I greatly appreciate various kind of support from all my seniors; Buwa, Gunjal, Khopkar, Ranjeet and Kaustubh who helped me in several things other than technical stuff. Special thanks to my colleagues Mohan and Naren for helping me several times during my work. Interacting with them has always helped me in getting my fundamentals more clear. I would also like to thank Madhavi, Dev, Latif, Chaitanya and all past and present members iFMg for making my stay at NCL more enjoyable. I also appreciate the support from workshop and other utility departments

I am grateful to Council of Scientific and Industrial Research (CSIR), India for providing the financial support during my research work and Department of Science and Technology for providing funding required for the project.

Last but not the least I would also like to say thanks to my entire family particularly to my mom and my dad and most importantly to my wife Deepa for standing by me at all times, may be good or bad.

Ajay Gorasia